Generic testing in photonic IC's

Document status and date:
Published: 01/01/2015

Document Version:
Publisher's PDF, also known as Version of Record (includes final page, issue and volume numbers)

Please check the document version of this publication:

• A submitted manuscript is the version of the article upon submission and before peer-review. There can be important differences between the submitted version and the official published version of record. People interested in the research are advised to contact the author for the final version of the publication, or visit the DOI to the publisher's website.
• The final author version and the galley proof are versions of the publication after peer review.
• The final published version features the final layout of the paper including the volume, issue and page numbers.

Link to publication

Download date: 04. Oct. 2023

Generic Testing in Photonic ICs

PROEFSCHRIFT

ter verkrijging van de graad van doctor aan de Technische Universiteit Eindhoven, op gezag van de rector magnificus prof.dr.ir. C.J. van Duijn, voor een commissie aangewezen door het College voor Promoties, in het openbaar te verdedigen op donderdag 23 februari 2015 om 16:00 uur

door

Elton Bitincka

geboren te Korçë, Albanië

Dit proefschrift is goedgekeurd door de promotoren en de samenstelling van de promotiecommissie is als volgt:

voorzitter   prof.dr.ir. A.C.P.M. Backx
1^e promotor: prof.dr.ir. M.K. Smit
2^e promotor: prof.dr. K.A. Williams
copromotor: dr. X.J.M. Leijtens
leden: prof.ir. A.M.J. Koonen
                dr. N. Whitbread (Oclaro Technology Ltd.)
                dr. M. Heck (University of Aarhus)
                dr.-ing. N. Grote (Fraunhofer Heinrich Hertz Institute)

Generic Testing in Photonic ICs, by Elton Bitincka

Typeset using LaTeX

Contents

Contents

Dedicated to my parents

List of Acronyms

ADS   Advanced Design Systems
ASE   Amplified Spontaneous Emission
AWG   Arrayed Waveguide Grating
BBB   Basic Building Blocks
BPM   Beam Propagation Method
CCL   Coupled Cavity Laser
DUT   Device Under Test
DC   Direct Current
DBR   Distributed Bragg Reflector
FP   Fabry-Perot
HHI   Fraunhofer Heinrich Hertz Institute
FSR   Free Spectral Range
IM   Imbalance
InP   Indium Phosphide
IO   Input Output
ISD   Integrated Source Detector
MZI   Mach-Zehnder Interferometer
MO   Microscope Objective
MPW   Multi Project Wafer
MQW   Multi Quantum Well
MMI   MultiMode Interference
PM   Phase Modulator
PS   Phase Section
PD   Photo Detector
PIC   Photonic Integrated Circuit
PTR   Power Transmission Ratio
QCSE   Quantum-Confined Stark Effect
RF   Radio Frequency
RR   Ring Resonator
SEM   Scanning Electron Microscope
SOA   Semiconductor Optical Amplifier
SMSR   Side Mode Suppression Ratio
SMF   Single Mode Fiber
TE   Transverse Electric
TM   Transverse Magnetic
WG   Waveguide

Chapter 1

Introduction

The invention of the semiconductor laser in 1962 [1, 2] opened the way to photonic integration. Only the last two decades, however, complex integrated optical circuits became a reality [3–5], and successfully entered the market [6]. The photonic integrated circuits with the highest number of components at the moment are a transmitter from Infinera [7], and an active passive optoelectronic switch from the Eindhoven University of Technology [8].

Highly sophisticated application-specific methods are developed and used to analyze these circuits, but the building blocks are not characterized individually. Measurements for the most basic parameters such as waveguide loss [9–11] can be imprecise and may suffer from systematic errors. For a broadly used measurement method such as the Fabry-Perot [12], suitable to determine propagation loss, only few authors perform a thorough analysis of the errors that might affect its accuracy with the latest development dating back almost a decade ago [13, 14]. The results of their analysis show how vulnerable this method is to external factors like optical coupling efficiency. However, little is done to propose alternative methods that eliminate the source of these uncertainties.

The aim of this work is to propose alternative measurement methods, based on on-wafer characterization of photonics integrated circuits, that avoid many of the external factors that affect the measurement accuracy.

Here we will design test modules for characterizing the performance of the most important photonic components such as, the passive interconnecting Waveguide (WG), the Phase Modulator (PM), and the Semiconductor Optical Amplifier (SOA) respectively in terms of waveguide propagation loss, phase modulation efficiency, and net modal gain. The above mentioned photonic components, that from now on we call them Basic Building Blocks (BBBs), are chosen as the most simple and basic ones responsible for manipulating the principal light properties such as the phase and amplitude and allow for routing the light on the chip. All the other building blocks originate from them. The proposed measurement methods are aimed to characterize propagation loss of the WG, phase modulation efficiency of the PM and net modal gain of the SOA with a measurement accuracy of respectively 0.2 dB/cm, 0.2 V (2 mA), and 5 cm^{-1}. The above mentioned values represent ambitious measurement accuracies which will contribute to the fast and reliable feedback to the PIC fabrication process.

To achieve these accuracies we analyze thoroughly all the possible uncertainties and compare them with the current state of the art used in academia and industry. The aim of this work is to demonstrate the feasibility of on-wafer characterization through electrical signals only and the benefits of this method. This work, however, is open to new developments and addition. A very important addition to this work is the inclusion of the BBB that is responsible for manipulating the light polarization, the polarization converter. The test module responsible for on-wafer characterization of the polarization conversion efficiency will be included as soon as the polarization converter is included in the generic platform. The presence of the polarization converter in the generic platform will allow to characterize the polarization dependence of all the above mentioned BBBs. Possible future developments to be added to this work may comprise the characterization of other BBBs such as the photodetector in terms of responsivity and/or saturation, or characterize wavelength dependent properties of lasers or optical filters. Given the rapid development and the great potential that photonics offers to ultra wide band communication technologies we predict the most important development of all is going to be the on-wafer characterization of the small signal Radio Frequency (RF) properties of lasers, modulators and photodetectors.

In this chapter we give first a definition of the measurement process, then we make the distinction between direct and indirect measurement methods and finally give an overview over the error sources during measurement.

1.1 Measurement, an (In)formal Definition

In [15] a measurement is defined as the procedure during which a numerical value is assigned to an entity of the real world, after an objective observation of the phenomenon, for representing or describing it. In an ideal measurement a single value is assigned to every single observation of a phenomenon. Real measurement procedures, however, are affected by errors, that reduce the final measurement accuracy.

In this thesis we identify the main error sources and analyze how they affect the final measurement result. We define the measurement, therefore, as *the objective operation that assigns a range of values to an entity of the real world*. This range of values includes many sources of uncertainty. This measurement definition, which accounts for the uncertainty, is similar to the one given in [16].

1.2 Elements of Measurement Theory

Let E be a manifestation of a set of entities (called as well a quality, property, attribute or parameter) of an object of the real world $E = \{e_1, ..., e_n\}$, and let ϕ be a set of empirical relations on E, $\phi = \{\phi_1, ..., \phi_m\}$. The system $T = \langle E, \phi \rangle$ is called the empirical relational system. A similar system, $Q = \langle N, \theta \rangle$ between the set of real numbers, N, and a set of relations $\theta = \{\theta_1, ..., \theta_m\}$ defined on N, is called the numerical relational system. The measurement is the process, that,

after an objective observation, assigns a numerical value to a natural entity [15].

$$M : E \to N \tag{1.1}$$

We show, through a simple example, how these abstract concepts apply to the previously introduced definitions. Let us consider a generic object A. The following entities can be defined on A: mass, volume and density, thus, $E_A = \{m_A, V_A, \rho_A\}$. The numerical values of the first two entities are assigned after a direct reading of the measurement instrument, $m_A = M_m(A)$, and $V_A = M_V(A)$. The numerical value assigned to the last entity, the density, is obtained by the numerical relation $\rho_A = m_A/V_A$.

1.3 Direct and Indirect Measurement Methods

In photonic integrated circuits the measurement is the process during which a numerical value is assigned to a given optical or electrical property, also referred to as parameter. We distinguish between primary and secondary parameters. The primary parameters are those of interest that we want to quantify through the measurement procedure. The secondary parameters are all the other parameters related to the photonic integrated circuit in consideration.

Returning to our example, in case we are interested in knowing the density of the object A, ρ_A is the primary parameter, whereas m_A and V_A are secondary parameters. But we could be interested in the mass of object A, thus in this case m_A would be our primary parameter and V_A and ρ_A secondary parameters.

In literature several ways to classify the measurement methods exist. Here we consider the classification between direct and indirect measurement methods.

- *The **Direct measurement method** is any measurement method where the numerical value assigned to the entity of interest is directly measured (read) at the instrument.* In our example, the measurement of the mass, m_A, by comparing the object A to the standard, is an example of a direct measurement. The same holds for measuring the volume, V_A. An example of such a method in photonic integrated circuits is the phase modulator switching curve measurement. During a voltage sweep we read the voltage that corresponds to the minimum power recorded at the output of the Mach-Zehnder interferometer. This method is discussed in detail in Chapter 5.

- *The **Indirect measurement method** is any measurement method where the numerical value assigned to the entity of interest is given by the value of the other directly measured entities, and the numerical relation defined on them.* In our example, the measurement of the density ρ_A, by measuring m_A and V_A, and knowing the numerical relation, $\rho_A = m_A/V_A$, is an indirect measurement. An example of such a method in photonic integrated circuits is the well-known Fabry-Perot measurement method applied to determine the insertion loss of any passive 2 port device [12]. The secondary parameter, the output power ratio between the maximum and minimum values, is measured while performing a wavelength sweep at the input of the cavity. Through a numerical relation the parameter of interest (the primary
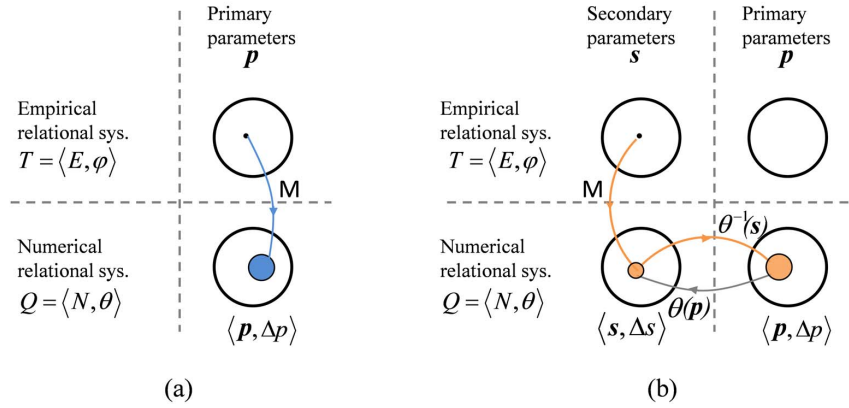
FIGURE 1.1: Schematic representation of direct (a) and indirect (b) measurement method.

parameter) insertion loss, is asserted. This method is discussed in detail in Chapter 4.

In Figure 1.1 (a) a schematic representation of the direct measurement is shown, whereas in Figure 1.1 (b) that of an indirect measurement.

The set of entities, that from now on we call set of parameters, $E = (s_1, \ldots, s_{n-1}, p)$, is composed of several secondary parameters, $(s_1 : s_{n-1})$, and, most of the time, one primary parameter, p. The set of numerical relations θ defined on N is composed of maximally a few relations: $(\theta_1 : \theta_m)$. These relations, that we call from now on functions, express the interdependence between the parameters.

Each parameter varies within a certain range with respect to its nominal value. We indicate the nominal value of parameter s_j as $\bar{s}_j$ and its range of variation as Δs_j, and in a more compact notation as $(\bar{s}_j, \Delta s_j)$.

The measurement procedure, assigns a range of numerical values to a parameter: $M : e_j \rightarrow (e_j, \Delta e_j)$, which in the case of a direct measurement becomes: $M : p \rightarrow (p_j, \Delta p_j)$, and in that of an indirect measurement: $M : s \rightarrow (s_j, \Delta s_j)$. These numerical values are represented in blue and orange colored regions for respectively direct and indirect measurement.

For measuring a certain parameter usually more than one measurement method exists. Each one of them is determined by its own measurement uncertainty range. If the measurements are performed correctly and the measurement uncertainty range is determined correctly then the measured numerical ranges (assigned numerical range in case of indirect measurement) have a non empty intersection. In Figure 1.2 the orange and blue circles indicate the uncertainty regions of a respectively indirect and direct measurement method for assessing the value of the same parameter. If the two (or more) regions have a null intersection then for at least one of the measurements the uncertainty region or the numerical relation is not accurate enough or the measurement procedure is incorrect.
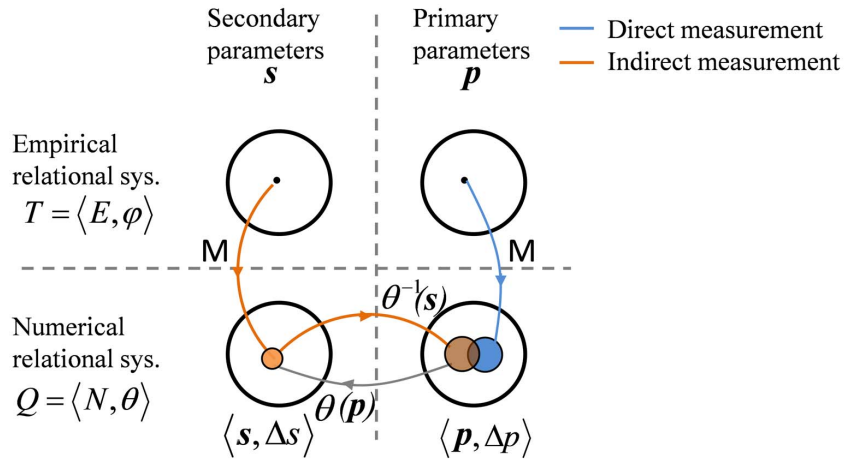
FIGURE 1.2: Schematic representation of direct and indirect measurement methods

1.4 Error Sources

The measurement of the parameter of interest is affected by many errors. The sources of these errors can be of different nature but they all affect the measurement accuracy of the parameter of interest. We distinguish in this thesis two main error sources:

- Errors related to the measurement procedure or to measurement setups.

- Errors introduced from the inaccuracies of the numerical relation in use and the assumption made in obtaining it.

From now on we use the term model for the numerical relations. Both error sources (related to the measurement set-up/procedure and to the model) are analyzed. In this chapter we introduce and treat these error sources in general terms. In each of the following chapters we show in more detail how these errors affect the measurement accuracy of the proposed test modules.

1.4.1 Error Propagation

Errors related to the measurement procedure (or to the measurement setups), and the error propagation in determining the final value of the parameter of interest is described in this section. In the example previously introduced they are the measurement errors in assigning a numerical value to the mass and the volume, and how these errors propagate into assigning a value to the parameter of interest, density.

1.4.1.1 Direct Measurement Method

During a direct measurement, the value of the parameter of interest is directly read at the measurement instrument. In direct measurements the numerical relation is in the form: $p = \theta[M(s_1), ..., M(s_{n-1})]$. In Figure 1.2 this procedure is indicated by

the arrow in blue. In direct measurement the errors in the primary parameter are the final result, therefore, the measurement uncertainty for the direct measurement method is due to the measurement procedure (errors related to the non ideal measurement set-ups used and/or to the non optimal measurement procedure followed by the operator) and is given by

$$\Delta p_M = \Delta m \tag{1.2}$$

With Δm the measurement procedure related errors. In the case of our example, assuming that we are interested in object's A mass, given the accuracy of the weighing machine, say 1%, then the measurement error by applying equation (1.2) is $\Delta p_M = 0.01 = 0.05$ dB The overall measurement uncertainty for direct measurement methods is given by equation (1.2). In Chapter 5 direct measurement methods are applied and analyzed.

1.4.1.2 Indirect Measurement Method

An indirect measurement is a two step process. First the value of one (or a few) secondary parameter is measured and then, through the model describing the relation between the secondary parameter(s) and the primary parameter, the value of the primary parameter is determined, see Figure 1.1 (b). In Figure 1.2 these steps correspond to the two arrows in orange. Errors made in the first step propagate through the second step. Errors generated in the second step, e.g. by model inaccuracy, do not propagate.

The measurement procedure related error in indirect measurement methods is similarly defined to that of direct measurement methods. Since more parameters are measured the square root of the sum of the errors squared is considered.

$$\Delta s_M = \sqrt{\sum_{i=1}^{k} (\Delta m_i)^2} \tag{1.3}$$

where the assumption of statistically independent error sources is made [17].
In the case of our example, given the accuracy of the measurement equipment, say 1% and 2% for mass and volume respectively, their influence on the measurement procedure related errors, described by (1.3), is $\Delta p_M = 0.022 = 0.1$ dB.
In indirect measurements the numerical relation is in the form:
$s_j = \theta[M(s_1), ..., M(s_{j-1}), M(s_{j+1}), ..., M(s_{n-1}), M(p)]$. The numerical relations we are interested in describe the relation between physical properties, thus are *well behaving* functions, that means they are monotonous, continuous and differentiable. Under these conditions it is possible, at least in theory, to invert them and find, therefore, the needed numerical relation in the form of $p = \theta^{-1}[M(s_1), ..., M(s_{n-1})]$. Here $\theta^{-1}()$ denotes the inverse function of $\theta()$.
The influence that the variation of parameter s_j has on the determination of parameter p is given by the formula

$$\Delta p_j = \frac{\delta \theta_j^{-1}}{\delta s_j} \cdot \Delta s_j \tag{1.4}$$

with $\theta_j^{-1} = \theta^{-1}[M(\bar{s}_1), ..., M(\bar{s}_{j-1}), M(\bar{s}_j), M(\bar{s}_{j+1}), ..., M(\bar{s}_{n-1})]$, all the parameters are kept constant to their nominal values except for the parameter of interest, s_j. Δp_j is the variation of the primary parameter, p, due to the variation of s_j, and $\delta\theta_j^{-1}/\delta s_j$ is the partial derivative of θ_j^{-1} with respect to s_j. Δp_j is the linear approximation of θ_j^{-1} at the point $\bar{s}_j$. The smaller the Δs_j the better this approximation is.

The measurement error propagated by the model is, therefore, given by

$$\Delta p_N = \sqrt{\sum_{j-1}^{n}(\Delta p_j)^2} \tag{1.5}$$

with Δp_N the error propagated by the numerical model. If the parameters s_j are statistically independent the square root of the singular errors squared is considered.

In the case of our example, assuming that we are interested in object's A density, given the accuracy of the measurement equipment, say 1% and 2% for mass and volume respectively, the influence that the variation of m_A and V_A have on the determination of ρ_A are given by $\Delta\rho_m = \frac{\delta\theta}{\delta m}\cdot\Delta m$ and $\Delta\rho_V = \frac{\delta\theta}{\delta V}\cdot\Delta V$. Considering the nominal values for mass and volume 1 kg and 5 L respectively the propagated error is $\Delta\rho_N = 0.0064 = 0.03$ dB, calculated by applying equation (1.5). In case the nominal values for mass and volume are 5 kg and 1 L respectively the propagated error is $\Delta\rho_N = 0.1005 = 0.5$ dB.

Finally the overall measurement uncertainty for indirect measurement methods is given by

$$\Delta p = \Delta p_N + \Delta s_M \tag{1.6}$$

In the case of our example, the overall measurement uncertainty is $\Delta p = 0.0284 = 0.13$ dB in the case of 1 kg and 5 L nominal values and $\Delta p = 0.1225 = 0.57$ dB in the case of 5 kg and 1 L nominal values.

In Chapters 4 and 6 indirect measurement methods are applied and analyzed.

1.4.2 Model Inaccuracies

In the previous sections the model describing a physical phenomenon was considered ideal and we focused on the errors introduced by the procedure followed by the operator or by the non idealities of the measurement setup used.

Every model tries to best describe a natural phenomenon. Often natural phenomena are quite complex and many assumptions are made to simplify them into practical models. In real working conditions many of these assumptions may no longer hold, thus an error is introduced.

In this section we try to introduce the problem and make the reader aware of the potential risks present in any model by using a well known example in integrated optics. As already introduced the Fabry-Perot (FP) method [12] is used to characterize insertion loss of any two port device. The FP method is based on an optical cavity in which the device under test is positioned between two reflectors, usually the un-coated facets of the chip. Light coupled inside this cavity travels

back and forth while at each facet it gets partly reflected and partly transmitted. While sweeping the wavelength of the input signal using an external tunable source, the output power goes through maxima and minima. From measuring the ratio between the maximum and minimum transmission (primary parameter), and knowing the cavity length and the facet reflection, the insertion loss (secondary parameter) is estimated. Several assumptions are made in the model. Here we mention a few.

1. The model assumes that only one mode is coupled to the cavity (e.g. the fundamental Transverse Electric (TE) or Transverse Magnetic (TM) polarized mode only).

2. No other intracavity reflections are present inside the cavity.

3. The estimate of the reflection coefficient is correct.

Often, when the input coupling, or the polarization selection is not perfect, higher order TE modes or Transverse Magnetic (TM) polarized modes are present. Another source of error, that the model does not take into account, is the presence of intracavity reflections. Due to processing imperfections the interface geometry can vary or the incidence is not exactly normal. All these parameters are not considered by the model and if not taken into account can produce errors ranging typically from a few tenths up to several dB. A more detailed analysis of these errors is presented in Chapter 4.

Comparing the results obtained by applying different measurement methods increases the confidence that the measurement results are correct if the measurement ranges have a non-empty intersection as shown in Figure 1.2.

It is worth noting that having a non-empty intersection does not mean that the measurement is correct, but an empty intersection means that certainly at least one of the elements in the measurement procedure is not correct.

For each test module or measurement method that we introduce in this thesis we will analyze the main sources of model inaccuracy.

1.5 Generic Measurement Concept

The need to bring down the prototyping and development costs of an innovative Integrated Circuit (IC), and for a short time to market at a reduced investment risk emerged in microelectronics already in the early 70s. The best answer to these requirements was the development of a generic integration process, and the introduction of the Multi Project Wafer (MPW). The concept of the MPW run was introduced at the VLSI System Design Course held at MIT in 1978 [18]. The first MPW run for IC prototyping was offered by MOSIS, established by DARPA in 1981 [19]. Universities, research centers as well as small and medium enterprises soon realized the potential of MPW runs, and made use of them to prove their concepts and ideas at affordable price. Since then many more companies offer IC MPW runs [20], [21].

The photonics community is now following the same steps as electronics. Photonic Integration leads to a significant reduction of the Photonic ICs cost when

fabricated in large volumes, but the R&D costs for developing and testing a chip remain high. The generic foundry model leads to a dramatic reduction of the R&D costs [22, 23]. It is based on building complex Photonic ICs from a small set of Basic Building Blocks, which are used for manipulating the basic light properties, such as phase, amplitude and polarisation, and integrating them in a single chip through a generic process. Very complex and disparate photonic functionalities can be obtained by a clever combination of these simple BBBs.

Two main platforms, JePPIX [24], and ePIXfab [25], are providing access to respectively Indium Phosphide (InP) and Silicon (Si) photonics generic processing through several foundries. The InP based generic foundry model in photonics, developed within the mainframe of several European projects, such as EuroPIC [26] and PARADIGM [27] and national projects, such as MEMPHIS [28], is revolutionizing photonic integration [22, 23].

MPW runs, offered by different foundries, lead to a significant cost reduction in R&D for developing a proof of concept design. The generic foundry model can also lead to a significant reduction of the testing costs by moving a large part of the testing from the circuit (chip) level to the BBB level (generic testing). This is the subject of the present thesis. If the BBBs are within specs, and the design is according to the design rules, the chip functioning should also be correct. Further cost reduction can be achieved by moving from die-level testing to wafer-level testing, which can be done by moving from the optical to the electrical testing domain.

The foundry realizing the MPW run guarantees the performance of the process by verifying on-wafer that the offered BBBs are within specifications. By ensuring the performance of the BBBs the designer has to focus only on the behavior of the circuit as a whole, avoiding, therefore, the design, simulation and verification of the individual BBB components. This speeds up the process and lowers the costs. Therefore, another added benefit of our approach consists of sharing the testing overhead in a MPW run. A track record of the single BBBs performance for every MPW run is obtained.

In this thesis we propose different test modules that are dedicated to on-wafer characterization of the most important BBBs. These test modules go into a generic test cell that is responsible for validating the MPW run.

The main advantage of the MPW runs, together with the low entry costs, is the short manufacturing turnaround time which guarantees a short time to market for the product, vital to the very dynamic semiconductor industry. To reduce the turnaround time the foundries make use as much as possible of standardization and automation. Once the MPW is ready the foundry has to cleave it into individual chips, verify the MPW fabrication by characterizing the generic test-cell, and finally coat the chips and ship them to the respective users.

1.6 Thesis Outline

The principal goal of this thesis is to introduce new concepts in characterizing photonic integrated circuits, fabricated with the generic foundry model, that lead to a significant reduction of the testing costs. This cost reduction is achieved by

moving a large part of the testing from the circuit (chip) level to the BBB level (generic testing). The good functioning of the BBBs is a necessary condition to the overall PIC performance. However, it is not a sufficient condition since it does not consider the interaction and interconnection between the BBBs. If the BBBs are within specs, and the PIC design does not violate any design rule, typical errors due to higher order mode generation or polarization conversion are minimized. The overall PIC performance is ultimately responsibility of the designer. To optimize the later circuit simulations are usually performed.

Further cost reduction can be achieved by moving from die-level testing to wafer-level testing, which requires moving from the optical to the electrical testing domain.

This thesis is organized as follows:

In Chapter 2 the concept of generic test cell and generic measurement setup are introduced. It describes how we propose to reduce significantly the costs in validation and testing by using a generic test cell where the most important building blocks are characterized. A lot of effort is done to make this test cell applicable to different foundries by applying standardization in the optical and electrical input and output. A state of the art measurement setup is developed. This measurement setup is compatible with the standard developed for the generic test cell.

In Chapter 3 we introduce and analyze the integrated light sources that allow us to move from the optical to the electrical characterization domain. These integrated light sources are namely the integrated broad band source that is used in Chapter 6 and the tunable laser source that is used in Chapters 4, 5. Both of them are analyzed in terms of reproducibility limits and the tunable laser in terms of continuous tuning.

Chapter 4 first identifies and analyzes the factors that limit the accuracy achievable with the classical Fabry-Perot measurement method, extensively used to characterize propagation loss of passive components. The second part of this chapter introduces for the first time a fully integrated optical circuit that allows the characterization of the propagation loss of passive waveguide in the electrical domain. This test module achieves with a small footprint (2 mm^2) a good accuracy (± 0.25 dB/cm). This work was published in IEEE Photonics Journal.

In Chapter 5 we propose and analyze two fully integrated optical circuits for characterizing the optical phase modulation efficiency in the electrical domain. The test modules achieve again with a small footprint (<2 mm^2) a good accuracy ($< 6\%$). The novelty of this work will be submitted to the Photonic Technology Letters.

In Chapter 6 we propose an innovative on-wafer characterization method for modal gain of semiconductor optical amplifiers. The footprint of the test module is 4 mm^2 and the accuracy at the maximum gain is very good (gain error less than 6.5%). The novelty of this work was presented at the European Conference on Integrated Optics (ECIO) 2014.

In the last chapter conclusions and future prospects are presented.

Chapter 2

Generic Characterization Methodology

2.1   Introduction

The cost of electronic ICs is dominated by test and assembly into packages. This is even more true for Photonic ICs (PIC) since more properties have to be characterized, and moreover optical properties are more challenging to verify. This is mainly due to the more complex methods required today for characterization of photonic ICs. The higher complexity comes from the characterization nature of PICs through mixed electro-optical signals. The measurement challenge is compounded by the wafer scale production of photonic integrated circuits. Wafer scale testing is, therefore, mandatory for verifying the MPW run as well as for mass-manufactured PICs. It allows cross-wafer characterization, vital for statistical information. The key words are thus standardization and automation even in the wafer validation process.

Besides the generic manufacturing and the generic BBBs, we introduce in this chapter the concept of the generic test cell, and of the generic setup. The generic test cell consists of dedicated test modules, meant for checking the performance of the BBBs that are responsible for manipulating the light properties as phase and amplitude and for routing the light in the chip. By validating the BBBs responsible for manipulating the above mentioned light properties the MPW run itself is validated. The generic test setup is a state of the art testbed realized to fully exploit the potential of the generic test cell in terms of measurement accuracy and automation. This generic test setup can be used as well for the characterization of other PICs, realised in the MPW runs that comply with the standard for the optical and electrical ports.

2.2   Wafer-level Testing

As already introduced in the introduction chapter the generic foundry model leads to a significant cost reduction not only in R&D but as well in testing. The cost reduction in testing is obtained by moving a large part of the testing from the

circuit (chip) level to the BBB level (generic testing), and by going from die-level testing to wafer-level testing, which requires moving from the optical to the electrical testing domain.

Research institutes and companies already in the early nineties have shown on-wafer characterization of application specific devices, in the optical [29], as well as in the electrical domain [30]. A good overview of the on-wafer characterization for application specific PICs can be found in [31]. On-wafer characterization of photonic ICs, fabricated through a generic process, however, is found only in recent years. The first effort in wafer scale characterization is described in [32] where silicon ridge waveguides, processed in a generic fabrication process, are characterized in terms of propagation loss in the optical domain. A more comprehensive wafer scale characterization used for validation of a generic platform is described in [33]. In both works the characterization was performed on test wafers rather than on a generic MPW run, using grating couplers to couple light in and out of the wafer and electrical probes to test the photo detectors and modulators.

To realize on-wafer characterization for validating generic ICs we follow a systematic approach and take advantage of the excellent active properties offered by Indium Phosphide (InP). The systematic approach consists of designing a dedicated generic test cell that contains test modules for characterizing the performance of the most important BBBs, namely the passive interconnecting waveguide, the phase modulator, and the semiconductor optical amplifier. Each of the dedicated test modules comprises an integrated light source and an integrated detector. The integrated input and output offer the possibility for validation of optical properties in the electrical domain. By shifting the characterization from the optical to the electrical domain the critical and time consuming optical alignment is avoided and test cells can be characterized on-wafer, before cleaving and dicing. The opportunity of characterizing all the BBBs in the electrical domain through electrical signals only opens the way to a much simpler automated measurement procedure, vital to quick and accurate cross-wafer characterization of the BBBs. To achieve this all the electrical contacts are routed to a predefined test cell area and spaced with a fixed pitch suitable for simultaneous characterization through a multi-probe card. The generic test cell is repeated several times across the wafer. At every touchdown of the multi-probe card the specific test cell is characterized.

In the PARADIGM and MEMPHIS projects [27, 28] MPW runs are provided by three foundries: Oclaro [34], Fraunhofer Heinrich Hertz Institute (HHI) [35], and Smart Photonics [36]. These foundries, among many similarities, have several differences too:

- Different refractive index contrast, therefore, different BBBs size

- Different BBBs (e.g. Electro-Optic vs. Thermo-Optic Phase Modulator)

- Different platforms (n+ vs. Semi Insulating platforms -*i.e.*- one or two pads for active BBBs)

Each of them uses a similar generic test cell that characterizes the BBBs responsible for light routing, phase modulation, and light amplification (WG, PM, SOA). Every generic test cell is composed of two sections. The main one dedicated to on-wafer testing in the electrical domain and the other dedicated to characterization

Experimental electrical measurement

"Classical" optical measurement

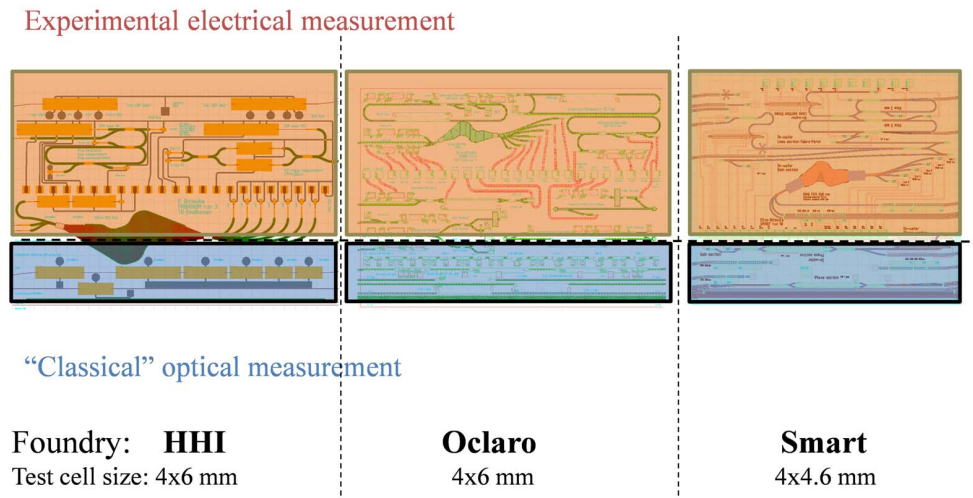| Foundry:	**HHI**	**Oclaro**	**Smart**
Test cell size: 4x6 mm		4x6 mm	4x4.6 mm

FIGURE 2.1: Designed generic test cells for the different foundries. Each test cell contains all-integrated test modules as well as test structures suitable to be measured with classical methods.

of the same BBBs through classical measurement methods represented in Figure 2.1 respectively in orange and in light blue.

During test module design a primary goal was to realize test modules that can be used in all the three foundries and that are transparent to the platform in which they are implemented, despite the differences of the three foundries. This is achieved by using the same characterization concept and testing protocol for all the foundries.

- The *characterization concept* for testing a given BBB, is the same for all the three foundries at the level of a schematic description of the test module. For example, for the WG (as we will see in Chapter 4) the same characterization concept is used: an integrated tunable light source, a specific optical cavity, and an integrated Photo Detector (PD). In the Oclaro process and the new HHI process the tunable source is a Distributed Bragg Reflector (DBR) laser, whereas in COBRA (gratings are not available) a coupled cavity laser is used instead. This difference in the test module is hidden by the characterization software.

- The *testing protocol* is given by the measurement procedure used and the parameters extracted for the BBB validation. Using the same example, the testing protocol consists of:

  - Tune the wavelength of the integrated laser
  - Record the typical oscillating response of the ring cavity at the detector
  - Extract the maximum and minimum transmitted output power
  - Determine the propagation loss.

Even though each test module uses the same characterization concept and testing protocol, because of the differences between the foundries, implementing them in
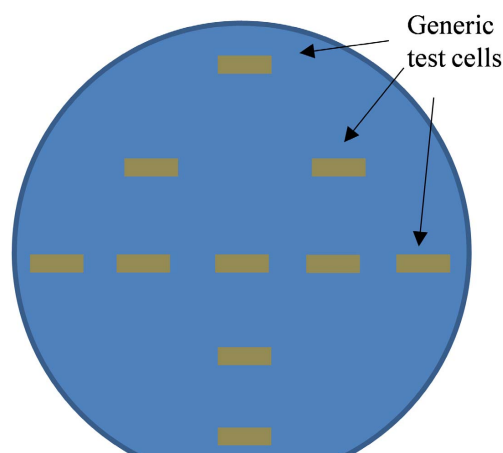
FIGURE 2.2: Proposed distribution of the generic test cell in a 2 inch InP wafer.

the different platforms, requires the use of a different light source, different BBBs realizing the modulation of phase, and different number of contacts used.

The use of a similar test cell facilitates convergence towards a further inter-foundry compatibility. A layout of the generic test cell for each of the foundries is shown in Figure 2.1. The details of each of the dedicated electrical test modules present in the generic test cell together with a comparison with the classical measurement methods already in use are explained in the following chapters of this thesis.

As we will see in this thesis the minimum dimensions for an all-electrical generic test cell suitable for MPW run validation is 2x6 mm (12 mm^2). We propose that the generic test cell is repeated at least 10 times in a 2 inch or 20 times in a 3 inch wafer (<10 % wafer area). The test cells should be distributed uniformly on the wafer in such a way that radial dependency of the BBBs performance can be determined. In Figure 2.2 the proposed distribution of the generic test cells in a 2 inch MPW wafer that guarantees an adequate cross-wafer characterization is shown.

By having the generic test cell repeated 10 times on the 2 inch wafer (20 in the 3 inch wafer) the minimum amount of data to perform a statistical analysis of the singular BBBs performance and retrieve such data as the mean value of the measured parameter, the standard deviation, the variance etc. would be possible. At the moment of this thesis however, with only one exception that we will see in the next chapter, no statistical data is present as the amount of PICs where the measurement are performed is not sufficient to perform such analysis. The goal of this work is to pave the way to automated generic testing through easy measurement procedures and small footprint test modules.

At the moment properties of BBBs in the generic test cell are characterized only with DC currents and voltages. In the future an update of the generic test cell to characterize basic RF properties of BBBs should be implemented.

2.2.1 Standardized IO Interface

The test modules of the generic test cells for the different foundries suitable for on-wafer testing are designed with the same characterization concept and the same testing protocol. Their layouts, however, reflect the differences between the foundries (different BBBs, different BBBs size, different number of contacts, etc). In this section the effort made to standardize the electrical and optical interfaces is described.

2.2.1.1 Standardized Optical IO

The wafer-level generic test cells have very few optical IO ports. The classical test structures are present or used to enhance the testability of the electrical test modules (for partially characterizing different parts of the test modules). To standardize the optical IO the standard already present at COBRA for many years is adopted.

- Optical ports are positioned at a pitch of 25 μm or an integer multiple of it.

- Straight as well as angled (7°) optical ports are allowed. The only possible angle facet direction is shown in the inset of Figure 2.3.

The waveguides exit straight or angled dependent on whether on-chip reflections are desired or not. The 7° angled waveguide minimizes the back reflections from the InP-air interface. This angled facet is realized where back-reflection is harmful as for example in the test structures used for modal gain characterization of SOAs. Due to the MPW run design rules the direction of the left and right angled facets is predefined as shown in the insets of Figure 2.3. The choice of 25 μm pitch is a trade-off between space requirements and low optical crosstalk between adjacent waveguides [37].

2.2.1.2 Standardized Electrical IO

The three wafer-level generic test cells have all the electrical contacts, used for driving the integrated inputs and outputs of all the dedicated test modules, routed to a specific chip area of the on-wafer testing part of the generic test cell. For the electrical contacts more freedom is present as little has been done in standardization. The standard in defining the electrical ports is:

- Electrical ports (pads) are positioned at a pitch of 250 μm (150 μm for Smart).

- Total number of electrical ports is 24.

- Electrical port size is 100x100 μm^2.

The number of electrical contacts required for driving all the dedicated test modules varies between the foundries. The highest number of contacts is required at the HHI foundry due to their semi insulating platform (top ground contact needs to be routed for each electrically driven BBB). For HHI 24 contacts were needed
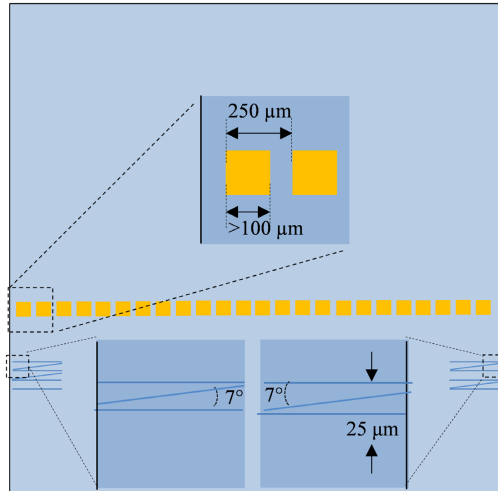
FIGURE 2.3: Schematic of the standardized optical and electrical interfaces of the generic test cells.

to drive all the test modules. This number of contacts was used for the other two foundries too as a need to standardize the electrical interfaces. The pitch, however, varies. For Oclaro and HHI, where the PIC longitudinal dimension is 6 mm a pitch of 250 μm is chosen. To fit the 24 electrical contacts in Smart, given the lateral dimension of its PIC 4.6 mm, a 150 μm pitch is chosen. The pad size is chosen to be 100x100 μm^2 for an easy and good electrical contact. In Figure 2.3 the schematic of the standardized electrical IO are shown.

A smaller pitch makes the alignment procedure difficult and time consuming. However, probe cards with a pitch down to 60-70 μm can be found in the market. Therefore, in the future, when fully automated characterization will be applied a reduction in pitch size is predicted.

2.3 Die-level Testing

Wafer-level testing is suitable for a fast and automated characterization of the most important BBB: waveguide, phase modulator and semiconductor optical amplifier. It is also needed for characterization across the whole wafer, especially useful in a commercial environment where statistical data and yield are important. However, in case access to the optical signal is needed then the die-level testing is used. At the die-level generic test cell test structures are provided not only for the BBBs but even for composite building blocks like a shallow to deep transition, isolation section, modefilter, 1x2 and 2x2 Multimode Interference (MMI) couplers etc.

The die-level testing provides means for cross-checking the characterization data given the availability of the optical ports and the possibility of accessing the optical signal. However, the die-level generic test cell can only be characterized once the wafer is cleaved and diced, thus later on in the production stage. Moreover, given the need to optically align signals for input and output the characterization procedure is slower and less suitable for automation.
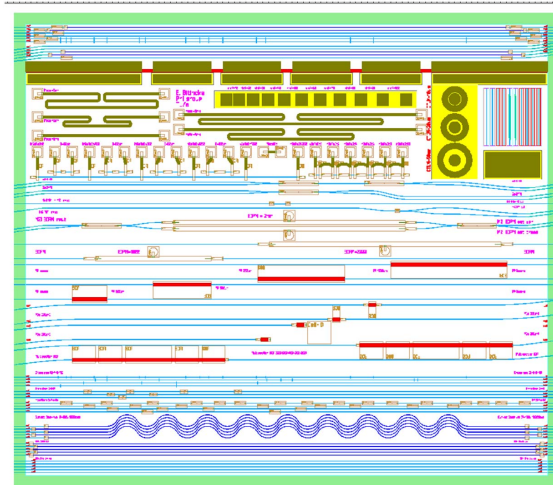
FIGURE 2.4: Die-level generic test cell designed for Smart foundry.

In Figure 2.4 the die-level generic test cell, designed for the Smart foundry, is shown. This die-level test cell is not present at the other foundries, where foundry specific test cells are present instead.

The die-level generic test cell uses the same optical and electrical IO port standard introduced in Section 2.2.1.

The die-level testing, with its mainly optical domain characterization, does not replace but is rather complementary to the fast and automated validation in the electrical domain that the wafer-level testing offers.

2.4 Characterization Throughput

In this section we estimate the throughput improvement that is achievable using wafer-level testing compared to die-level testing when characterizing 10 test cells. Each test cell has dedicated test modules for measuring: waveguide propagation loss, phase modulation efficiency, and modal gain of a semiconductor optical amplifier.

To characterize each of the test modules in the die-level testing the first step is aligning optical and/or electrical ports, then performing the measurement. Typical aligning and measuring times needed for each test modules are shown in table 2.1. The phase modulator has the longest alignment time which is estimated to be 25 min. It includes the alignment of two lensed fibers, and at least one probe for electrical contact. For the waveguide loss aligning two fibers is required with an estimated time of 15 min, whereas for the amplifier one fiber and one electrical contact with a similar estimated alignment time of 15 min. The typical measurement for the waveguide and phase modulator consists of a wavelength or voltage sweep that takes no longer than a few minutes. However, to characterize the semiconductor optical amplifier a wavelength scan with an optical spectrum analyzer for any applied current is needed, therefore, a longer measurement is required (50 min).

Optical (manual) characterization		
BBB	Align. time (min)	Meas. time (min)
WG	15	2
PM	25	2
SOA	15	50
total charact. time	55	54
charact. throughput	0.05 wafers/hour (0.5 PICs/hour)	

Electrical (automated) characterization		
WG	-	2
PM	-	2
SOA	-	2
total characterization time	15 (probe align.)	6
throughput	1 wafer/hour (10 PICs/hour)	

TABLE 2.1: Optical vs. electrical characterization throughput

To characterize each of the test modules in the wafer-level testing a first manual alignment of the probe card is needed (estimated time 15 min). The other test cells are automatically aligned, therefore, in a fraction of the manual alignment. Characterizing the waveguide loss and the phase modulator a current or voltage sweep is required with typical characterization times similar to the die-level testing. The characterization of the semiconductor optical amplifier, however, is performed only at a few points in the gain spectrum thus much quicker if compared to the die-level testing.

As can be seen from Table 2.1 the wafer-level testing performed in the electrical domain speeds-up the MPW run validation by at least a factor 20. This improvement in characterization throughput is fundamental to the successful commercialization of generic PICs in general, and that of MPW runs in particular.

2.5 Generic Test Setup

Testbeds dedicated to characterization of application specific PICs, optimized and automated to increase throughput, are common in the photonics semiconductor industry [29–31]. Testbeds suitable for characterization of generic PICs, however, are not yet present, whereas in academia, testbeds are often manually operated by manipulating a typical 3D stage [38]. The manual operation affects the stability and is not optimal when fast measurements are required.

To fully benefit from the measurement speed-up offered by the generic testing methodology and generic test cell a state-of-the-art testbed, called the generic test setup, is developed within the PARADIGM project according to the schematic shown in Figure 2.5.

The generic setup is suitable for die-level testing. Another task of the generic setup is to characterize other PICs, realized in the MPW runs whose optical and/or electrical interfaces comply to the same standards. The generic test setup can be
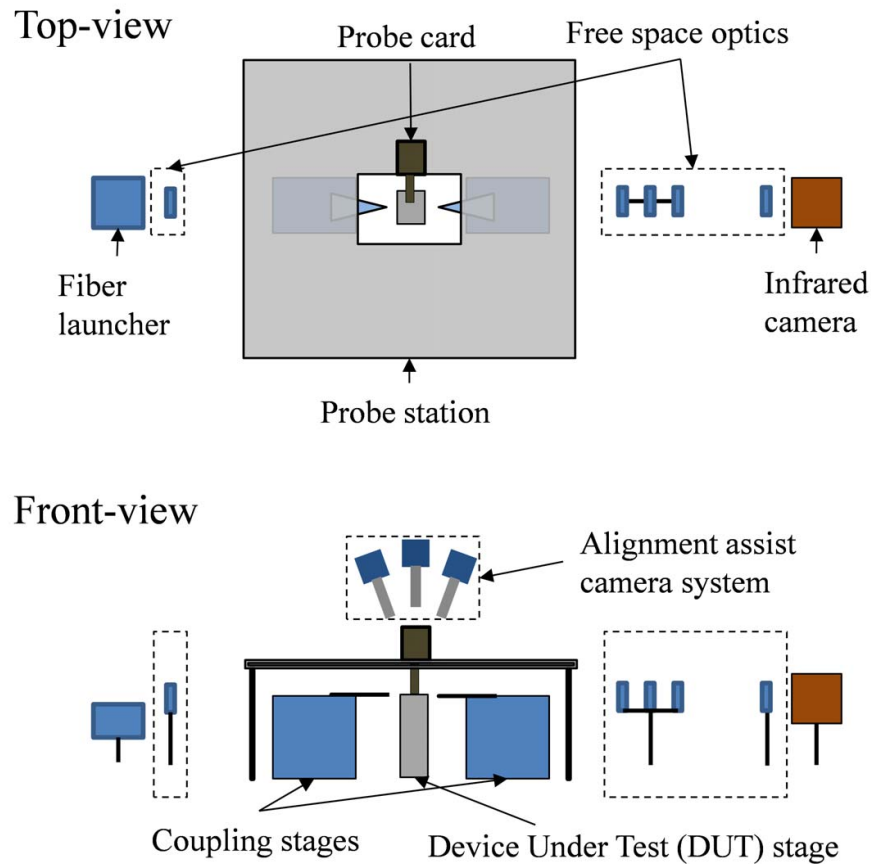
FIGURE 2.5: Schematic representation of the developed generic setup.

used to perform emission, detection and transmission measurement, in the optical as well as in the electrical domain.

2.5.1 Standardized IO Interface

One of the main requirements for a state-of-the-art generic setup is the throughput defined as the number of PICs characterized per hour. To this purpose a standard IO for the optical and electrical interfaces of the setup is defined.

In an industrial environment where characterization of large number of PICs is performed, standardized IO ports are less important as long as the right probe for the electrical-optical IO ports is used.

The standardized IO ports, offered by the generic setup, are the same as the ones described in Section 2.2.1, thus they coincide with those of the generic test cell since one of the principal tasks of the developed generic setup is the fast and accurate validation of the MPW run through the characterization of the generic test cell.

Optical IO constraints:

- Optical ports have to be positioned at a minimum pitch of 25 μm or an integer multiple of it.

(a)   (b)
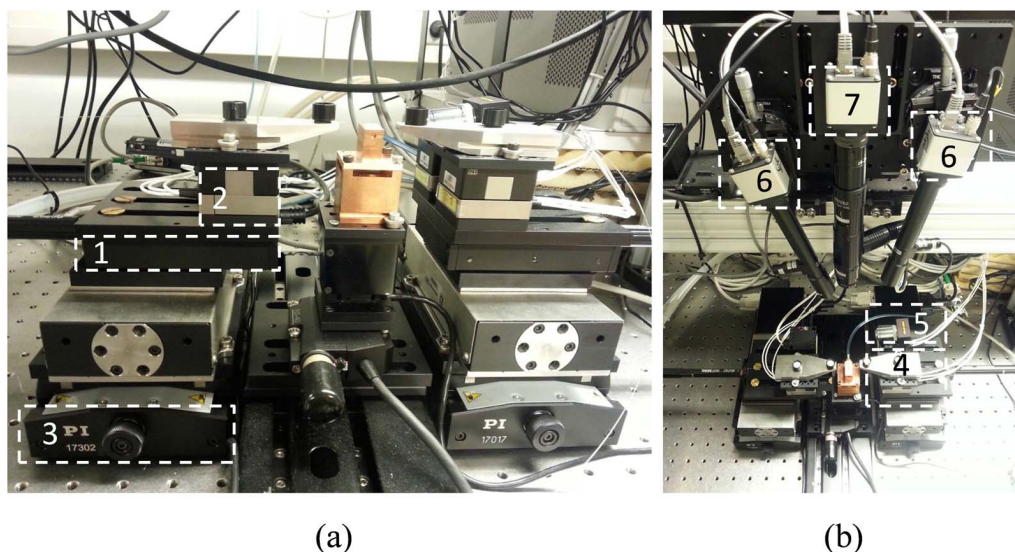
FIGURE 2.6: Photograph of the developed generic setup. In (a) detailed picture of the motorized positioners and in (b) an overall top view of the setup that shows the imaging system too.

- Straight as well as (7°) angled optical IO are supported.

- Spot-size diameter is 3 μm.

Electrical IO constraints:

- Single or multiple DC electrical ports are allowed.

- In the case of multiple DC ports the pitch is 250 μm.

- Each interface must have a contact pad not smaller than 100x100 μm^2.

Other specs of the generic setup are:

- Only one fiber or microscope objective per facet is offered.

- Maximum number of electrical ports is 24.

- The maximum chip size allowed is 6x6 mm^2.

PICs realized through MPW runs should comply with the opto-electrical IO standards to enable quick and accurate characterization with the generic setup.

2.5.2   Generic Setup Accuracy Analysis

The generic test setup shown in Figure 2.6 is developed to speed-up and simplify the measurement procedure and improve the measurement accuracy of PIC developed in a MPW run which satisfies the constraints specified in section 2.2. The two principal factors that slow down the measurement are:

- Finding the optical axis by aligning the two lensed fibers/microscope objectives back to back and subsequently introducing the PIC between the fibers (microscopes) and restoring the optical axes (which is a time consuming procedure). To avoid it motorized stages with long range and high repeatability are used. [38], see Figure 2.6(1). The homing repeatability of these stages ± 1 μm assures the preservation of the optical axis.

- To couple light in and/or out of the chip the two principal methods are either using a microscope objective or a lensed fiber. Due to the generic nature of the setup we offer the possibility of choosing the coupling method without rearranging the setup every time. This is achieved by combining two small range (80 μm) but high resolution (2 nm) 3D stages: one used for the lensed fiber coupling and the other for the microscope objective. The stages are independent of each other, see Figure 2.6(2), and mounted on a long range stage (10 cm), Figure 2.6(3). The long range stage (3) allows switching from lensed fiber to microscope objective without dismantling the setup. The operator can choose a lensed fiber or a microscope objective as coupling element, Figure 2.6 (4) (5), for both, the left and the right side coupling.

Control of the input polarization state in free space and fiber is obtained by use of a free space polarizer and a fiber-bench polarization controller respectively. In output a second polarization rotator can be used to filter out unwanted polarization state.

The following features are added to simplify the measurement and reduce the level of user experience required in optical characterization

- Three high resolution cameras are used for monitoring the left and right coupling, Figure 2.6(6), and for focusing on different PIC areas of interest, Figure 2.6(7).

- A user friendly interface, that standardizes and simplifies the control for all the stages was developed see Figure 2.7 [1].

The last requirement for the generic measurement setup is to ensure a high accuracy. Therefore, stages with the following characteristics were chosen

- Stages with a motorized control, thus reducing oscillations and instability introduced by the operator using manually controlled ones.

- Stages with very high resolution (2 nm) and low hysteresis, and with a feedback control loop, optimal for an accurate optical coupling, Figure 2.6 (2).

2.5.2.1 Generic Setup Time Stability

To check the stability and accuracy of the setup a few experiments were carried out. The first one is shown in Figure 2.8. It shows the stability over time of an

---

[1]We designed a Labview software that controls all the different positioners of the generic setup whereas the development was done at the Equipment and Prototyping Center (EPC) at TUE.
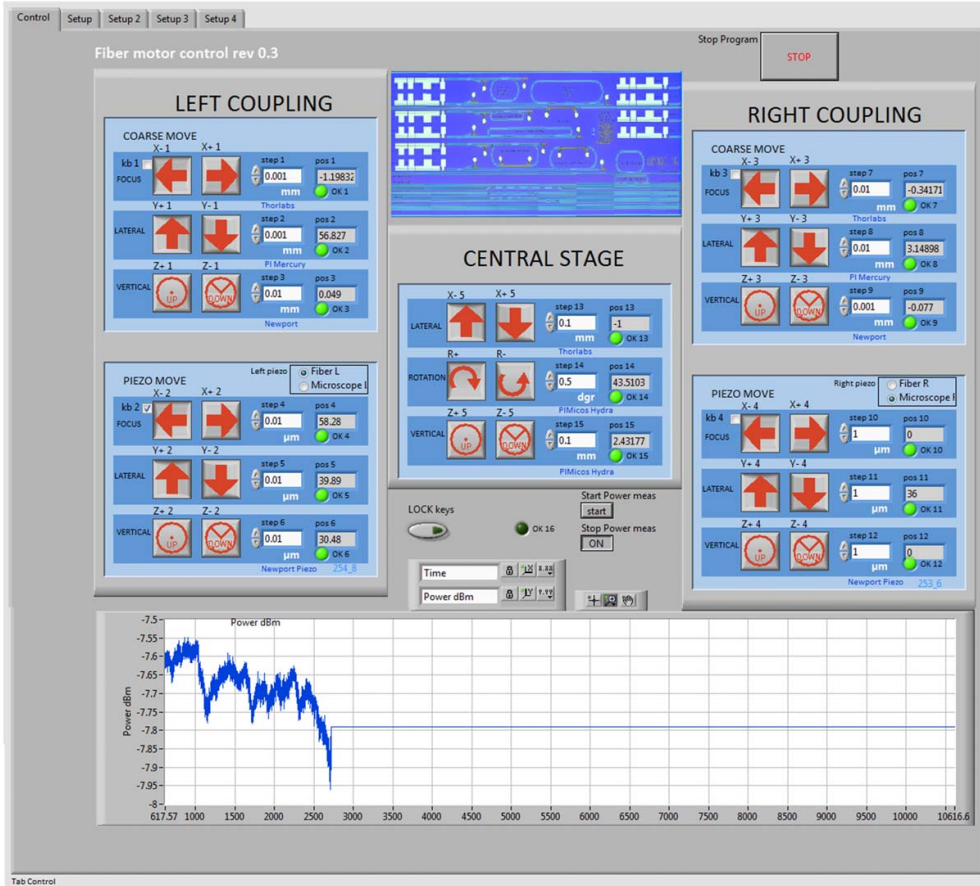
FIGURE 2.7: User interface of the Labview control for the several motorized stages. The user interface is organized in four sections: control of the left coupling stage, of the right coupling stage, and control of the central stage where the PIC is positioned. The last section monitors the power coupled at the output while aligning.

optical measurement. For this experiment first two lensed fibers were aligned back-to-back by maximizing the collected power. Then the power was monitored for several minutes. During this measurement the wavelength and the intensity of the 81940A tunable HP laser were kept constant. The same procedure was repeated by aligning a straight waveguide in a chip with anti reflection coating applied at its facets. In the fiber back-to-back measurement the power stability is within 0.02 dB during the 10 min measurement whereas when between the two lensed fibers a chip with anti-reflection coatings applied at its facets is positioned a maximum power drop of 0.2 dB is observed. These two measurements are compared and normalized with respect to the case when the two fibers are connected through the E2000 connector assembly, see Figure 2.8. The 0.2 dB of power drop is due to a horizontal drift of 100 nm of the correspondent stage. Most of the measurements take only a few minutes, with, therefore, an acceptable power drop. In case a longer measurement is needed simple auto alignment scripts can be easily implemented to motorized stages.
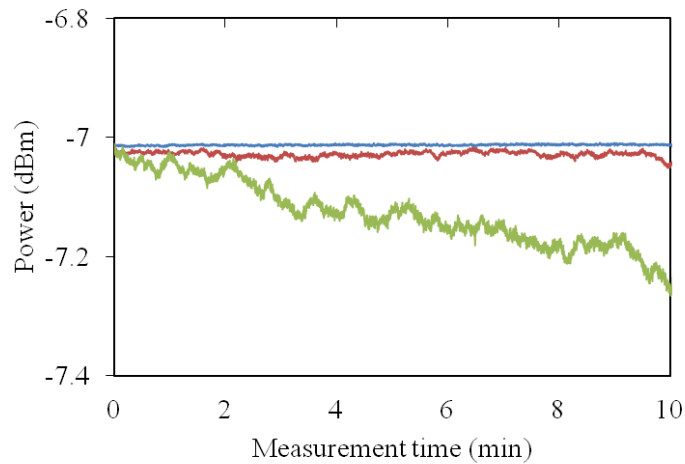
FIGURE 2.8: Time stability measurement with two lensed fibers back to back (red) and through a straight waveguide (green) compared to the fibers connected through a E2000 fiber connector (blue). The three traces are normalized with respect to the output power measured through the E2000 connector.
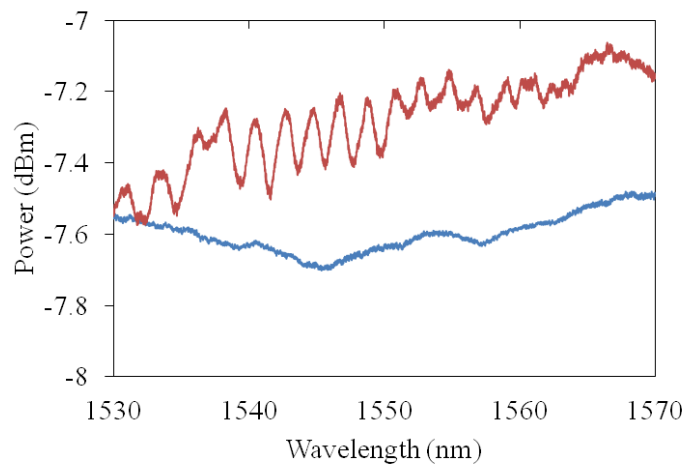
FIGURE 2.9: Normalized uniformity measurement over the C-band with two lensed fibers back-to-back (blue) and through a straight waveguide (red).

2.5.2.2   Generic Setup Wavelength Uniformity

Another important figure of merit of the setup is its uniformity over the C-band (1530-1565 nm) while performing a measurement. To assess it a wavelength sweep of the external tunable laser over the C-band was done as shown in the Figure 2.9. The measured power coupled at the output fiber was recorded with a power meter. The wavelength uniformity over the C-band during a measurement with the fibers in the back-to-back configuration is within ±0.05 dB, and in the case when light is coupled in and out of a straight waveguide with anti reflection coated facets this stability degrades up to ±0.2 dB. During measurement a strong dependence between the oscillation depth present in Figure 2.9 and the input angle of the lensed fiber was observed. These oscillations are attributed to higher order modes

coupled to the cavity since as we will see in Chapter 4 the presence of higher order modes inside the cavity is the principal cause of oscillating transmission. An angled input excites the first order mode, therefore, causes the oscillations.

2.6 Conclusions

The concept of generic wafer-level and die-level testing were introduced. The first performed in the electrical domain and the other in the optical domain. Both of them apply the same optical and electrical standard IO ports. Dedicated test cell suitable for wafer-level testing for the three foundries were presented. The potential throughput improvement that can be achieved by using the wafer-level testing compared to the die-level testing is also given.

Finally the development of a state of the art generic setup for die-level testing is described. Its motorized stages allow for stable and reproducible characterization. They are suitable for automated measurements too.

Chapter 3

Integrated Light Sources

3.1 Introduction

As already mentioned in Chapter 1 the actual measurement methods applied to characterize optical integrated circuits can be inaccurate [9, 13, 14]. The inaccuracy is mainly introduced by the external optical input that is responsible for the excitation of higher order modes or the selection of a non ideal state of polarization. To avoid the problems related to the critical optical coupling we shift the characterization from the optical to the electrical domain using integrated light sources. By integrating the light source on the chip we reduce significantly the alignment time, which is another draw-back of the optical characterization.

In this chapter we introduce the integrated sources that are used throughout this thesis. There are three types: the semiconductor optical amplifier broad band source, the Distributed Brag Reflector (DBR) tunable laser, and the coupled cavity laser. In [22, 39] is described the SOA used in our technology, and in [40] a more thorough analysis and few characterization methods for the SOA are presented. A detailed description of the DBR lasers can be found in [40–42], and in [43] a detailed description and characterization results of the coupled cavity laser are presented.

All integrated sources are connected to an optical cavity or optical filter and finally to an integrated Photo Detector [44]. In this chapter we analyze the broad band source and detector in terms of reproducibility limit, and the integrated DBR laser source and detector in terms of reproducibility limit and tuning capability, since these parameters, as we will see in the following chapters, are of primary importance when determining the measurement accuracy of the test modules comprising these two sources. The parameter of interest when considering the coupled cavity laser and the respective test module that it is included in is the side mode suppression ratio.

3.2 The Integrated Source Detector Method

Several test modules that are proposed for integrated measurement comprise the integrated source, a Device Under Test (DUT), and an integrated detector. The semiconductor optical amplifier, used as integrated input, converts the electrical
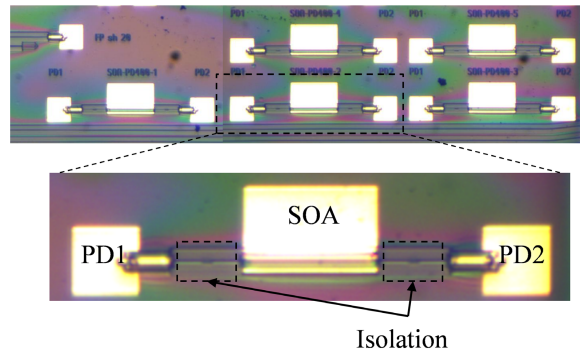
FIGURE 3.1: Microscope photograph of the integrated source detector proposed and in the inset the zoom of one of them.

signal, provided through an electrical probe, to an on-chip broad band optical signal. The integrated detector performs the opposite function, it converts incoming light signal into electrical signal (photocurrent), that is collected by another electrical probe.

The absolute transmission value measured by the photodetector is not only dependent on the device under test but it is also dependent on the emission of the integrated SOA and on the photodetector responsivity. The accurate measurement of the DUT is thus dependent on the reproducibility of the integrated source and integrated detector, that from now on is called Integrated Source Detector (ISD) structure.

To determine the reproducibility limit of the ISD several identical structures composed of an integrated broadband source and an integrated detector are used in Smart run 9 [24]. In the analysis that follows we are interested in the reproducibility of the Integrated Source Detector as a whole. The reproducibility limit of the ISD is the ultimate resolution limit of all the comparative transmission methods applying it.

3.2.1 Structure Description of the Integrated Source Detector

Measurement resolution *is the smallest variation of an optical parameter that is actually measurable.* It is clear from the definition that the resolution limit is strictly related to the measurement procedure and measurement instruments used. The reproducibility limit of the ISD is, therefore, the ultimate limit of the measurement resolution achievable with this method. To determine the reproducibility limit of the ISD, five of such identical structures are proposed, see Figure 3.1. In the inset, details of such a structure are shown.

The more ISDs, and the better the statistical description of the ISD, the more confident are we on the measurement resolution. The number of structures we implemented is the maximum possible within the allocated space on the test cell. The ISD structure consists of:

- 200 μm long SOA

- photodiode

- isolation section

- passive interconnecting waveguide

The SOA length, 200 μm, is chosen as a trade-off between small footprint and sufficient output power to characterize the DUT. The output power expected from the SOA (> -30 dBm) is often enough for integrated measurements as the integrated detectors have a dark current of a few tenths of nA at -2 V bias, therefore, signals with an intensity down to -40 dBm can be measured. If longer SOAs are present they are always a multiple of the smallest 200 μm SOA. The photodetectors are 60 μm long, sufficient to fully absorb the incoming light. The SOA is defined in the weak waveguide cross section, whereas the photo detector is defined in the deep one. An isolation section is included to electrically isolate the SOA and the PD. Detailed information on the isolation section can be found in [22].

To prevent that spurious reflections inside the ISD cause the lasing of the SOA a second full absorbing PD is used on the other side (together with an isolation section). The second PD serves two purposes: prevents the lasing of the SOA and at the same time acts as a second monitor on the SOA activity, therefore basically doubling the number of available ISD structures.

3.2.2 Experiments

The test structure shown in the inset of Figure 3.1 comprising one SOA and two detectors, one on each side, is repeated five times, as can be seen in Figure 3.1. Therefore, 2 ISD structures are obtained for each SOA for a total of 10 ISDs. All the 10 ISD structures are used under the same operating conditions. The SOA is pumped up to a current density of 10 kA/cm^2 starting from 1 kA/cm^2 in 10 steps of 1 kA/cm^2 where the PD is biased at 0 V. The applied bias at the PD is kept at 0 V to reduce the dark current to a minimum, by therefore, increasing the PD measurement range by more than 10 dB with respect to the case when the PD is biased at -2 V (dark current at -2 V is several tens of nA). The difference in photocurrent recorded at the PDs when they are biased at 0 V or at -2 V while pumping the SOA is less than a few percent, and moreover, it does not change the reproducibility performance of the ISD devices. Increasing the measurement range of the PDs, on the other side, is quite useful during measurement.

The maximum current of 10 kA/cm^2 is a typical pumping current to drive the SOA to saturation. The ISD structure however, is not optimal to measure SOA saturation, whereas from the test module proposed in Chapter 6 such information can be retrieved. The bias voltage of 0 V used for the PDs is sufficient to absorb more than 95% of the incoming light (a few percent more light is absorbed if the detector is fully depleted by applying -2 V). The photocurrent detected in the PDs is recorded. This is repeated for all the 10 ISD structures. The spread of the photocurrent measured by the PDs with respect to the average (when their SOAs work under the same operating conditions) determines the limit with which we can perform our integrated measurements.

In Figure 3.2 is shown the reproducibility limit of 40 ISDs for typical current densities applied at the SOAs 1, 3 and 5 kA/cm^2, respectively depicted in red,
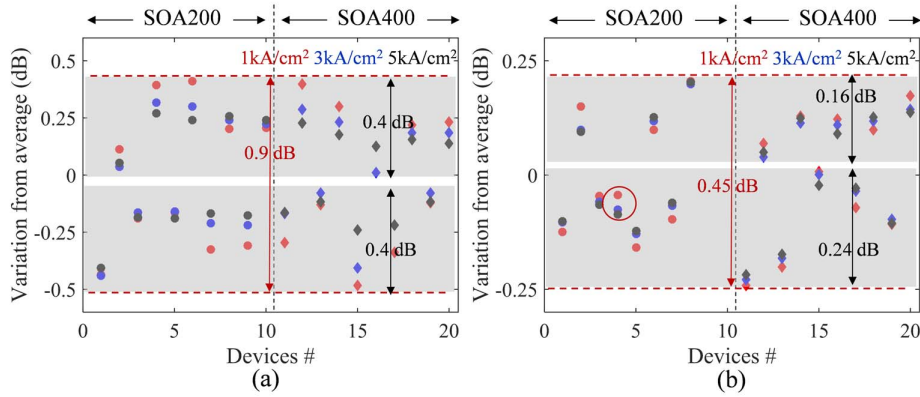
FIGURE 3.2: ISD reproducibility limit measured for 200 um and 400 um long SOA in wafer W150-1 (a), and in wafer W150-3 (b).

blue, and black, where the PDs are biased at 0 V. The reproducibility limit (or variation from average) is given by the ratio expressed in dB between the photocurrent recorded at each PD and the average photocurrent recorded in all the ISDs. Reproducibility limit is not shown for other pumping currents for graph clarity. The spreading values are, however, very similar to those represented in Figure 3.2. The odd numbered ISD in Figure 3.2 comprise the SOA and the PD on its left absorbing the SOA emission on that side. The even numbered ISD comprise the SOA and the PD on its right side.

An ISD device, similar to the one in Figure 3.1 but with 400 SOA length, is used to check what the reproducibility limit is for different SOA lengths. The 400 μm long SOAs are biased with the same current densities, 1-10 kA/cm^2 in 10 steps, as the 200 μm long ones. The PDs are biased at 0 V.

As can be seen from Figure 3.2 (a) and (b), the reproducibility limit is not dependent on the SOA length. It is, however, dependent on the wafer used. Wafer W150-3, Figure 3.2 (b), has a lower variation with respect to the average if compared to wafer W150-1, see Figure 3.2 (a). A slight improvement of the reproducibility is observed at higher current densities.

The reproducibility limit for the 20 devices present in wafer W150-1 and shown in Figure 3.2 (a) is 0.9 dB ($\pm$0.45 dB), or equivalently have a mean value of -0.005 dB and a standard deviation of 0.21 dB. The 20 ISD devices present on wafer W150-3 and shown in Figure 3.2 (b) have a reproducibility limit of 0.45 dB ($\pm$0.23 dB), or equivalently a mean value of -0.002 dB and a standard deviation of 0.12 dB. The SOA of ISD 9 and 10 in Figure 3.2 (b) is not working, and so are the ISD 9 and ISD 10, even though the PDs have typical dark current. The reproducibility limit, mean value, and the standard deviation are all calculated for the even numbered ISDs (plotted in the upper part of Figure 3.2) at bias current of 5 kA/cm^2.

In Figure 3.2 a clear pattern is present. This pattern is shown with the two gray ranges. In the upper range the even numbered ISDs are present, whereas in the lower gray range the odd numbered ones. The only exception out of 38 devices to this pattern is present for device No. 4, in Figure 3.2 (b) shown in a red circle. This pattern, present for both wafers and both SOA lengths, is a clear indication of a preferred side of transmission, namely the right side PDs absorb up to a few
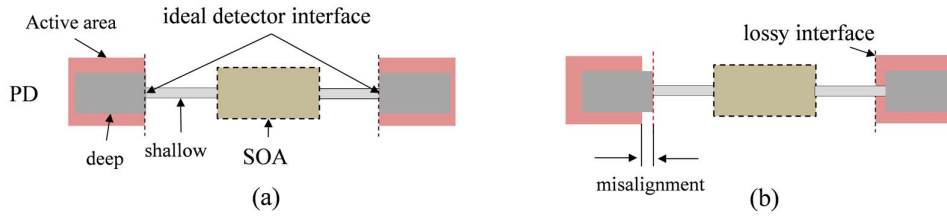
FIGURE 3.3: Interface schematic between a shallow waveguide and a PD defined in the deep cross-section. In (a) is the ideal interface and in (b) is the interface in presence of an horizontal misalignment.

percent more light than those on the left. It is unclear whether is the SOA that has a favorite emission side or a systematic error on the detectors. The design itself is symmetric with respect to the center, therefore, we can exclude it as a cause of asymmetry.

A possible cause of this asymmetry can be due to a design tolerance error that any misalignment during processing affects the performance of our test structures. In Figure 3.3 (a) is shown the interface schematic of a shallow waveguide entering a PD. The PD is defined in the deep cross-section shown in dark gray on top of a predefined active area (red), whereas the waveguide cross-section (shallow) is shown in light gray. The ideal interface, shown in black dashed line, is realized with a perfect alignment of the masks defining the shallow and the deep cross-sections with the predefined active area. However, if a horizontal misalignment is present one of the interfaces suffers higher losses than the other interface, see Figure 3.3 (b). By calculating the mode overlap between a shallow and a deep waveguide a power coupling loss of 5% is present (0.22 dB), which is in good agreement with Figure 3.2 (a). Ideally there should be only one range, centered at 0 dB, instead of 2 ranges centered at ± 0.23 dB. This mode overlap corresponds to the worst case scenario when a large misalignment is present (shallow to deep transition is far from the waveguide to PD interface). In Figure 3.2 (b) there is a less critical misalignment causing an asymmetry of only ± 0.1 dB. In the left interface of Figure 3.3 (b) the misalignment is not critical as the waveguide to PD transition happens in a wide waveguide where light simply diverges in the larger waveguide (inside the PD) rather than reflecting back. Due to the symmetry of the ISD structure, a certain horizontal misalignment is by definition critical in only one of the PD. This misalignment in Figure 3.3 (b) is critical only on the right interface. The ISD structure can be seen even as an on-wafer characterization of the horizontal mask misalignment.

This well defined pattern allows us to redefine the reproducibility limit of the source detector device. For devices in wafer W150-1 it is 0.45 dB (± 0.23 dB), or equivalently have a mean value of 0.19 dB and a standard deviation of 0.07 dB. Those in wafer W150-3 have a reproducibility limit of approximately 0.2 dB (± 0.1 dB), or equivalently a mean value of 0.1 dB and a standard deviation of 0.08. Redefining the reproducibility limit is allowed since in all the test structures comprising an ISD always only one side of the SOA emission is used. The reproducibility limit, mean value, and the standard deviation are all calculated for the
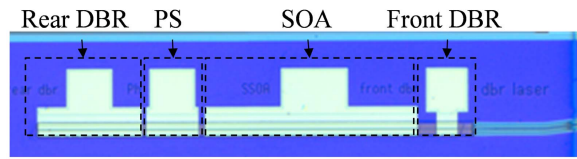
FIGURE 3.4: Microscope photograph of a test tunable DBR laser.

even numbered ISDs (plotted in the upper part of Figure 3.2) at bias current of 5 kA/cm^2.

The odd numbered ISDs have very similar parameters (reproducibility limit, mean value, and standard deviation of respectively 0.5 dB, -0.2 dB, and 0.08 dB for wafer W150-1, and 0.25 dB, -0.1 dB, and 0.06 dB for wafer W150-3). Very little dependence of these parameters on the biasing conditions of the SOAs or PDs is observed.

The integrated SOA followed by an integrated optical filter and finally by integrated detectors is used in Chapter 6.

As can be seen from the measurements at the ISD structures present in wafer W150-1 and W150-3 the reproducibility of the test modules from wafer to wafer is not yet optimal thus a constant monitoring of BBBs performance and integrated sources in every wafer is required.

To confirm the source of the reproducibility pattern found in the ISD structures a Scanning Electron Microscope (SEM) picture can be used. A more tolerant design to horizontal mask misalignment would solve the problem.

3.3 Integrated Tunable DBR Laser

To characterize some of the test structures present in the next chapters an integrated tunable source is needed. The wavelength tuning should be continuous to characterize the transmission of the given test structure.

The tunable source of choice is the DBR laser [41, 42]. The DBR laser that we propose is composed of a 250 μm long high reflecting rear grating, a 450 μm long SOA, a 30 μm long partially reflecting front grating and a 125 μm long Phase Section (PS). Test modules comprising tunable DBR lasers are implemented in PARADIGM run 2 at Oclaro [24].

A test DBR laser, with the same configuration is shown in Figure 3.4. It is provided with an external waveguide for tuning characterization. This DBR laser configuration is recommended by the foundry, and is therefore, a good starting point for the integrated tunable source.

All the test structures comprising a tunable laser presented in this thesis have the same DBR configuration. Typical tuning range of a DBR laser is 6-7 nm [41]. However, this tuning range cannot be continuous, unless some special tuning algorithm is developed which avoids the mode hops by simultaneously controlling the applied current into the rear and the phase section (or front grating) [42].

A simpler way of tuning the wavelength of the DBR laser is achieved by forward biasing the PS. By doing so only a continuous tuning between two consecutive
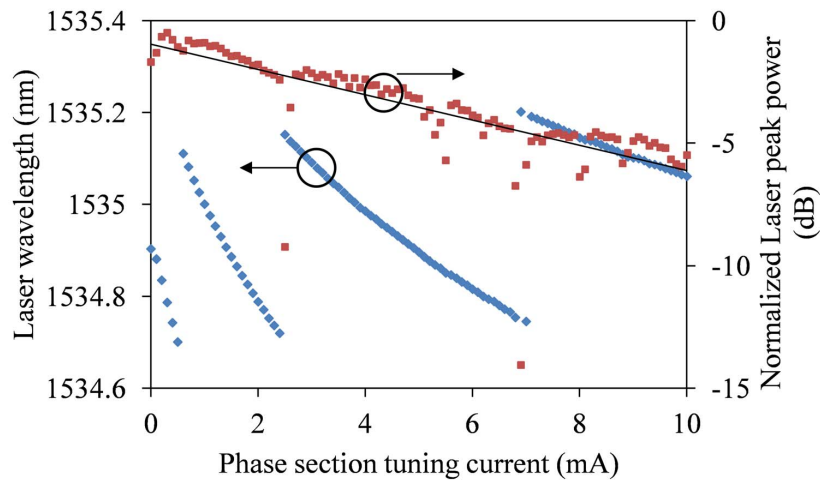
FIGURE 3.5: Tuning capability of a test DBR laser while forward biasing the phase section (dotted blue), peak power drop while laser tuning (dotted red), and the linear interpolation of the peak power drop while tuning (solid black).

longitudinal modes is obtained. In our case, given the dimensions of the DBR laser described above, the longitudinal mode spacing is 0.4 nm. As we will see in the next chapters this range of continuous wavelength tuning, if the test module is carefully designed, is sufficient to extract the parameters of interest. The tuning algorithm is much simpler (only a sweep of applied current in the PS), moreover, one electrical source less is needed.

The phase section is normally used for fine tuning of the laser such that the Side Mode Suppression Ratio (SMSR) is maximal, with SMSR defined as the power difference between the main peak and the highest secondary peak. Due to the induced low loss during the wavelength tuning operation, in the following experiments we exploit the DBR tuning capability by forward biasing only the phase section.

Figure 3.5 presents the tuning performance of the test laser of Figure 3.4 when the phase current is swept from 0 to 10 mA in steps of 100 μA. The SOA is pumped at 25 mA and no current is applied to the gratings. As can be seen by the wavelength curve (in blue) there are a few mode hop free regions suitable for the continuous tuning of the laser, needed in the integrated measurements of the following chapters. In red the laser peak power is plotted. In correspondence of the mode hops a dip in the peak power is present, moreover, the peak power decreases by 4-5 dB when the current pumped at the phase section is swept from 0 to 10 mA. The lasing wavelength and the peak power of the test laser during tuning is measured with the AQ6140 Multi-Wavelength meter. Very similar behaviour in terms of continuous tuning performance and power drop was measured in several other test lasers even on different chips.

To accurately measure the transmission of a given test structure, it is important that most of the photocurrent that the detector records is due to the peak power of the laser and not of the noise floor of the secondary peaks. A pumping current of 25 mA is used to characterize DBR lasers present in PARADIGM MPW run 1 and
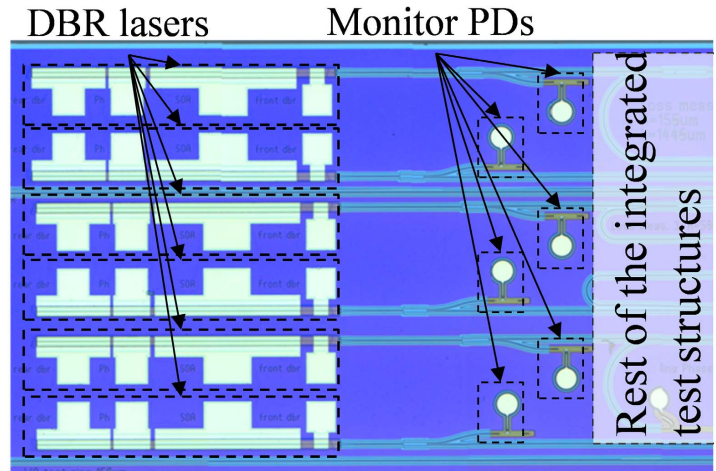
FIGURE 3.6: DBR lasers used in 6 different integrated test structures used for on-wafer characterization optical properties. The monitor photodetectors are used to monitor the peak power drop experienced by the laser while tuning.

2 as it is found to be a good compromise between a good side mode suppression ratio and a low noise floor.

The DBR laser used in test modules does not have an external waveguide to monitor the peak power drop experienced during tuning. To solve this problem we added a monitor prior to the structure of interest as shown in Figure 3.6.

A power splitter is used between the laser and the monitor. The splitting ratio is not important. What is important is the power drop during tuning of the respective DBR laser. This drop is the same experienced at the power of the other branch of the splitter that enters the test structure. The power drop experienced at the monitor photodetector is used to normalize the test structure transmission recorded at the output photodetector.

The integrated photodetector helps to continuously monitor the DBR laser activity and spot possible regions of laser instability or power fluctuations as for example in Figure 3.5 at 5.5 mA phase tuning section. The power drop at this tuning current, that might be critical for the integrated measurement, would have been detected by the integrated monitor. In presence of such a power drop the quality of the measurement is questionable.

In Figure 3.7 the IV and LI curves of the 6 lasers present in Figure 3.6 are shown. As can be seen from Figure 3.7 the DBR lasers are quite reproducible in terms of IV curves, LI curves, as well as threshold current (17±0.3 mA). The maximum photocurrent detected at the corresponding photodetectors while applying 120 mA at each DBR laser is 10.6±0.25 mA.

In the LI curves shown in Figure 3.7 (b) mode hops can be seen. These mode hops pose a threat to the on-wafer measurement. If in presence of such mode hops, detected by the integrated monitor, another wavelength range free of mode hops should be sought. Controlling the phase section as well as the rear grating of the DBR laser allows for a larger wavelength window to be explored, thus possible to find a wavelength region free of mode hops useful for the on-wafer characterization.
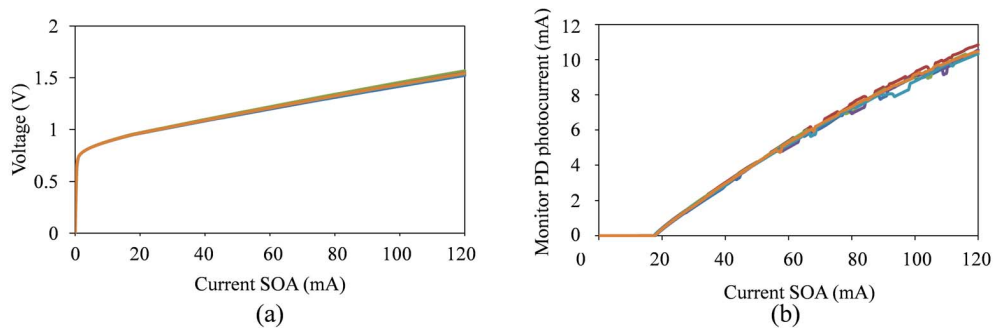
FIGURE 3.7: IV curves of the SOAs in (a), and LI curves in (b) measured on-wafer at the respective monitor photodiode of the 6 DBR lasers.
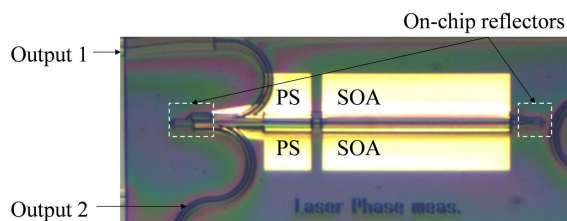
FIGURE 3.8: Microscope photograph of the coupled cavity laser.

The integrated DBR laser source followed by an integrated optical cavity and finally by an integrated photodetector is used in Chapters 4 and 5.

3.4 Integrated Coupled Cavity Laser

To characterize one of the two test modules present in Chapter 5 the coupled cavity laser described in [43] is included.

The coupled cavity laser source that we propose is composed of two 500 μm long SOAs, three on-chip reflectors based on multimode interference [45], and two phase sections long 125 μm. The test module comprising the coupled cavity laser is proposed in SMART run 9 at SMART Photonics [24].

The coupled cavity laser is shown in Figure 3.8. This coupled cavity laser configuration is used and characterized in [43] with good performance, and is therefore, a good starting point for the integrated source.

To reach threshold a 30 mA current is pumped at each SOA. The phase section is used for fine tuning of the laser such that the SMSR is maximal. A spectrum of the laser is shown in Figure 3.9. The side mode suppression ratio is larger than 30 dB [43], which as we will see in Section 5.2 is sufficient to obtain a very good performance of the overall test module.

The coupled cavity laser has two outputs which provide a similar optical output power. To increment the testability of the test module including this laser source, one of the outputs enters a monitor diode for power monitoring purposes during on-wafer measurement, and the other output is provided at the input of the test module.

FIGURE 3.9: Spectrum of the coupled cavity laser.

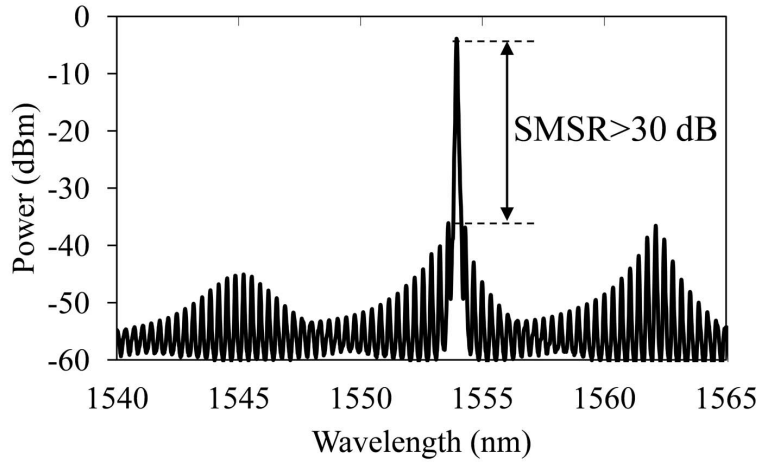To accurately measure the transmission of a given test module, it is important that most of the photo current that the detector records is due to the peak power of the laser and not of the noise floor or of the secondary peaks. A pumping current for the coupled cavity laser of 70 mA (35 mA each SOA) is found to be a good compromise between a good side mode suppression ratio and a low noise floor. As shown in [43] this coupled cavity laser is tunable over several nm, however, in the test module in Section 5.2 we operate it in a single wavelength regime.

3.5   Conclusions

In this chapter we presented the three integrated sources that we propose in the rest of this thesis together with the integrated detectors. The performance of the integrated sources and detectors was analyzed in terms of reproducibility limit for the integrated broadband source, and in terms of continuous tuning capability for the tunable laser. The coupled cavity laser source has a side mode suppression ratio of more than 30 dB. For the broad band source a worst case reproducibility limit of 0.4 dB was found which is the lowest accuracy measurement that we can claim for the test structures applying such an integrated source. The tunable laser provides a continuous tuning between two consecutive longitudinal modes of approximately 0.4 nm. This tuning range is sufficient to characterize carefully designed test modules. During tuning a peak power drop of a few dB is observed. A continuous monitoring of the SOA, the DBR laser, and of the coupled cavity laser by means of an integrated monitor is useful to mitigate possible variations of these sources during integrated measurements.

Chapter 4

Propagation Loss Characterization Methods

4.1   Introduction

The passive waveguide is one of the most used basic building blocks in photonic integrated circuits. It is used to route light on the chip. The main parameter that describes the waveguide performance is propagation loss, and it describes the power decay per unit length. To determine propagation loss many methods have been proposed [9, 46, 47].

A frequently used method to determine the loss not only of waveguides but of any two-port building block like straight and curved waveguides, MMI mode filters, tapers and isolation sections, is the Fabry-Perot measurement method [11, 12]. With this method the internal loss in the FP cavity can be determined from the Power Transmission Ratio $PTR = P_{max}/P_{min}$ with P_{max} and P_{min} the maxima and minima of the transmitted power when making a wavelength sweep. In principle, it can be very accurate, but many researchers have experienced that often the PTR is not uniform over the wavelength sweep, but shows fading and undulations, in which case it is not possible to determine a unique PTR. In [13] it is shown that first order mode excitation by misalignment of the input field can lead to measurement errors in excess of 1 dB. Their analysis is based on imaging the output light with a microscope objective on a broad area detector.

In the first part of this chapter we analyze the effect of first order mode excitation and intracavity reflections on the PTR and the accuracy of the FP method. We show that a large improvement can be obtained by detecting the transmitted light using a single mode fiber and we make recommendations for further improvement of the measurement accuracy.

Other methods for extracting propagation loss include the use of a ring cavity. In [48] the power transmission ratio, and the finesse of the ring over a wide range of wavelengths are measured. From these measured parameters the propagation loss and the coupling loss are determined. Another method is proposed in [49]. It estimates the overall loss, composed of propagation loss and coupling loss, from the ring PTR at different outputs.

In the second part of this chapter we introduce a measurement method based on an integrated test module comprising a ring resonator cavity integrated with a
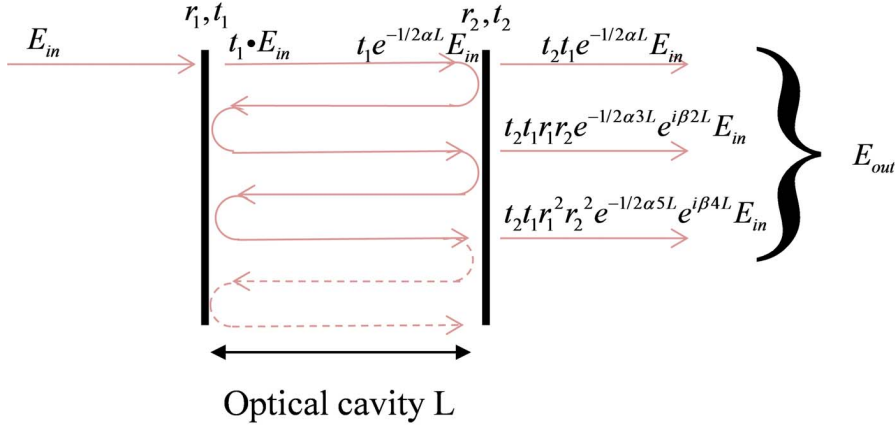
FIGURE 4.1: Schematic of the optical cavity. The electrical input field E_{in}, leads through multiple internal reflections to the electrical output field E_{out}.

tunable light source and a detector. The integrated test module is not affected by higher order modes and/or different polarized modes. It, moreover, removes the complexity associated with the cleaving and mounting of test chips.

The integrated light source and the detector are probed electrically, avoiding the critical optical coupling. The all-electrical characterization that this method allows can be performed on-wafer, allowing for automation and a radical step change in the testing costs.

4.2 Fabry-Perot Based Optical Measurement

The FP method is based on an optical cavity in which the device under test is positioned between two reflectors, usually the un-coated facets of the chip. Light coupled into this cavity travels back and forth while at each facet it gets partly reflected and partly transmitted. In Figure 4.1 a schematic of the optical cavity is shown.

The output field is given by the sum of the individual electrical fields after each roundtrip

$$E_{out} = t_1 t_2 e^{-\frac{1}{2}\alpha L} E_{in} + t_1 t_2 r_1 r_2 e^{-\frac{3}{2}\alpha L} e^{i\theta} E_{in} + t_1 t_2 r_1^2 r_2^2 e^{-\frac{5}{2}\alpha L} e^{2i\theta} E_{in} + \cdots \quad (4.1)$$

$$= t_1 t_2 e^{-\frac{1}{2}\alpha L} E_{in} \left[1 + \sum_{j=1}^{\infty} \left(r_1 r_2 e^{-\alpha L} e^{i\theta} \right)^j \right] \quad (4.2)$$

$$E_{out} = \frac{t_1 t_2 e^{-\frac{1}{2}\alpha L}}{1 - r_1 r_2 e^{-\alpha L} e^{i\theta}} E_{in} \quad (4.3)$$

with $t_{1,2}$ and $r_{1,2}$ the electric field transmission and reflection coefficient at the two interfaces, α the power decay coefficient, and $\theta = 2kL$ the roundtrip phase where
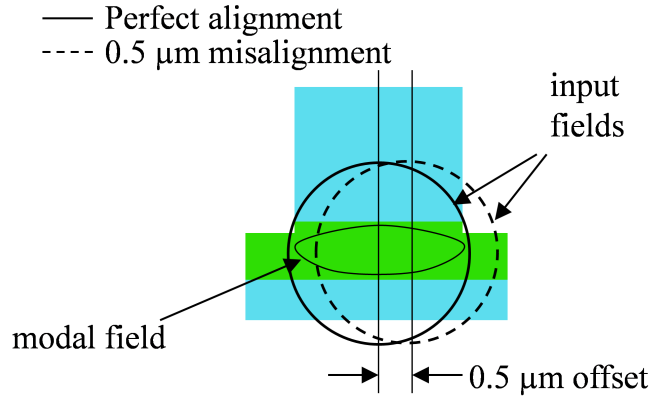
FIGURE 4.2: Schematic of the optical coupling between a microscope objective (lensed fiber) and a waveguide, best coupling (solid line) and non-best coupling (dashed line).

L is the cavity length and k the wave vector. We consider from now on $t_1 = t_2 = t$ and $r_1 = r_2 = r$.

From (4.3) the power transmission of the cavity is:

$$\frac{P_{out}}{P_{in}} = \frac{(1-R)^2 e^{-\alpha L}}{(1 - Re^{-\alpha L})^2 + 4Re^{-\alpha L}\sin^2(\theta/2)} \tag{4.4}$$

with R the power reflection coefficient $(R = r^2)$. While sweeping the wavelength the output power goes through minima and maxima dependent on the value of $\sin^2(\theta/2)$. The cavity loss, provided that we know the power reflection coefficient R and the cavity length L, is:

$$\alpha = -\frac{1}{L}\ln\left[\frac{1}{R}\frac{\sqrt{PTR}-1}{\sqrt{PTR}+1}\right] \tag{4.5}$$

with PTR the ratio between the maximum and minimum values of equation (4.4). A detailed derivation of Eq. (4.4) is given in [50]. Here we investigate how the first order mode and internal reflections affect the accuracy of the FP method and make recommendations for improvement of the measurement accuracy.

4.2.1 Effects of First Order Mode Excitation

In Figure 4.2 a schematic of the overlap between the Microscope Objective (MO) focal field and the waveguide mode during optical coupling is shown.

If the waveguide inside the FP cavity is not strictly single mode, and the input beam is misaligned with respect to the center of the waveguide higher order modes are excited. Higher order modes can also be excited by imperfections in the waveguides or at junctions on the chip. All modes are orthogonal, thus excited modes in a waveguide propagate independently. Once they exit the waveguide and are collected by the MO, however, their different phase and propagation constant will cause a PTR modulation with period proportional to the propagation constant
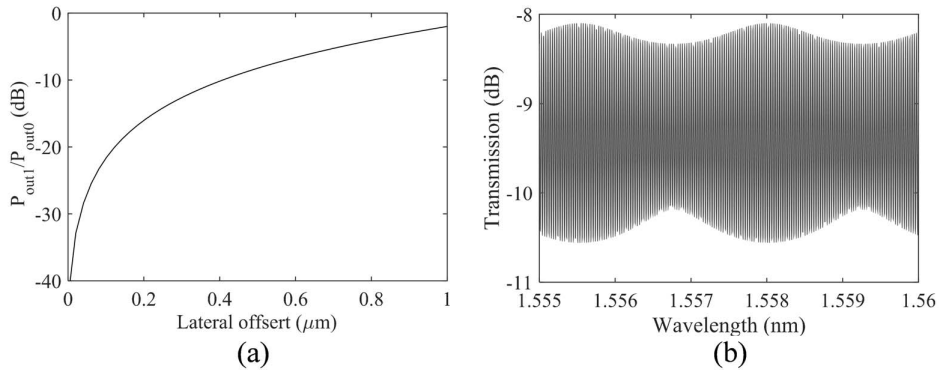
FIGURE 4.3: First order mode excitation in presence of a horizontal offset (a), and PTR when the first order mode is excited with 500 nm misalignment at the input, and the output power is collected with a MO and a large area detector (b).

difference. To analyze the effect on the measurement accuracy we simulate in Matlab an InP based 2 μm wide and 12.8 mm long shallow etched waveguide as an example. This waveguide supports 2 modes. The length is typical for 2 inch wafers processed in quarters but the results apply also to other lengths.

We distinguish two cases: output power collected with a broad area detector and with a Single Mode Fiber (SMF).

In the case when both modes are excited and the total power is collected with a MO and a broad area detector its value is given by:

$$P_{tot}(\lambda) = \eta_{M0}P_{out}^0(\lambda) + \eta_{M1}P_{out}^1(\lambda) \tag{4.6}$$

with $P_{out}^0(\lambda)$ and $P_{out}^1(\lambda)$ the power fractions in the fundamental and the first order mode respectively, and η_{Mi} the overlap integral between the MO focal field and the i_{th} waveguide mode. The ratio of the power in the two modes as a function of the lateral misalignment of the optical input is shown in Figure 4.3 (a). The interference between the two modes causes the PTR to vary between a maximum when the two modes are constructively interfering and a minimum where they are destructively interfering, as shown in Figure 4.3 (b).

Figure 4.4 shows the measurement error that is made when estimating the intracavity loss L at the destructive interference point (worst case), and at the constructive interference point (best case).

If the PTR is measured in the constructive interference point then to characterize loss with an accuracy better than 0.1 dB, the power fraction coupled to the first order mode should be lower than -5 dB (compared to power in the fundamental mode), that corresponds to a horizontal misalignment of 0.7 μm from the center of the waveguide. However, if the PTR is measured at the destructive interference point to have the same accuracy the power coupled to the first order mode should be lower than -19 dB (compared to power in the fundamental mode), which corresponds to a much stronger requirement on the alignment ($<$150 nm).

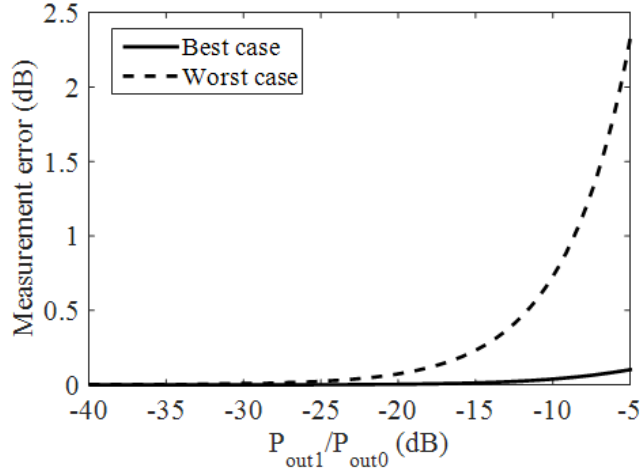These results are in good agreement with those obtained by [13, 51].

FIGURE 4.4: Measurement error occurring when loss is estimated in the constructive (solid) and destructive (dashed) interference point.

A large improvement can be achieved by collecting the transmitted light with a lensed single mode fiber which filters out the first order mode which causes the inaccuracy. We rewrite equation (4.3) in the following form

$$\frac{E_{out}}{E_{in}} = M = \frac{A}{1 - Re^{(i\theta - \alpha L)}} \tag{4.7}$$

with $A = t^2 e^{-\frac{1}{2}\alpha L}$ and $R = r^2$.

The output power in the SMF is found from the overlap integral between the sum field of all the modes excited in the waveguide. In our case only two modes.

$$P_{tot}(\lambda) = \left[\sqrt{\eta_{fo}\eta_{of}}M_0(\lambda) + \sqrt{\eta_{f1}\eta_{1f}}M_1(\lambda)\right]^2 \tag{4.8}$$

with η_{fi}, η_{if} the overlap integrals describing the input and output coupling between the fiber mode (or the focal field of a lensed single mode fiber) and the i_{th} waveguide mode, and M_0, M_1 defined for the fundamental and first order mode according to equation (4.7).

Figure 4.5 (a) shows the error in the intracavity loss estimation when measurement is performed with a SMF in the constructive interference point of the two modes and Figure 4.5 (b) when it is performed in the destructive interference point. This is done for different misalignment offsets (represented in different colors) of the output SMF from the center of the waveguide.

Collecting the output power with a SMF increases the measurement accuracy. In the worst case scenario, when the output SMF is misaligned by 500 nm the measurement error is 1.6 dB, whereas when measuring with a broad area detector and a microscope objective the error is 2.3 dB. In absence of misalignment of the output SMF the improvement in measurement accuracy is dramatic, 0.03 dB vs. 2.3 dB. If the measurement is performed in the constructive interference (best case scenario) the error when the broad area detector is used is quite small, 0.1 dB. It is however larger if compared to the case when the SMF is used (0.08 dB if the
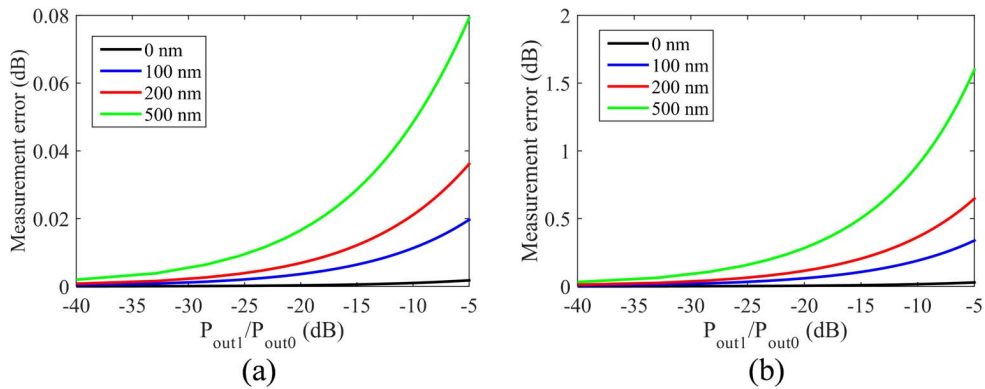
FIGURE 4.5: Measurement error occurring when loss is estimated in the constructive (a), and destructive (b) interference point as a function of the relative amount of power in the first order mode P_{out1}/P_{out0} when the output signal is collected with a Single Mode Fiber. The curves are shown for 4 different misalignments of the output fiber.

output SMF is misaligned by 500 nm, and only 0.002 dB if no misalignment of the output SMF is present).

To calculate what misalignment at the input corresponds to a given amount of power in the first order mode see Figure 4.3 (a).

The best accuracy, when using a SMF, is obtained when the output SMF is positioned at the center of the waveguide (in Figure 4.5 curves in black), because then the first order mode is filtered out. For best accuracy the fiber should be aligned by maximizing the uniformity of the PTR (no modulation present), and not for maximizing the power because in presence of first order mode the maximum will not occur in the center of the waveguide. The lowest measurement error is again achieved in the wavelength window were the constructive interference of the FP transmission happens.

The Fabry-Perot method always overestimates the real propagation loss, for a given power transmission ratio and a correct estimation of the reflection coefficient. The overestimation can be even higher than 1 dB if the PTR is measured at the destructive interference point. However, if an erroneous value for the reflection coefficient is used ($R_{sim} < R_{real}$) propagation loss can be underestimated.

4.2.2 Effects of Reflections Inside the Cavity

Also reflections inside the cavity affect the measurement accuracy of the FP method. The PTR is affected by the strength and the position of the intracavity reflection. In Figure 4.6 a schematic of a reflection point inside a FP cavity is shown. The field reflection coefficients are also shown.

To model the intracavity reflection we use the transmission matrix simulation method. For every component of the FP cavity: left and right facet, two propagating waveguides (before and after the intracavity), and the intracavity reflection

FIGURE 4.6: Schematic of a reflection point inside a Fabry-Perot cavity.
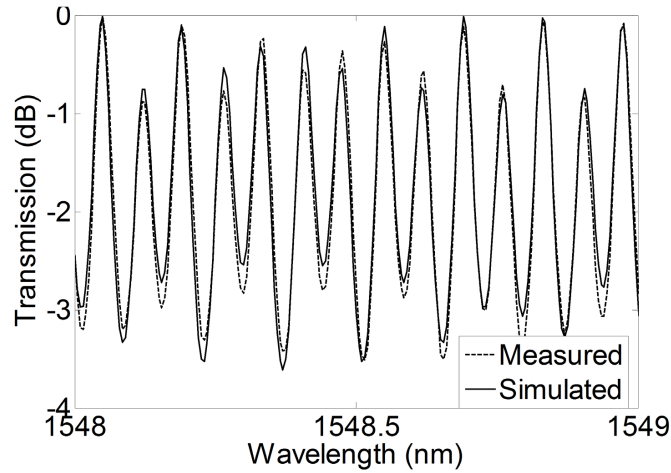
FIGURE 4.7: Simulated and measured PTR for an intracavity reflection of -20 dB.

itself, the respective transmission matrix is calculated. The final relation is

$$T = \frac{1}{t_1 t_2 t_a} \begin{pmatrix} 1 & r_1 \\ r_1 & 1 \end{pmatrix} \begin{pmatrix} e^{j\theta_1} & 0 \\ 0 & e^{-j\theta_1} \end{pmatrix} \begin{pmatrix} 1 & r_b \\ r_a & t_a t_b + r_a r_b \end{pmatrix} \begin{pmatrix} e^{j\theta_2} & 1 \\ 1 & e^{-j\theta_1} \end{pmatrix} \begin{pmatrix} 1 & -r_2 \\ -r_2 & 1 \end{pmatrix} \tag{4.9}$$

If in equation (4.9) the term $t_a t_b + r_a r_b < 1$ the intracavity reflection is lossy.
The effect of an intracavity reflection is shown in Figure 4.7. The measured curve is recorded for an MMI-coupler with some parasitic reflection at one side of the MMI section. There is a large variation of the PTR between adjacent fringes, which leads to a large inaccuracy in estimating the MMI insertion loss. Using equation (4.9) we could achieve an excellent fit between the simulated and the measured PTR if we assume a -20 dB reflection point with 3 dB loss positioned at 2.1 mm from the input facet within a main cavity of 4.6, which corresponds well with the position of the reflecting MMI interface. The left and right facets are considered lossless with the same power reflection coefficient $R = 0.33$. The value of the intracavity reflection, implemented in our model as -20 dB, was confirmed during characterization of low reflection MMIs in [52].
Once the validity of our model is shown we analyze how the position and intensity of the intracavity reflection affects the measurement error. Figure 4.8 (a) shows how the position of the intracavity reflection inside the main cavity affects the measurement accuracy. The accuracy is calculated starting from very close to the input facet, $L/50$, up to the center of the main cavity, $L/2$, with L the length of the main cavity where the measurement error is defined as the difference between the estimated and the real cavity loss.
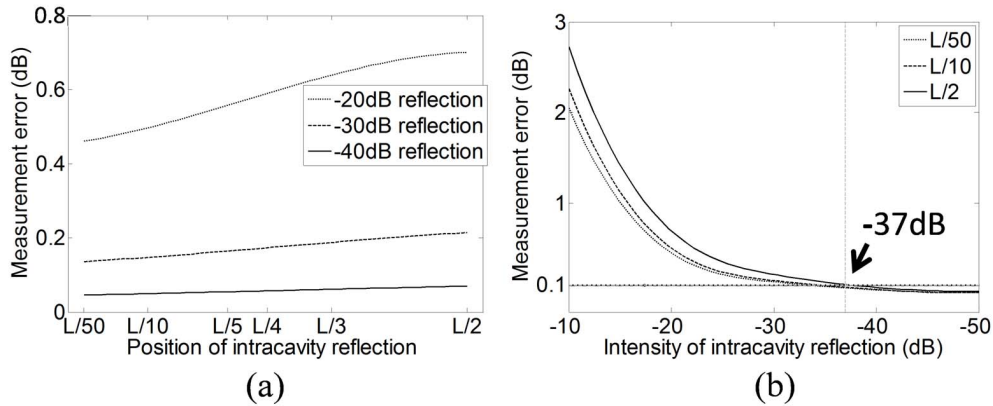
FIGURE 4.8: Measurement accuracy in measuring propagation loss vs. position of intracavity reflection (a), and vs. intensity of intracavity reflection (b).

Figure 4.8 (b) shows the dependence of the measurement accuracy on the reflection intensity. For an accuracy of 0.1 dB the intracavity reflection should be below -37 dB. The measured and simulated device is a 1x2 multimode interference coupler where the input and one of the outputs end in uncoated (reflecting) facets whereas the other output ends in a non reflecting termination such that this module, with a well known reflection value, is suitable for FP measurements. The measurement accuracy of the FP method appears to be strongly affected by intracavity reflections. The strength and position of this reflection point is of major importance. Depending on the position where the PTR is measured loss can be both overestimated and underestimated. It is important to keep intracavity reflections low and to position them as close to the reflecting facet as possible. If the measurement accuracy aims at 0.1 dB the reflection inside the cavity should be as loss as -37 dB as can be seen in Figure 4.8 (b).

4.3 Ring Resonator Based Integrated Measurement

In this section we introduce the Ring Resonator (RR) cavity, which, when integrated with a tunable light source and a detector allows for all-electrical on-wafer measurement of the propagation loss.
The ring resonator is a very suitable optical cavity for measuring propagation loss because of its high sensitivity to loss inside the cavity.

4.3.1 Analytical Model

In Figure 4.9 is shown the schematic of the ring resonator. The input and output signals couple to the RR through the bus waveguides and the coupling element. We chose the multimode interference coupler because of its tolerance to the fabrication process and its broadband operation [53, 54].
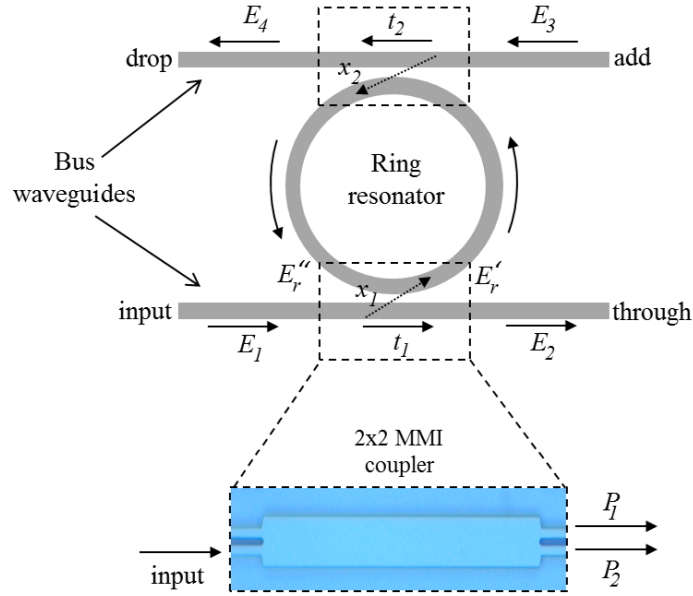
FIGURE 4.9: Schematic of the ring resonator configuration with the 2x2 MMI coupling element shown in detail in the inset.

E_r' is the part of the input electrical field E_1 that couples to the ring. E_r'' is the part of the electrical field E_r' after propagating one round trip in the ring (and eventually coupling to E_4). $t_{1,2}$ and $x_{1,2}$ are the self and cross coupling coefficients between the bus waveguide and the ring of MMI couplers 1 and 2 respectively. This ring architecture is often called the add-drop configuration.

To calculate the ring transmission the following relations as in [55, 56] are used:

$$
\begin{align}
E_1 &= 1 \tag{4.10} \\
E_2 &= I t_1 E_1 + i I x_1 E_r'' \tag{4.11} \\
E_r' &= i I x_1 E_1 + I t_1 E_r'' \tag{4.12} \\
E_r'' &= t_2 \alpha_{ring} E_r' \tag{4.13} \\
E_3 &= 0 \tag{4.14} \\
E_4 &= i x_2 \sqrt{\alpha_{ring}} E_r' \tag{4.15}
\end{align}
$$

In (4.10) the input electric field is normalized to one whereas the input field in the add port is considered zero. α_{ring} is the attenuation experienced by the field in the ring, excluding the MMI coupler, and I is the field attenuation coefficient due to the MMI coupler, called excess loss. The self and cross field coupling coefficients in a lossless coupling element satisfy the following relation: $t = \sqrt{1 - x^2}$. In the ideal case of no internal reflections inside the ring and the couplers, the output field exits only at the through and the drop port if an optical field is launched at the input port. The following transmission characteristics are obtained from the

FIGURE 4.10: Simulation of the through (solid) and drop (dashed) port transmission of a 5 mm long ring in the add-drop configuration.

equations in (4.10-4.15):

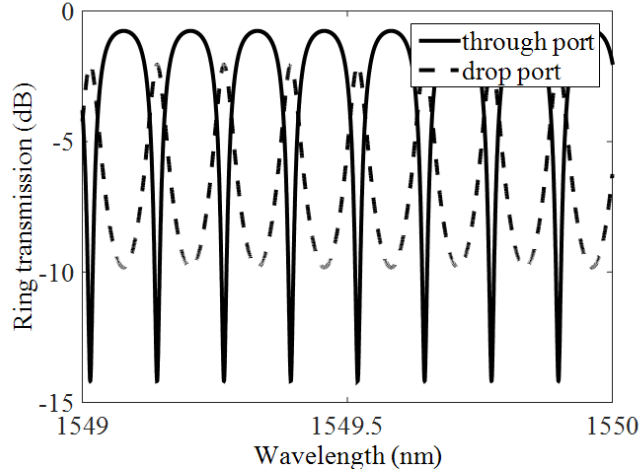$$|T_{th}|^2 = \left|\frac{E_2}{E_1}\right|^2 = I^2 \left|\frac{t_1^2 + t_2^2\tau^2 - 2t_1t_2\tau cos\theta}{1 + t_1^2t_2^2\tau^2 - 2t_1t_2\tau cos\theta}\right| \tag{4.16}$$

$$|T_d|^2 = \left|\frac{E_4}{E_1}\right|^2 = I^4 \left|\frac{\tau x_1^2 x_2^2}{1 + t_1^2t_2^2\tau^2 - 2t_1t_2\tau cos\theta}\right| \tag{4.17}$$

in which θ is the accumulated round trip phase, and τ is defined as the round trip loss $\tau = \alpha_{ring}I$. In an MMI without excess loss, $I = 1$. To test the integrated test modules, we have fabricated them in a number of multi project wafer runs. Such test-modules will be used during production for validating the quality of the processing. A small footprint of these integrated test modules is important in order to keep the testing overhead small, and, therefore, the smallest ring perimeter is needed. The perimeter is limited by the smallest radius of the curved waveguides in InP based MPW runs ($R = 150$ μm), and by the MMI coupler dimensions [53] that restricts the minimum perimeter to 1.5 mm. A small ring perimeter, however, has a large free spectral range. The continuous wavelength tuning capability of the integrated laser source, that tunes over two longitudinal modes as we saw in Section 3.3, is limited. The best trade-off, between a small footprint and a small Free Spectral Range (FSR), is a perimeter in the range 1.5-5 mm. FSR is the wavelength periodicity of the RR. The *PTR* over at least one FSR while keeping the footprint small can be measured.

We have designed, simulated, and measured several RRs in this range. In Figure 4.10 the simulated spectra of the through and drop port of a 5 mm long add-drop ring, calculated with Matlab are shown. The simulation assumes an ideal 2x2MMI coupler (no excess loss, and $P_1 = P_2$) and a waveguide propagation loss of $\alpha = 3$ dB/cm.

The power transmission ratio between the maximum $|T|^2_{max}$, and the minimum $|T|^2_{min}$ measured at the through port is obtained for respectively $cos\theta = -1$ and
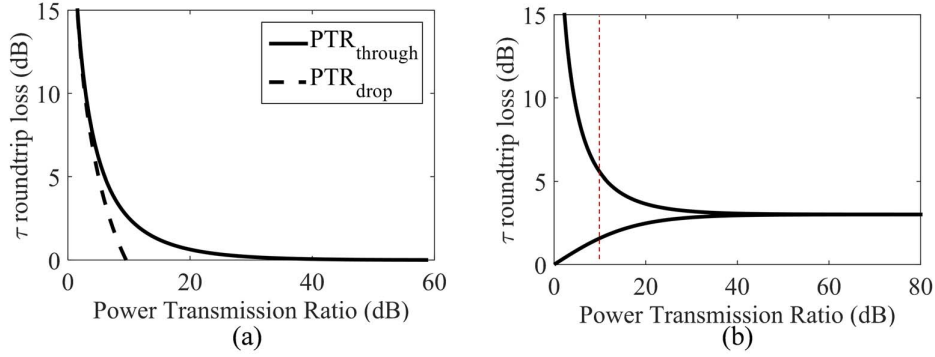
FIGURE 4.11: Round trip loss vs. power transmission ratio for add-drop (a) and for notch ring configuration (b). The dashed vertical line represents a ring perimeter design rule which guarantees a simple way to distinguish between the "low loss" and "high loss" roots of the notch ring configuration.

$\cos \theta = 1$. A similar relation can be determined for the PTR at the drop port. Finally there is a relation between the PTR at the through and drop port.

$$PTR_{th} = \frac{|T_{th}|^2_{max}}{|T_{th}|^2_{min}} = \frac{(t_1 + \tau t_2)^2 (1 - \tau t_1 t_2)^2}{(t_1 - \tau t_2)^2 (1 + \tau t_1 t_2)^2} \tag{4.18}$$

$$PTR_d = \frac{|T_d|^2_{max}}{|T_d|^2_{min}} = \frac{(1 + \tau t_1 t_2)^2}{(1 - \tau t_1 t_2)^2} \tag{4.19}$$

$$PTR_{th} \cdot PTR_d = \frac{(t_1 + \tau t_2)^2}{(t_1 - \tau t_2)^2} \tag{4.20}$$

The field self and cross coupling coefficients in the case of the add-drop ring configuration are $t_1 = t_2 = 1/\sqrt{2}$. The round trip loss from equations (4.19) and (4.20) is solved analytically (considering only the positive roots of these equations that have physical meaning), and is given by the following relations:

$$\tau = \frac{1}{t_1 t_2} \left(\frac{\sqrt{PTR_d} - 1}{\sqrt{PTR_d} + 1} \right) \tag{4.21}$$

$$\tau = \frac{t_1}{t_2} \left(\frac{\sqrt{PTR_d PTR_{th}} - 1}{\sqrt{PTR_d PTR_{th}} + 1} \right) \tag{4.22}$$

Equation (4.18) is solved numerically and shown in Figure 4.11. In case only one bus is connected to the RR a simpler configuration is obtained. This configuration is often called notch ring. Its transmitted spectrum and PTR are obtained from (4.16) and (4.18) respectively, by substituting $t_1 = 1/\sqrt{2}$ and $t_2 = 1$. This RR configuration is also known in literature as All Pass Filter since if the ring and the coupler are ideal (lossless) all the wavelengths pass through. By solving τ numerically from the PTR the graph in Figure 4.11 (b) is obtained.

In the notch ring configuration two different round trip losses correspond to each measured PTR, due to the quadratic equation (4.18). If the measured PTR,

however, is on the left side of the dotted line, see Figure 4.11 (b), it is straightforward to distinguish between the low round trip loss (high quality factor), and high round trip loss (low quality factor), and, therefore, select the correct propagation loss and discard the other one. The transmission of a high quality factor ring has a typical sharp dip and flat peak, whereas that of a low quality factor ring has a typical sine like rounded dip and peak. In semiconductor devices, the propagation loss value is expected to be in a narrow window, 2–4 dB/cm. A simple design rule is to choose the ring perimeter such that the measured PTR (that corresponds to this length and to typical propagation loss values) is on the left of the dotted line. In an add-drop configuration, on the other hand, there is always a unique solution, but as shown in the next section, the add-drop configuration has a lower measurement accuracy.

4.3.2 Accuracy Analysis

By solving equations (4.18) or (4.21) the round trip loss, defined as $\tau^2 = I^2\alpha_{ring}^2 = I^2e^{-\alpha L}$ is measured, where α is the power attenuation coefficient. The RR perimeter L is set with high accuracy by the lithographic definition and, therefore, a known of our problem, whereas the other two parameters, I and α , are unknown.

4.3.2.1 Single Notch Ring Configuration

The round trip loss is composed of two contributions: a) the waveguide propagation loss α and b) the MMI excess loss I^2. We are interested in characterizing the waveguide propagation loss but it is clear that with a single measured PTR the accurate determination of the propagation loss is closely related to our prior knowledge of the MMI excess loss. The relation

$$\Delta\alpha_I = \frac{1}{L}\frac{\delta\tau}{\delta I^2}\Delta I^2 \tag{4.23}$$

describes how the MMI excess loss error influences the determination of the propagation loss. In equation (4.23) ΔI^2 is the MMI excess loss variation, and $\Delta\alpha_I$ is the error in estimating propagation loss due to MMI excess loss variation, with the latter defined as the difference between the nominal MMI excess loss and the actual MMI excess loss. A typical power loss value of 10 % (0.45 dB) is used for I^2. Equation (4.23) is plotted in Figure 4.12 (a), for a typical propagation loss value of $\alpha = 3$ dB/cm and several ring perimeters.

For a fixed value of I^2, the higher the propagation loss experienced in the ring (longer ring perimeter and/or higher propagation loss per unit length), the smaller is the error in estimating this propagation loss. The factor $1/L$ in equation (4.23) translates $\Delta\alpha_I$ from error per round trip to error per unit length. In order to determine the propagation loss error induced by the MMI excess loss error the following procedure should be followed:

- measure the ring PTR;

- calculate the round trip loss from equation (4.18) (or through Figure 4.11 (b));
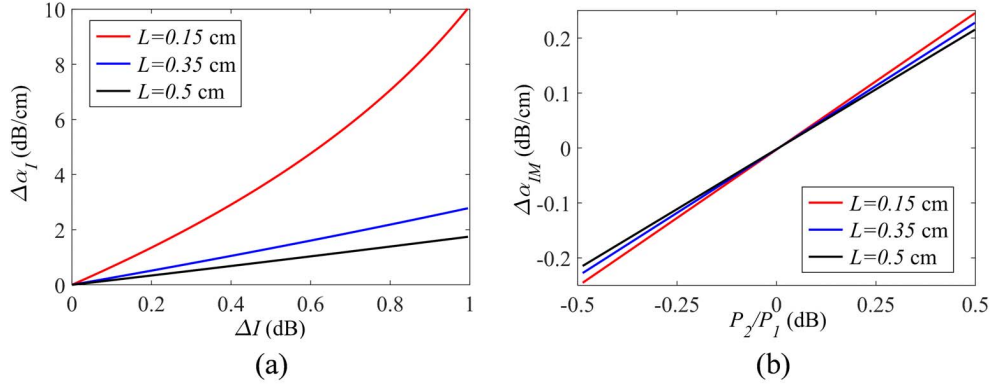
FIGURE 4.12: Error in estimating propagation loss vs. MMI excess loss error (ΔI) (left) and MMI imbalance (right) for different ring perimeters and a propagation loss $\alpha = 3$ dB/cm. The inset shows the influence on $\Delta\alpha_{IM}$ of a maximal imbalance of ± 0.5 dB with a mean at -0.25 dB.

- calculate the propagation loss: $\alpha = -\frac{1}{L}\ln\left[\frac{\tau^2}{I^2}\right]$;

- calculate $\Delta\alpha_I$ through equation (4.23);

Also the imbalance of the MMI coupler plays a role in the measurement accuracy. An imbalanced 2x2MMI with a cross coupling coefficient $x^2 > 0.5$ will lead to an overestimation of the propagation loss measured with the ring resonator module, whereas $x^2 < 0.5$ leads to an underestimation of the propagation loss. The imbalance is defined as: $IM^2 = 10\log_{10}(P_2/P_1)$ with P_2 and P_1 the power exiting from the two MMI outputs as shown in the inset of Figure 4.9. The maximal imbalance of the 2x2MMI in our technology is $IM^2 = \pm 0.5$ dB. To quantify the influence of the 2x2MMI imbalance on the propagation loss calculation the following relation is used:

$$\Delta\alpha_{IM} = \frac{1}{L}(e^{-\alpha_t L} - e^{-\alpha_{t+\Delta t}L}) \qquad (4.24)$$

where α_t and $\alpha_{t+\Delta t}$ are the propagation losses estimated, respectively, in the case of ideal and imbalanced 2x2MMI. The factor $1/L$ in equation (4.24) translates $\Delta\alpha_{IM}$ from error per round trip to error per unit length.

Excess loss and imbalance are independent parameters of the MMI, however, during processing there is typically one dominant cause for errors such as MMI width variation and/or overetch (underetch) which affects both MMI properties in a similar way. Therefore, we consider measurement uncertainties due to MMI excess loss and imbalance dependent on each other. The overall propagation loss measurement accuracy attainable with the notch ring configuration is [17]

$$\Delta\alpha = \Delta\alpha_I + \Delta\alpha_{IM} \qquad (4.25)$$

For a typical MMI excess loss variation of $\Delta I^2 = 0.45$ dB, maximal MMI imbalance of $IM^2 = 0.5$ dB, propagation loss $\alpha = 3$ dB/cm, and ring perimeter $L = 5$ mm the MMI excess loss and the MMI imbalance induced error are respectively 0.8

dB/cm and 0.2 dB/cm. Therefore, the excess loss induced error dominates the overall error.

4.3.2.2 Add-drop Ring Configuration

In the case of an add-drop ring configuration there is the contribution of two 2x2MMI couplers in each round trip. Therefore, the contribution of the ΔI and the IM in the round trip loss, experienced by the field and estimated by the PTR at the through and at the drop port, is twice as large as in the notch ring configuration. The propagation loss measurement uncertainty attainable with the add-drop ring is

$$\Delta\alpha = 2\Delta\alpha_I + 2\Delta\alpha_{IM} \tag{4.26}$$

From a measurement accuracy point of view we can state that the notch ring is twice as accurate as the add-drop ring for a given footprint. The add-drop ring in turn, has a unique PTR for any given round trip loss.

4.3.2.3 Double Notch Ring Configuration

The last configuration that we consider is the double notch ring with different perimeters and the same coupling element. With this configuration we can discriminate between propagation loss and MMI excess loss by assuming that the MMI couplers have the same properties (excess loss and imbalance).

If the RRs are in the same chip area, as those in Figure 4.13, only the difference in excess loss and imbalance of the corresponding MMIs plays a role in the measurement accuracy. If the MMIs are closely spaced in the PIC their excess loss and imbalance vary with less than 4 %. This value was measured through a dedicated test structure composed of an odd number of cascaded 2x2MMI couplers. The total imbalance of a cascaded number of 2x2MMIs scales in first approximation linearly if compared to that of a single 2x2MMI, thus making it possible to be measured. Cascading an even numbers of 2x2MMI, conversely, would not allow to measure the imbalance between the two outputs as the total optical power would simply be switched completely at the cross output (due to the $\pi/2$ of phase delay added by each 2x2MMI). The final accuracy is calculated by using (4.25). The singular $\Delta\alpha_I$ and $\Delta\alpha_{IM}$ uncertainty contributions are still calculated using equations (4.23) and (4.24) with the value of 4 % measured for MMIs closely spaced in PIC.

Maximal MMI excess loss variation is $\Delta I^2 = 0.45$ dB, and maximal MMI imbalance is $IM^2 = 0.5$ dB, whereas if the MMIs are closely spaced in the PIC's area these variations go down to less than 0.04. If a single notch ring is used then the value 0.1 (0.5 dB) should be used for ΔI^2 and IM^2.

4.3.3 Optical Experiments

The test modules presented in this section are fabricated in a MPW run on the COBRA platform. We verify the validity of the analytical models derived in Section 4.3.1, and the measurement accuracy as analyzed in Section 4.3.2 for the best ring configurations in terms of measurement accuracy, namely the notch ring, and
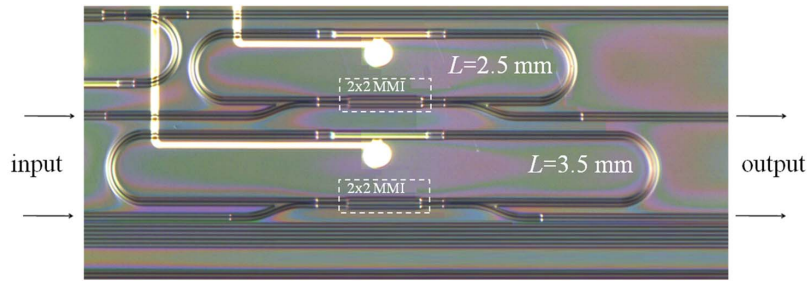
FIGURE 4.13: Microscope photo of notch rings.
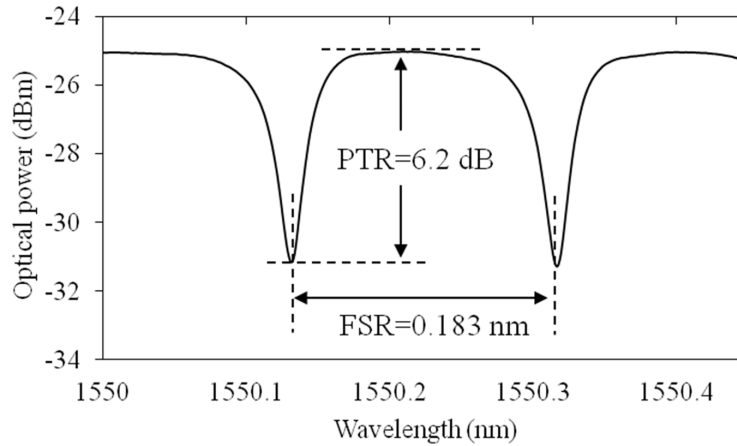
FIGURE 4.14: Transmission measurement, Power Transmission Ratio, and Free Spectral Range of a 3.5 mm long racetrack in the notch ring.

the double notch ring configurations, using test structures without integrated light source and detector. All the ring configurations that we measure in this section and the next one have the shape of a racetrack, as shown in Figure 4.13, which means that they are composed of 2 semi-circular arcs of π radians connected by straight waveguides. The analytical model and the accuracy analysis presented in the previous sections are not dependent on the ring shape but on the ring perimeter, thus the previous analysis is still valid for a racetrack shape ring. Moreover, the use of the racetrack allows the decoupling of the ring radius from the ring perimeter. All the straight and curved waveguides are designed to be 1.5 μm wide and deeply etched to allow small bending radii, and, therefore, a small footprint. The 1.5 μm wide waveguides are single mode, thus possible higher order modes, excited in junctions or at imperfections, should not be guided.

4.3.3.1   Notch Ring Configuration

Figure 4.14 shows the measured spectrum of the 3.5 mm long ring shown in Figure 4.13. To suppress the back reflections from the facets the input and output waveguides were designed at a 7° angle. No evidence of facet reflections in the ring transmission was found.

The passive ring configurations have been measured using an Agilent HP 8168A tuneable source connected to a polarization control stage and a lensed single-mode polarization-maintaining fibre. Transverse electric polarized light was coupled to the input bus waveguide of the ring cavity. Light was coupled out of the bus waveguide through a lensed fibre, and finally fed to a power meter. A wavelength sweep was performed with a step of 1 pm and the recorded power is shown in Figure 4.14.

To determine $\Delta\alpha_I$ we repeat the procedure with (in brackets) the values that apply to the single notch ring configuration under examination:

- measure ring PTR (6.2 dB);

- determine the round trip loss through (4.18) (or Figure 4.11 (b)): $\tau^2 = 0.785 = 1.05$ dB;

- calculate the propagation loss: $\alpha = 0.39 \ cm^{-1} = 1.7$ dB/cm;

- calculate the propagation loss error (4.23) $\Delta\alpha_I = 0.25 = 1.25$ dB/cm;

Equation (4.23) gives the differential error when approximating a function with its first derivative calculated around the point $\alpha = 1.7$ dB/cm (0.39 cm^{-1}) for an MMI excess loss error of $\Delta I^2 = 0.1$.

By following the same procedure for the MMI imbalance described in the previous section the propagation loss error for the nominal MMI imbalance is $\Delta\alpha_{IM} = 0.032$ (0.13 dB/cm). The final measurement accuracy using equation (4.25) is $\Delta\alpha = 0.282$ (1.38 dB/cm), and the measured propagation loss is $\alpha = 1.7 \pm 0.69$ dB/cm.

4.3.3.2 Double Notch Ring Configuration

To isolate the inaccuracy due to the 2x2MMI coupler we use two rings with the same 2x2MMI coupler but different overall lengths. The first ring is the one previously analyzed ($L_1 = 0.35$ cm), whereas the second has a length $L_2 = 0.25$ cm. The racetrack configuration allows a difference in length to be implemented in the straight waveguide section and, therefore, gives us a measurement of the propagation loss in the straight waveguide, see Figure 4.13. The transmission of the two rings is shown in Figure 4.15.

The power transmission ratios are $PTR_1 = 6.2$ dB and $PTR_2 = 4.7$ dB respectively, which by solving (4.18) for the notch ring or by using Figure 4.11 (b), corresponds to $\tau_1^2 = 0.785$ (1.05 dB) and $\tau_2^2 = 0.83$ (0.81 dB) round trip loss. Knowing the ring length difference $\Delta L = 0.1$ cm it is straight forward to calculate the propagation loss $\alpha = \frac{1}{\Delta L}\ln(\frac{\tau_1^2}{\tau_2^2}) = 0.56$ cm^{-1} (2.4 dB/cm), which corresponds to an MMI excess loss of $I^2 = \tau_{1,2}^2/\alpha_{ring1,2}^2 = 0.955$ (0.2 dB). Taking into account the excess loss variations and imbalance of adjacent MMIs, $\Delta I^2 = 0.04$ and $IM^2 = 0.04$ as described in Section 4.3.2.3, the double sided accuracy interval becomes $\Delta\alpha = 0.11$ (0.5 dB/cm). The measured propagation loss is $\alpha = 2.4 \pm 0.25$ dB/cm.

To verify the propagation loss measurement result the Fabry-Perot method [48, 49] was used in a straight deeply etched reference waveguide. Propagation loss of
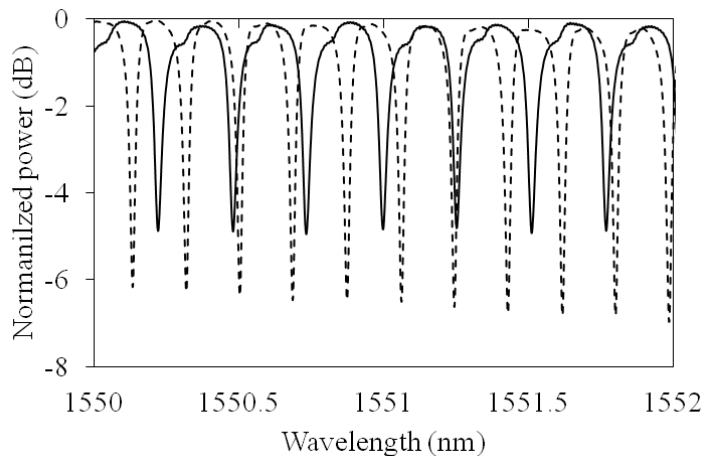
FIGURE 4.15: Measured transmission spectra of a 2.5 mm long ring (solid) and a 3.5 mm long ring (dashed).

$\alpha = 2.35 \pm 0.22$ dB/cm was measured for a 3.2 mm long cavity and a simulated facet reflectivity for a deep etched waveguide of $R = 0.31 \pm 0.005$. The variation of the reflection coefficient accounts for typical process variations that affect the waveguide width and/or etch depth. This propagation loss range is in very good agreement with the result of the double notch configuration.

4.3.3.3   Effects of Multiple Modes

Other effects that might reduce the measurement accuracy are the presence of higher order TE modes or TM polarized mode. These modes can be excited from a misalignment at the input, a non perfect junction between BBB, a mode conversion in curved waveguides or from intracavity reflections.

Higher Order TE Polarized Modes

In the transmission of the 2.5 mm long ring, shown in Figure 4.15, a slight modulation of the fringes can be seen. This modulation is to be attributed to higher order TE modes propagating in the circuit. To verify our claim a long wavelength sweep measurement was performed. This measurement is compared to the simulation when considering higher order modes propagating in the circuit that are excited by a deliberate misalignment of the input coupling to the waveguide, see Figure 4.16.

The measured and the simulated transmission match quite well in terms of the beating period (32 nm) which confirms that the observed modulation is caused by a higher order mode, in this case the first order mode.

The simulation was performed using the Agilent's Advanced Design Systems (ADS) simulation tool which considers the first 3 modes.

TM Polarized Mode

In case the TM polarized mode is present in the circuit it will cause a fringe modulation similar to the one caused by the higher order TE mode. For rings
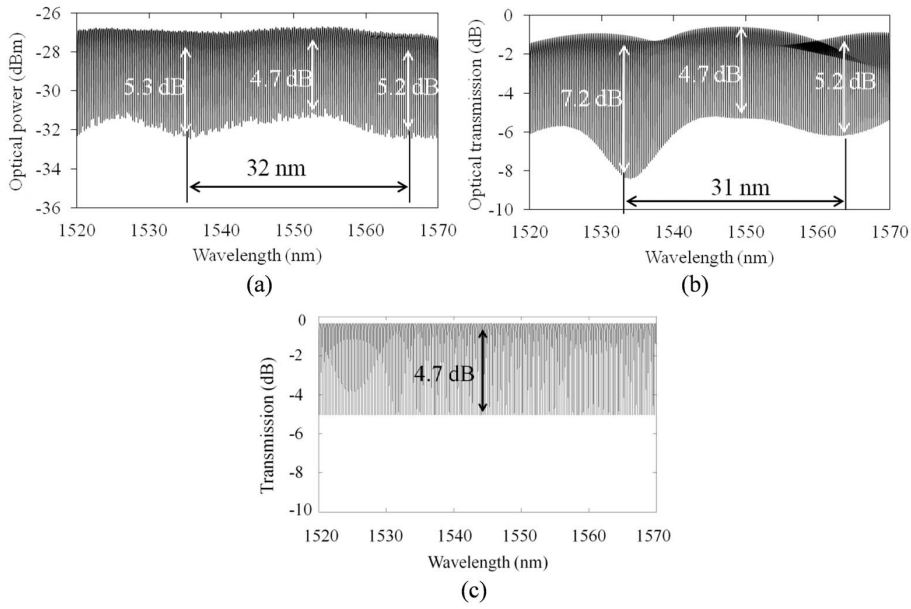
FIGURE 4.16: Measured transmission of a 2.5 mm long ring is shown in (a). A simulated transmission that considers the propagation of the fundamental and higher order modes is shown in (b), and with only the fundamental TE mode in (c). The MMI excess loss was included in the simulation.

with round trip loss less than 3 dB the PTR is proportional to the propagation loss, see Figure 4.11 (b), therefore, the smallest PTR corresponds to the lowest loss mode propagating in the optical circuit. To characterize the propagation loss for the fundamental TE mode, in case both polarizations are excited, the smallest PTR should be considered, since in our technology the waveguide design is optimized to minimize propagation loss for TE polarized mode.

Moreover, the maximum value of equation (4.18) is obtained for $\cos\theta = -1$ and corresponds to

$$|T_{th}|^2_{max} = \frac{(t_1 + \tau)^2}{(1 + t_1\tau)^2} \tag{4.27}$$

Equation (4.27), which describes the top envelope of the ring transmission, is maximized by maximizing τ, thus by minimizing the propagation loss α ($\tau^2 = I^2 e^{-\alpha L}$). From equation (4.27) the propagation loss of the fundamental TE mode is best estimated at the highest transmission point.

These two simple rules allow us to quickly select the optimal characterization wavelength window that allows the highest accuracy in measuring propagation loss of the TE polarized mode (the influence of TM mode is the smallest possible). The problem of higher order modes and/or excitation of the TM polarization is solved in the on-wafer test module that includes an integrated single mode laser source. The measurement uncertainty due to reflection coefficient variation is also solved by use of the integrated measurement.
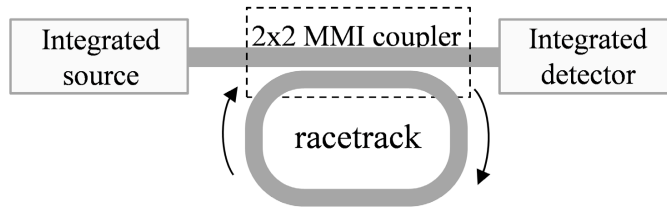
FIGURE 4.17: Schematic of the integrated ring-based test module for measuring propagation loss.

Intracavity Reflections

The mode conversion that might happen at the junction between different BBBs is negligible if the design rules suggested by the foundries are followed. Polarization conversion in deep etched curved waveguides is also negligible [57].
The last uncertainty source is the intracavity reflection. The use of integrated measurements unfortunately cannot solve the issues related to the presence of intracavity reflections. A careful choice of the BBBs used and of the test module design, however can reduce these effects to a minimum. A simple example is the choice of a 2x2MMI even when a simple splitter is needed. The simplest splitter is a 1x2MMI. The 2x2MMI coupler has lower reflection coefficients if compared to the 1x2MMI [52]. The 2x2MMI coupler present in the ring test module, as can be seen from the optical measurements does not include any noticeable parasitic effect that would modify the ring transmission curve. The only parameter so far is the first order mode coupled at the input during optical measurements.

4.3.4   Electrical Experiments

The last test modules presented in this section and shown in the schematic of Figure 4.17 concern the notch ring coupled through a 2x2MMI to an integrated tunable laser source and an integrated photo detector. They are designed according to the generic integration concept, using standardized building blocks, and fabricated in a MPW run at Oclaro.
The measured notch rings have perimeters of 1.44 mm (the smallest possible when complying with the 150 μm minimum radius of curved waveguides, and an MMI length of 150 μm) and 3.44 mm (2 mm longer than ring 1), as shown in Figure 4.18 (a).
The integrated source for these test modules is a tunable Distributed Bragg Reflector laser [41, 42], as described in Chapter 3. The output signal is measured by an integrated fully absorbing PD. To get an interference pattern at the ring resonator output the wavelength of the source should be tunable. The DBR laser configuration used is the standard one offered by the foundry. The measured transmission of the 1.44 mm and 3.44 mm long rings is shown in Figure 4.19 (a). The output power, measured at the integrated detector, is normalized on the power measured at the integrated monitor. The monitor is used to track the laser output power which drops by a few dB during tuning.
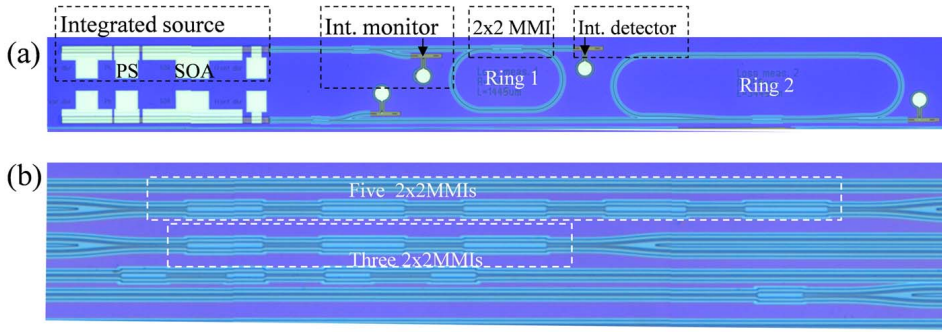
FIGURE 4.18: (a) Fully integrated notch ring resonator structure for propagation loss measurement, and (b) the dedicated test module for measuring variations in excess and imbalance loss for closely spaced 2x2MMIs.
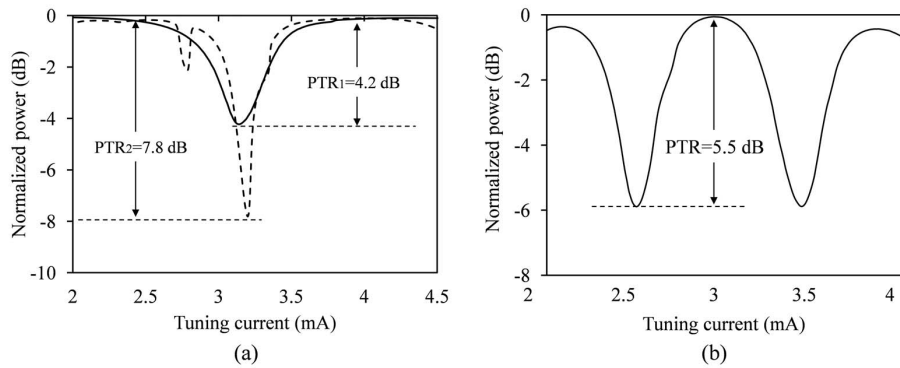
FIGURE 4.19: Measured transmission of a 1.44 mm long (solid) and a 3.44 mm long (dashed) ring resonator (a), and of a 5.2 mm long ring resonator in an MPW run with high loss (b). The current applied at the phase section of the DBR lasers is used to fine tune its wavelength. The small dip in ring 2 transmission (dashed line) is due to a mode hop of the laser.

The semiconductor optical amplifier section of the DBR laser is biased above threshold by pumping it with 25 mA ($I_{th} = 18mA$). Higher pumping currents were avoided to lower the noise floor. Stable single-mode operating regime for the integrated laser requires a stable operating temperature that is achieved by using a temperature controller during on-wafer measurement. During measurement the temperature was set at 18°C. The lasing wavelength was tuned by varying the current applied at the laser Phase Section (PS), thus only a limited continuous tuning between two consecutive longitudinal Fabry-Perot modes is obtained. The DBR mirrors were not tuned to avoid mode hops and to simplify the continuous wavelength tuning procedure (no second control signal applied to the DBR mirror). With a careful design of the RR perimeter, the small tuning window (0.45 nm) is sufficient to obtain a wavelength sweep over one FSR for ring 1. The power at the output is measured by an integrated full absorbing photo detector.

The measured power transmission ratios are $PTR_1 = 4.2$ dB and $PTR_2 = 7.8$ dB, which, by solving equation (4.18) for the notch ring or by using Figure 4.11

	Single notch	Double notch	Add-drop
Measured accuracy (dB/cm)	±0.55	± 0.22	±1.3
Footprint RR (mm^2)	1.0	1.5	1.0

FIGURE 4.20: Comparative table of the principal ring configurations. The three configurations use the same 2x2MMI coupler.

(b), correspond to $\tau_1^2 = 0.846$ (0.73 dB) and $\tau_2^2 = 0.743$ (1.3 dB) round trip loss respectively. Considering the ring length difference $\Delta L = 0.2$ cm it is straight forward to calculate the propagation loss $\alpha = \frac{1}{\Delta L} \ln(\frac{\tau_1^2}{\tau_2^2}) = 0.65 cm^{-1}$ (2.82 dB/cm). Which corresponds to an MMI excess loss of $I^2 = \tau_{1,2}^2/\alpha_{ring1,2} = 0.929$ (0.32 dB). In this calculation we assumed that the propagation loss experienced in the straight and curved waveguides is the same.

A dedicated test structure for measuring excess loss and imbalance of 2x2MMIs was included in the chip, see Figure 4.18 (b). The excess loss of the 2x2MMI, measured on these test structures was found to be in the range 0.3-0.5 dB over the C-band which is in good agreement with the results obtained by the RRs. For the imbalance the measurement showed 0.1-0.2 dB. Using these values for the excess loss and imbalance of adjacent MMIs, $\Delta I^2 = 0.04$ and $IM^2 = 0.04$, the accuracy becomes: $\Delta \alpha = 0.11$ (0.5 dB/cm). So the measured propagation loss is $\alpha = 2.82 \pm 0.25$ dB/cm.

The integrated monitor and the integrated output detector are used for a relative measurement of the power of the integrated tunable laser, therefore, no absolute calibration of the splitting MMI or of the monitor detector is needed.

A similar test module was present in a wafer that due to some processing problems suffered high losses. Nonetheless the integrated RR with a perimeter of 5.2 mm (4 times larger than the smallest ring perimeter possible), under the same working conditions as the one previously described, showed a PTR of 5.5 dB which corresponds to 1 dB/cm or 15.5 dB/cm propagation loss depending whether we are on the lower or higher side of the critical coupling. From the low quality factor of the ring transmission, see Figure 4.19 (b), the 1 dB/cm propagation loss was discarded. A very similar value of propagation loss was measured in an alternative test structure present on the same test cell. This example shows the versatility of the integrated ring resonator test module in measuring propagation loss over a large range.

In Figure 4.20 a comparison of the RR configurations in terms of footprint and measurement accuracy for a typical ring perimeter of 0.25 cm and loss $\alpha = 3$ dB/cm is shown. The best configuration in terms of accuracy is the double notch

ring, whereas in terms of footprint the single notch and the add-drop are better. A considerable part of the footprint is due to the integrated DBR laser, see Figure 4.18 (a). The gain in terms of measurement accuracy obtained with the double notch ring is several times larger than with the other methods with only a small price in footprint. Therefore, this is our method of choice for on-wafer propagation loss determination.

In the single notch configuration two propagation loss values correspond to every measured PTR. Data interpretation is needed to choose the correct propagation loss. In the double notch configuration two values of the propagation loss correspond to each of the rings but only two of the solutions are consistent. The add-drop configuration has only one solution for any measured PTR.

4.4   Conclusions

In this chapter we first analyzed in detail the well-known Fabry-Perot measurement method in terms of measurement accuracy. We found that higher order modes exited due to a non-optimal input coupling or at imperfections in the waveguides or junctions on the chip can lead to a large measurement error if measured at a wrong wavelength window. A large improvement in measurement accuracy is obtained if the power at the output is collected with a (lensed) single mode fiber which filters out the first order mode. The presence of intracavity reflections affect the FP method too. We analyzed the dependence of the measurement accuracy on the position and strength of the intracavity reflections.

Further, we demonstrated for the first time on-wafer propagation loss measurements using an integrated tunable light source, a photo detector, and a ring cavity. The test module was fabricated in an MPW run in an InP-based foundry process. This measurement method uses electrical probing rather than optical coupling with lensed fibers and is, therefore, faster and more reproducible. It can be carried out with a current and a voltage source avoiding expensive equipment such as optical spectrum analyzers, tunable lasers and power meters and, moreover, it can be done earlier in the PIC processing, i.e. before cleaving the wafer. Experimental data show that this method is consistent with other classical methods as, for example, the Fabry-Perot measurement method. It can be applied to measure propagation loss from 1-2 dB/cm up to 15 dB/cm or higher. An accuracy analysis was carried out for different ring configurations. The analysis identified the MMI excess loss error and MMI imbalance as the main factors degrading propagation loss measurement accuracy. The accuracy is dependent on the ring configuration and the propagation loss. The best ring configuration in terms of accuracy is the double notch ring with $\Delta\alpha = \pm0.25$ dB/cm. Its results compare well with data measured with the Fabry-Perot method. The Fabry-Perot method depends on prior knowledge of the facet reflectivity, and it requires cleaved facets and optical alignment. These draw-backs are avoided with our integrated measurement approach.

Chapter 5

Phase Modulation Efficiency Characterization Methods

5.1 Introduction

The easiest way to encode data to a stream of light is by switching the laser between its on and off state. This solution, called direct intensity modulation, however, is not applicable in long range communication systems due to the large chirp (time dependence of the frequency components of an optical pulse) that is due to the change in refractive index of the laser when the carrier density changes [58]. To solve the problem of chirping external modulators can be used.

In the generic foundry approach [22, 23] the phase modulator is a basic building block responsible for manipulation of the phase of the light, by using an electrical control signal (voltage or current).

The phase modulator is key component in the advanced modulation formats [59–61] that are used in high bitrate communication channels. By integrating phase modulators in a Mach-Zehnder Interferometer (MZI) the phase modulation, provided by the PM, can be converted into amplitude modulation. The MZI is composed of a power splitter at the input, 2 symmetric arms containing a phase modulator, and a power combiner at the output. The phase modulation, obtained in the PM BBB is converted to amplitude modulation by means of constructive and destructive interference at the power coupler of the MZI.

The most important parameters that characterize a phase modulator are the phase modulation efficiency V_π (I_π), defined as the voltage (current) required to obtain 180 degree phase shift. Often $V_\pi L$ is used instead for taking into consideration the footprint of the modulator as well. Other parameters are the insertion loss of the phase modulator, defined as the power attenuation due to the modulator, the absorption introduced by the phase modulator while operating, the polarization response of the phase modulator, the bandwidth of the phase modulator etc.

Up to now on-wafer characterization reported in the literature is restricted to discrete Mach-Zehnders with external sources coupled through a fiber and (sometimes) with integrated detectors [62, 63]. Thus characterization is done in the mixed electro-optical domain, and accurate optical alignment is required to get accurate results.

In this chapter we focus on fully-integrated test modules, suitable for electrical on-wafer characterization of the phase modulator efficiency. We demonstrate two novel fully-integrated test modules with a small footprint, that are suitable for electrical on-wafer characterization of the phase modulation efficiency. They can be used for wafer validation by guaranteeing phase modulator performance for all application specific circuits on wafer.

The first test module integrates the classical MZ interferometer with a laser source and two detectors. The second test module uses a compact ring resonator integrated with a laser source and a detector. The phase modulator is included inside the ring cavity.

5.1.1 Electro-Optical Effects in InP

Indium phosphide is a good electro-optical material. It possesses several electro-optical effects that can be used in designing PICs. In this section we describe them briefly. They can be divided in two main groups: those where the refractive index change is induced by an externally applied electric field and those induced by carrier injection.

Electric Field Induced Electro-Optical Effects

When an external electric field is applied to a semiconductor material such as InP its refractive index changes proportionally to this field.

- If the change in refractive index is linearly proportional to the applied electric field it is called the linear (Pockels) electro-optic effect [64–66].

- If the change in refractive index is quadratically proportional to the applied electric field it is called the quadratic (Kerr) effect [66, 67].

The crystalline structure of the material determines which electro-optical effect is present. In InP both the linear and the quadratic electro-optical effects are present. The Pockels effect is dependent on the crystallographic orientation of the phase modulator. The obtained refractive index change can be positive or negative depending on the orientation of the phase modulator [66]. The Pockels effect is significantly larger than the Kerr effect but affects only the TE polarization. The Kerr effect is polarization independent [66].

- The Franz-Keldysh effect involves the bandgap of the semiconductors. Here the applied electric field changes the refractive index by modifying the bandgap [66, 68, 69]. The Franz-Keldysh effect is polarization independent.

- The Pockels, the Kerr, and the Franz-Keldysh effects are present in bulk materials. In a quantum-well material the Quantum-Confined Stark Effect (QCSE) is responsible for the electro-absorption of the material [66, 71]. The band gap of the semiconductor changes quadratically with the electric field. The QCSE is very efficient and it requires, therefore, a small footprint on the chip [72]. However, it introduces a high absorption. Where a low applied voltage is required MQW modulators are used that combine the QCSE and

the linear electro-optical effect [72, 73]. Both the Pockels and the QCSE effect are polarization dependent.

The speed of the field-induced effects is very high, in the order of ps. The bandwidth of the modulators is restricted by the resistance and the capacitance of the electrodes. In traveling wave configurations the bandwidths can be higher than 40 GHz [66].

Carrier Induced Electro-Optical Effects

The above mentioned effects are due to the change of refractive index induced by an externally applied electric field. If carriers are injected in an electro-optically active material several other effects take place

- Free carrier absorption (plasma effect) is induced by carrier injection [66, 74]. The corresponding refractive index change is negative ($\Delta n < 0$) for photon energies below the band gap.

- Bandfilling is another electro-optical effect induced by carrier injection [66, 75]. The refractive index change is also negative for photon energies below the band gap ($\Delta n < 0$).

- The last carrier induced effect is the band gap shrinkage [66, 76]. In this case the refractive index change is positive ($\Delta n > 0$) for photon energies below the band gap.

The Kramers-Kronig relations describe a universal relationship between the real and imaginary parts of the refractive index. They can be used to determine the real part of the refractive index given the absorption coefficient of the material for a certain wavelength band or vice versa [66, 70].

The speed of the carrier induced effects is restricted to a few GHz by the carrier recombination time which is in the order of ns. However, local heating by the injected current will contribute significantly to the induced phase change and will strongly reduce the switching speed, because thermal effects occur on a ms time scale.

5.1.2 Thermo-Optical Effects

Locally heating a waveguide is a very efficient way of changing the refractive index. The refractive index increases with increasing temperature [77]. The temperature induced refractive index change has a time constant in the order of ms, dependent on the waveguide geometry, which makes it not suitable for high speed operation [66].

5.2 On-wafer Phase Characterization Based on Mach-Zehnder Interferometer

The first test module that we propose for characterizing phase modulation efficiency on-wafer is based on the Mach-Zehnder interferometer. This module was
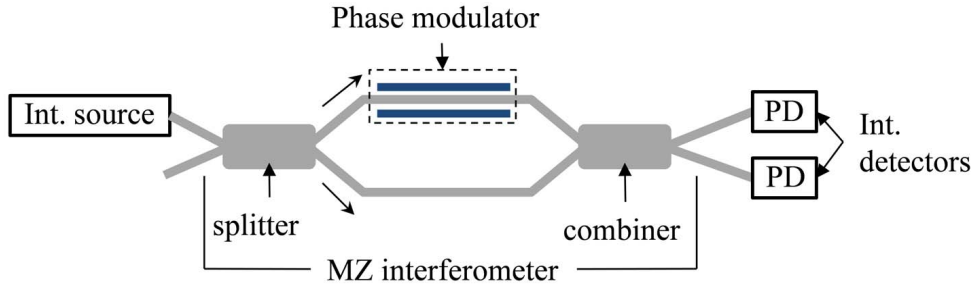
FIGURE 5.1: Schematic of the Mach-Zehnder interferometer that converts the phase modulation into amplitude modulation. The phase modulation is realized by a phase modulator present at one of the arms of the MZI.
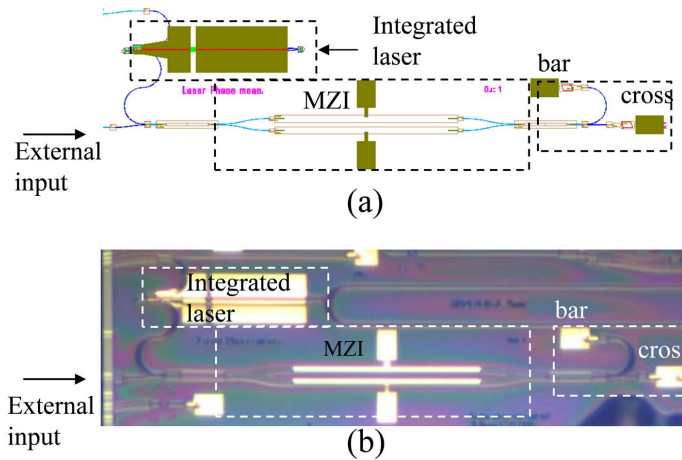
FIGURE 5.2: Mask layout in (a), and microscope photograph in (b) of the realized test module dedicated to on-wafer phase efficiency measurements.

tested in an MPW run by the company SMART Photonics (Smart 9 run). Its schematic is shown in Figure 5.1.

5.2.1 Test Module Design

The mask layout of the developed test module is shown in 5.2 (a), and the microscope photograph in Figure 5.2 (b). It features an integrated coupled cavity laser described in Section 3.4 [43], two integrated photo detectors, a Mach-Zehnder interferometer, and two phase modulators. The length of the phase modulator can be chosen arbitrarily. We chose a length of 1 mm as a good trade-off between a small footprint and an acceptable applied voltage for obtaining at least π phase change.

The waveguide composition of the phase modulator is bulk InP Q(1.25) which introduces a small electro-absorption at the operating wavelength of 1.55 μm [22]. The phase modulator in this technology exploits the carrier induced effects and the linear electro-optical effect [78].

FIGURE 5.3: On-wafer characterization of phase modulation efficiency for applied reverse bias. In blue the bar and in red the cross output of the MZI.

The integrated source provides the light that is coupled through the power splitter to the interferometer. By applying an electrical control signal to the phase modulator a phase change is obtained. The interferometric structure converts the phase modulation into amplitude modulation in both output waveguides through constructive and destructive interference in the combiner. The output waveguides are coupled to the integrated detectors.
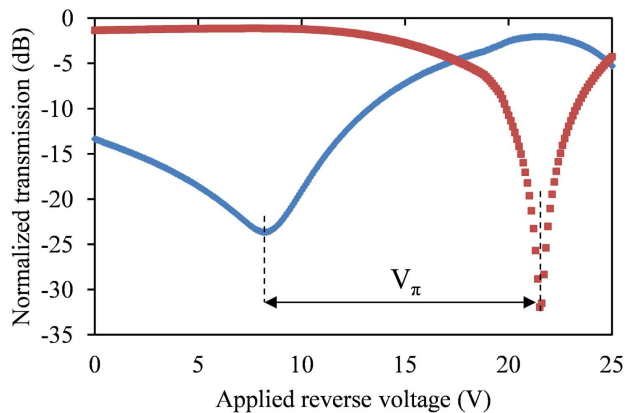
The power splitter and combiner of the integrated Mach-Zehnder based test module are realized as 2x2Multimode interference couplers because of their robustness to fabrication tolerances and their sufficiently large bandwidth [53, 54]. At the other input of the splitter a waveguide connected to the facet of the chip provides external access to the test module. The external input is used to increase the testability of the test module and compare the integrated on-wafer measurement with classical optical measurement.

To measure the phase modulation efficiency, the laser operating wavelength is kept constant while a phase sweep is performed at the modulator. The typical MZ transmission is measured at the detectors. The phase shift between maximum transmission and the consecutive minimum transmission is π.

5.2.2 Experiments

To characterize the phase in the electrical domain the integrated laser is biased above threshold by pumping 70 mA (35 mA at each SOA). Stable single-mode operating regime for the integrated laser requires a stable operating temperature that is achieved by using a temperature controller during on-wafer measurement. During measurement the temperature was set at 18°C. To fully absorb the incoming light at the integrated detectors fabricated in SMART Photonics a reverse biased of -2 V should be applied. Sweeping the modulator bias (and keeping the laser operating wavelength stable) the typical MZI transmission, measured in terms of photocurrent at the integrated photo detector, is shown in Figure 5.3.

To perform this measurement a total of four electrical sources is used, one current source (biasing the laser), one voltage sources (biasing the phase modulator), and two current meters (for the cross and bar outputs).

The reverse bias is swept to quite high voltages to be able to measure π phase modulation. The reverse bias needed to obtain π phase change is $V_\pi = 13.3$ V which is higher than expected (typical switching voltages for a 1 mm long PM in this technology is $V_\pi = 10$ V). Another anomaly is the large offset of the switching curves (the minimum of the bar output should be at 0 V, instead of -8.2 V). Both anomalies are to be attributed to the not sufficient etching of the devices which is particularly critical at the MMIs. If the input waveguides of the 2x2 MMI-couplers are not sufficiently etched the input fields couple to each other. The coupled input fields of the waveguides are responsible for an imbalanced splitting of the power at the two output arms with two main consequences: the switching curves are shifted (bar output not at the minimum for 0 V biased), and the mode coupling at the input waveguides imbalances the MZI (the 2 arms of the MZI are not symmetric anymore). To have good destructive interference both arms should have the same power and opposite phase. If imbalance is present in the arms of the MZI (due to coupled inputs of the MMIs in our case) the destructive interference cannot be complete, even though a π phase modulation is achieved. This translates in a low extinction of the MZI. In Figure 5.3 the extinction is better at the second dip due to the fact that the high applied reverse voltage introduces the needed insertion loss to one of the arms to balance the power to that of the other arm. The not sufficient etching at the input of the 2x2 MMIs was confirmed by SEM photographs and the imbalance by BPM simulation in OptoDesigner.

With the MZI based test module insertion loss of the phase modulator is not easy to measure, whereas absorption is limited since there is no noticeable power drop at the PDs at high applied voltages.

The measurement was repeated applying a forward bias to the phase modulator. The switching curves recorded with the integrated laser source, while forward biasing one of the phase modulators of the MZI are shown in dotted (cross in red and bar in blue) in the Figure 5.4.

Next we repeated the measurement with an external laser source (Agilent HP 8168A), which was coupled with a lensed fiber to the external input shown in Figure 5.2. The photo current, measured at the PD while forward biasing one of the phase modulators, is shown in solid in Figure 5.4. The switching curves of the electrical measurement are shifted by 5.28 mA, to compensate for the imbalance of the MZI. From the switching curves of both measurements a current needed to obtain a π phase modulation of $I_\pi = 12.8$ mA is obtained. The good match in terms of the optically and electrically measured I_π, despite the considerable imbalance of the MMIs, confirms the goodness of the integrated CCL and its validity when used in such a test module. No difference in MZI transmission is to be attributed to the different source used (integrated or external). The different extinction for the different nulls is again to be attributed to the imbalanced MMI. When forward biasing the phase modulator the phase change is caused by carrier induced effects, that mainly reduce the refractive index, and local heating that increases the refractive index. These effects have opposite signs. Given the
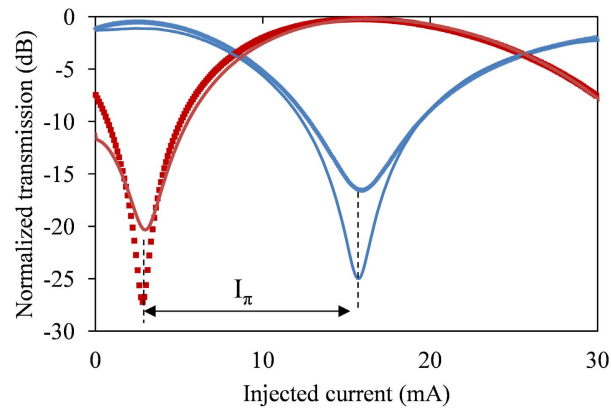
FIGURE 5.4: On-wafer characterization of phase modulation efficiency for applied forward bias using an internal laser source (dotted) and an external one (solid). In blue the bar and in red the cross output of the MZI.
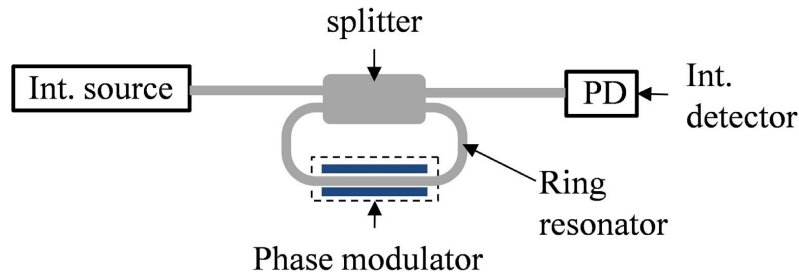
FIGURE 5.5: Schematic of the ring resonator test module that converts the phase modulation into amplitude modulation. The phase modulation is realized by the phase modulator inside the ring cavity.

composition of the phase section Q(1.25), however, the phase switching is to be attributed mainly to the thermo-optic effect.

The Mach-Zehnder based test module has a footprint of approximately 2 mm^2.

5.3 On-wafer Phase Characterization Based on Ring Resonator

The second test module that we investigated for characterizing phase modulation efficiency on-wafer is based on a ring resonator cavity. This test module was included at the PARADIGM run 2 at Oclaro. Its schematic is shown in Figure 5.5.

5.3.1 Test Module Design

The test module is shown in Figure 5.6. It features an integrated tunable DBR laser, an integrated photo detector, a high sensitivity ring cavity, and a phase modulator inserted inside the ring resonator. The length of the phase modulator
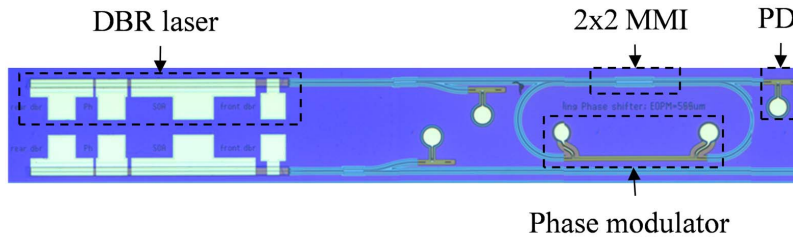
FIGURE 5.6: Microscope photograph of the realized test module for on-wafer phase efficiency measurements.

can be chosen arbitrarily. We chose a length of 500 μm as a good trade-off between a small footprint and an acceptable applied voltage for obtaining at least 2π phase change, which corresponds to one free spectral range in the ring transmission spectrum. The ring perimeter, 2.5 mm, is chosen accordingly. It is the minimum perimeter sufficient to insert a phase modulator of 500 μm and respect the minimum bending radius which in this technology is 150 μm.

The phase modulator is a passive waveguide with the core composed of a multi quantum well, so the highly efficient quantum-confined Stark effect is present [71]. The same waveguide structure is used in the modulator and the passive waveguides. The ring cavity is coupled to the DBR laser and detector through a 2x2 Multimode interference coupler. The DBR laser, as shown in Figure 3.5, has a continuous tuning capability of 0.4 nm by injecting current at the phase section. The 2x2 Multimode interference coupler is chosen for its robustness to fabrication tolerances [53, 54].

Due to the orientation of the phase modulator perpendicular to the major flat (parallel to the laser) the linear electro-optic effect is subtracted from the QCSE thus reducing the overall modulation efficiency. If the phase modulator is positioned parallel to the major flat both electro-optical effects, Pockels and QCSE, add-up resulting in a higher overall efficiency. The former orientation is chosen because of space constraints on the chip. With the current test module we characterize phase modulation efficiency for PM positioned perpendicular to the major flat. If the phase modulation efficiency needs to be characterization for the PM oriented parallel to the major flat another test module should be included in the test cell with as consequence a larger overall test cell.

To measure the phase modulation efficiency, the laser operating wavelength is kept constant while a phase sweep is performed with the modulator. The typical ring transmission is again measured at the detector. The phase shift between one resonance (minimum transmission) and the consecutive antiresonance (maximum transmission) is π radians.

An added benefit of this test module is the potential to characterize propagation loss too as shown in Chapter 4.

5.3.2 Experiments

To characterize the phase in the electrical domain the integrated laser is biased above threshold by pumping it with 25 mA ($I_{th} = 18$ mA), see Figure 3.7 (b).
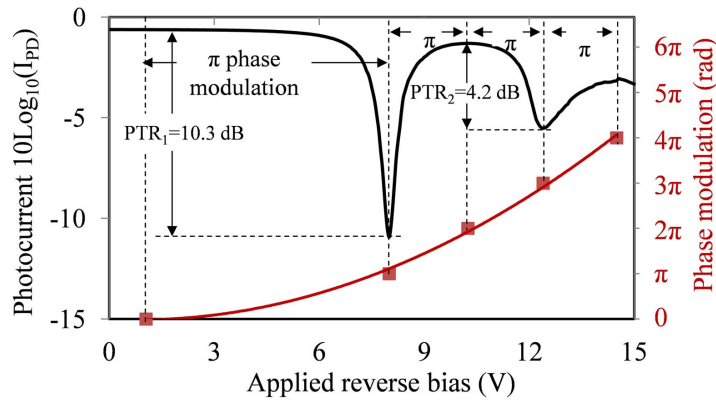
FIGURE 5.7: Ring transmission when the modulator phase is swept. One period corresponds to 2π phase modulation.

Stable single-mode operating regime for the integrated laser requires a stable operating temperature that is achieved by using a temperature controller during on-wafer measurement. During measurement the temperature was set at 18°C. To fully absorb the incoming light at the integrated detectors fabricated in Oclaro a reverse biased of -5 V should be applied. Sweeping the modulator bias (and keeping the laser operating wavelength stable) the typical ring transmission, measured in terms of photocurrent at the integrated photo detector, is shown in Figure 5.7.

In Figure 5.7 the measured phase shift is plotted with a quadratic fit as a function of the applied reverse bias voltage. The quadratic function is typical for tuning with the quantum confined Stark effect.
The round trip loss is composed of propagation loss, 2x2MMI excess loss, and modulator induced loss. The reduction in PTR between consecutive resonance dips as a function of reverse bias is due to the increased absorption in the phase modulator that, in turn, increases the round trip loss inside the ring. The values $PTR_1 = 10.3$ dB and $PTR_2 = 4.2$ dB correspond to a round trip loss of 1.6 dB and 10.3 dB. The 2x2MMI excess loss is $I^2 = 0.3$ dB, whereas the round trip loss (excluding coupler excess loss) is $\alpha_{ring}^2 = 0.7$ dB as measured in Chapter 4. The modulator loss is, therefore, 0.6 dB and 9.3 dB, respectively, at the working points of 8 V and 12.4 V reverse bias. A rapid increase of absorption is measured at high voltages.
The measurement was repeated by applying a forward bias sweep to the phase modulator (all the other conditions are kept identical). The measured photocurrent is shown in Figure 5.8. In Figure 5.8 the measured phase modulation efficiency is fitted with a quadratic curve as a function of the applied forward bias.
The $PTRs$ correspond to a round trip loss of 2.1, 2.4, and 2.5 dB. Considering the same coupler excess loss and waveguide loss, the phase modulator loss is 1.1 dB, 1.4 dB, and 1.5 dB at the corresponding working points of 47.3 mA, 75.3 mA, and 98.6 mA forward bias.
When applying a forward bias the phase modulation is to be attributed to the carrier induced effects and thermal effects, which are competing with opposite signs, reducing thus the overall efficiency. The phase modulation due to carriers
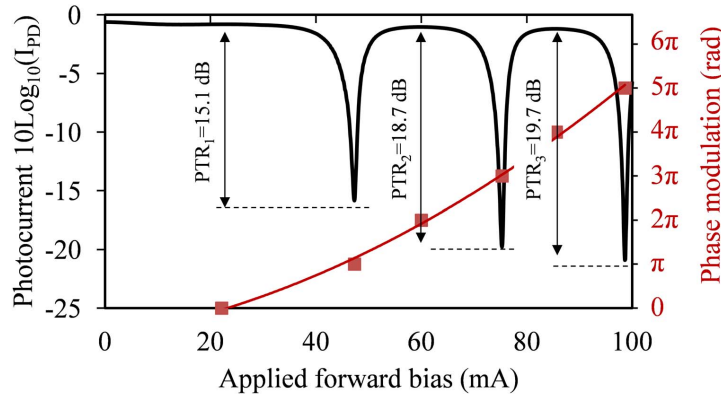
FIGURE 5.8: Ring transmission when the phase is modulated with an applied forward bias.

introduced in the junction has a linear dependence with current, whereas the phase modulation due to local heating has a quadratic dependence with current. Given the quadratic fit with current [79] the phase tuning is to be mainly attributed to thermal effects.

By using an integrated source, be it a coupled cavity or a DBR laser, no higher order modes or other polarizations are excited. Thus errors related to exciting the wrong polarization or higher order modes are greatly reduced. The absence of irregularities in the ring transmission (e.g. double dips or shoulders at the maximum transmission) gives a high level of confidence that only the fundamental transverse electric mode is present.

The ring resonator based test module has a footprint of approximately 1 mm^2. Phase modulation efficiency as well as phase modulator overall loss can be extracted from the ring based test module. Moreover, it needs one electrical signal less if compared to the MZI based test module. Another added benefit if compared to the MZI based test module is the possibility to use the RR based test module for both, phase modulation measurement and propagation loss measurement, as shown in Chapter 4. The test modules that we presented, due to space constrains, could not be implemented at the MPW run of the same foundry, thus a comparison between the two test modules in terms of phase modulation efficiency is difficult. Different foundries provide phase modulation by use of different InP electro-optical effects.

Another useful experiment is to implement the same PM BBB (from the same foundry) in the two test modules and verify that they both measure the same phase modulation efficiency. Due to space constrains, however, it was not possible to do it.

Characterizing on-wafer the phase modulation efficiency for the TM modulation, will be possible when a polarization converter is integrated in the generic process.

5.3.3 Accuracy Analysis

Different causes may affect the accurate determination of the phase modulation efficiency curves discussed in the previous section. Given the integrated nature
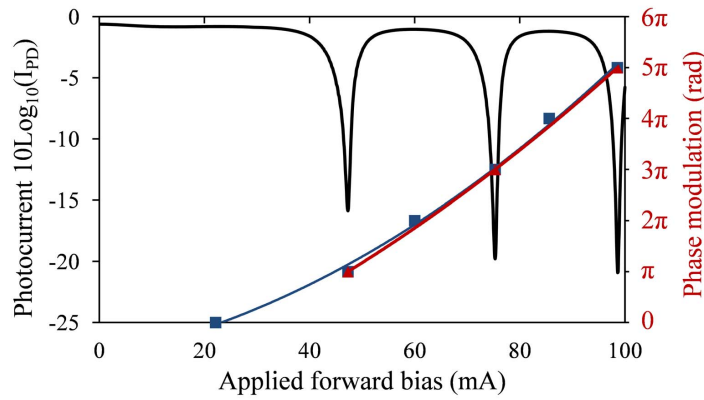
FIGURE 5.9: Ring transmission and phase modulation efficiency when, (in blue) both, maxima and minima, and (in red) only minima are considered.

of the test module only the fundamental TE polarized mode should be excited. Satisfying the design rules, such as using a radius not smaller than that advised by the foundry, and using the proper offset at the junction between a curved and a straight waveguide guarantees that the mode or polarization conversion in the curves and junctions is negligible. The well-defined single dips for both test modules give a high level of confidence that only the fundamental transverse electric mode is present. Different modes, be it higher order TE polarized mode or TM polarized mode, have different propagation constant than the fundamental TE mode, which would be visible in the ring transmission by the presence of multiple dips or other irregularities.

Extracting the minima and maxima of the ring transmission for determining the phase vs. voltage (current) efficiency curve can, however, be a source of error. This is mainly due to the fact that the maximum transmission of low loss ring resonators is quite flat and, therefore, susceptible to typical power variations of the laser or local temperature variations which might shift the maximum transmission affecting the phase vs. voltage (current) curve.

The error in extracting the maxima from the transmission curve of a low loss ring resonator can be reduced by implementing a ring with a higher round trip loss. The maximum transmission of such a ring is less susceptible to noise (less flat) at the expenses though of having a minimum transmission which is less robust to noise.

Determining the phase modulation efficiency curve only from the minimum ring transmissions is a more robust phase measurement. The well defined minima are less susceptible to small power fluctuations of the laser or temperature oscillations. We use this method to determine the phase modulation efficiency for the forward bias tuning.

The phase modulation efficiency curves are very similar, see Figure 5.9. However, considering only minima may lead to too few measured points as in Figure 5.7, therefore, it is important to determine what is the measurement error in this case. To do that the two quadratic fitting curves of Figure 5.9 are compared and the difference in modulation efficiency is calculated.

The difference in modulation efficiency is in the range $\Delta\phi = 3.2 - 6\%$. All the measured points vary with less than 6% from the fitted curve as well.

Another source of error is the minimum voltage (current) step used that might affect determination of the minimum or maximum. The error due to the limited step of 0.05 V and 0.1 mA is only 1% and 0.5% of the V_π, I_π respectively. This error, when considering several measurement points, will be small and, therefore, neglected in the final measurement accuracy.

5.4   Conclusions

In this chapter we report for the first time on-wafer phase measurement test modules dedicated to generic testing of phase modulators. The two proposed test modules, Mach-Zehnder based and ring resonator based, use electrical signals only thus avoiding the time consuming optical alignment and, therefore, speeding up the overall characterization process.

A very good match between optical and electrical measurements was observed for the MZ based test module. For the ring-resonator-based test module a good fit between the phase modulation efficiency and the expected behaviour of the phase modulator is shown.

The overall footprint of the Mach-Zehnder based test module is 2 mm^2, whereas that of the ring resonator is only 1 mm^2. The ring resonator based test module can be used for on-wafer measurements of phase modulation as well as propagation loss, reducing thus the overall generic test cell footprint. It also provides an indication of phase modulator loss during operation.

Comparison of the two test modules in terms of the measured phase modulation efficiency was not possible since the modules were not present on the same foundry MPW run.

Chapter 6

Modal Gain Characterization Method

6.1 Introduction

One of the main basic building blocks within the generic foundry approach is the Semiconductor Optical Amplifier (SOA). It is the core element in every integrated laser source. Therefore, its accurate characterization in terms of modal gain is fundamental to the overall performance of the PIC. The main methods proposed for measuring modal gain are the Hakki-Paoli [11, 80], the Thomson [81], and the fitting algorithm method [82]. The draw-back of the Hakki-Paoli method is the need to measure with high accuracy the modulation depth of the Amplified Spontaneous Emission (ASE) resonances of a laser cavity that operates below threshold. For typical chip lengths a very high resolution spectrum analyzer is needed for resolving the longitudinal modes. The fitting method [82] makes use of a non linear least square fitting algorithm that calculates the modal gain and the spontaneous emission for each wavelength from the measured ASE of SOAs with different length, pumped at the same current density. The draw-back of this method lays in the large number of SOAs needed, in [82] 26 SOAs were used. The Thomson method in turn needs only two SOAs with length L and $2L$ to determine the modal gain. Our approach is based on the Thomson method. The novelty of our approach lies in the integration of the SOAs with a wavelength demultiplexer and an array of integrated detectors. The integration of the SOAs with the wavelength demultiplexer and a detector array allows for electrical on-wafer characterization without the need to couple optical signals out of the chip.

6.2 Thomson Method

In Figure 6.1 two SOAs of 200 μm and 400 μm length are shown. At the left output of the SOAs a photodetector is connected which, when reversely biased, absorbs the incoming light thus avoiding feedback. The right output of the SOAs exits the chip through an angled waveguide, to minimize reflections. The ASE, emitted by the SOAs when forward biased, is collected by lensed single mode fibers, connected to an optical spectrum analyzer.
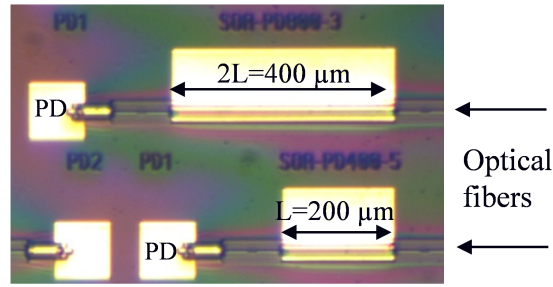
FIGURE 6.1: SOA pair 200-400 μm long. The photodetectors on the left are reversely biased during measurement to avoid feedback. The lensed fiber collects the amplified spontaneous emission.
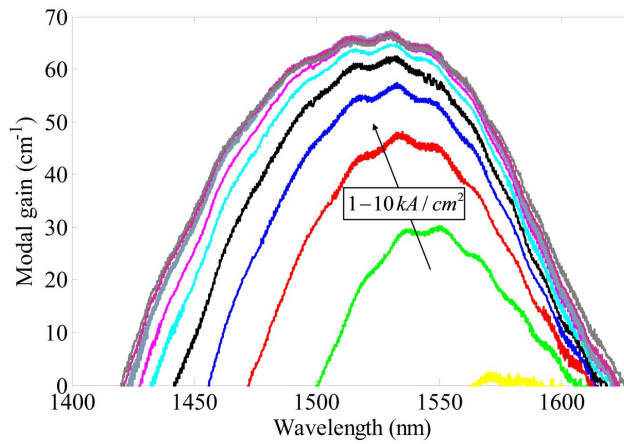
FIGURE 6.2: Modal gain curves for varying current densities, 1-10 kA/cm^2 for the 200-400 μm long SOA.

In absence of feedback the modal gain G and the *ASE* power intensity I are related by [81]:

$$I = \frac{I_{SE}}{G} \left(e^{GL} - 1 \right) \tag{6.1}$$

with I_{SE} spontaneous emission intensity and L the SOA length. The net modal gain, obtained by comparing the *ASE* intensity (6.1) emitted from SOAs with lengths L and $2L$ when pumped with the same current density, is:

$$G = \frac{1}{L} \left[\ln \left(\frac{I(2L)}{I(L)} - 1 \right) \right] \tag{6.2}$$

By applying (6.2) to the *ASE* emitted from the SOA pair the modal gain curves of Figure 6.2 are obtained.

6.3   Test Module Design

The schematic of Figure 6.3 represents the test module for on-wafer gain measurement using the Thomson method. It comprises a multi-section SOA (containing
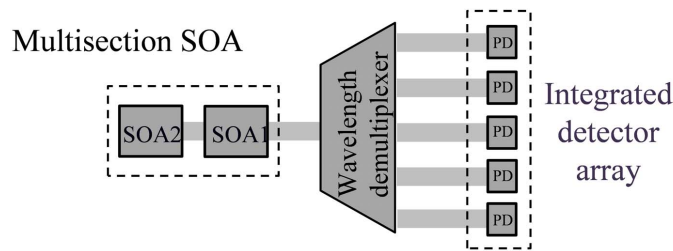
FIGURE 6.3: Schematic of the integrated modal gain test module. It is composed of a multisection semiconductor optical amplifier, a wavelength demultiplexer, and an array of integrated detectors.
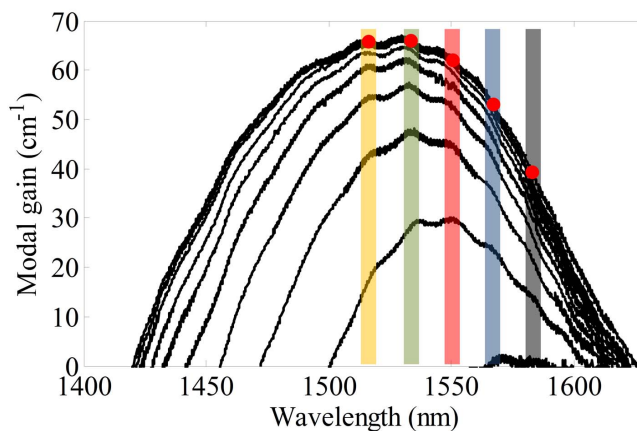
FIGURE 6.4: On-wafer gain measurement concept that uses a wavelength demultiplexer to sample gain at the wavelengths of interest.

at least a pair of SOAs) as integrated input, a wavelength demultiplexer, and an array of integrated detectors. The wavelength demultiplexer spectrally resolves the *ASE* emitted from the SOA pair into the corresponding integrated detector. The on-wafer gain measurement concept is shown in Figure 6.4. The different colors represent the different demultiplexer passbands. The gain curves, obtained for different current densities (1-10 kA/cm^2), are the same as shown in Figure 6.2. The red dots represent the modal gain values for 10 kA/cm^2 current density, to be measured at the respective filter passband through the implemented on-wafer electrical method.

The mask layout of the test module is shown in Figure 6.5 (a) and the microscope photograph of the realized one is shown in Figure 6.5 (b). The multi-section SOA of the realized chip consists of four cascaded SOAs of different length (200-200-400-800 μm), electrically isolated from each other, see Figure 6.5. By pumping different combinations of the four SOAs the following SOA pairs are obtained: 200-400 μm, 400-800 μm, and 800-1600 μm. Ideally only one SOA pair is enough to calculate modal gain, as shown in Figure 6.2. Here more SOA pairs were used to compare modal gain measured with different SOA pairs. Light emitted in the opposite direction is absorbed by the un-pumped SOAs thus preventing unwanted feedback.
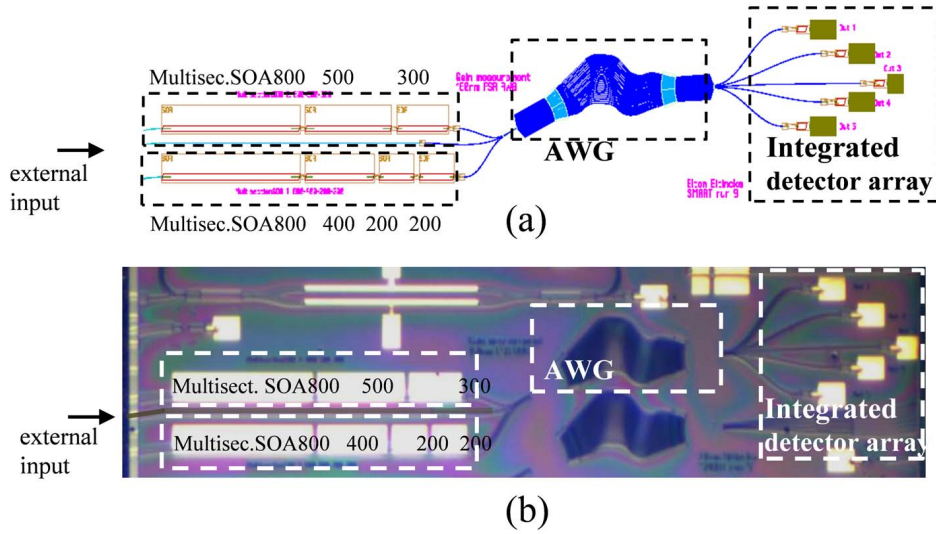
FIGURE 6.5: Mask layout in (a), and microscope photograph in (b) of the realized integrated modal gain test module based on the Thomson method. The multisection SOA, the arrayed waveguide grating, and the detector array are indicated in the figure.

For the wavelength demultiplexer we used an Arrayed Waveguide Grating (AWG). The AWG is widely used in telecom applications. A detailed analysis of the AWG can be found in [83]. At each of the PDs, connected to the outputs of the AWG, the modal gain at that wavelength is measured. The external input is included to characterize the AWG response as will be described further on. The other multisection SOA (300-500-800 μm) shown in the figure was not used in this experiment.

We are interested in characterizing the modal gain in the C-band (1530-1565 nm). An AWG with five channels: a central channel at 1550 nm, and a channel spacing of 10 nm would cover the full C-band. In order to be less sensitive to shifts of the gain spectrum we decided to sample the spectrum also beyond the C-band. The designed AWG has, therefore, five channels with the central one at 1550 nm, and a channel spacing of 20 nm to best cover the C-band and beyond. Moreover, for a given FSR, larger channel spacing reduces the footprint. The larger channel spacing did not affect the the calculated gain. The larger wavelength window, provided by the 20 nm channel spacing design, offers a more optimal coverage of the gain curves for the different current densities (gain curves show a significant blue shift with increasing current density).

6.3.1 Large Free Spectral Range AWG

As already introduced in the previous section, a large free spectral range AWG is needed to cover the 1500-1600 nm wavelength window. Typical AWG designs cannot have such a large free spectral range since a very large FSR means a very

FIGURE 6.6: Flipped AWG design suitable for very large free spectral range in (a), and a SEM photograph of the arm array exiting the first free propagation region of the realized flipped AWG in (b).

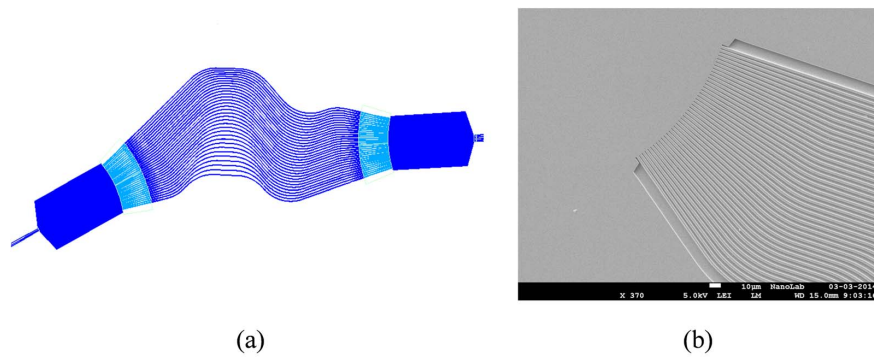small arm length difference in the array, and thus, very closely spaced waveguides. To overcome this problem a special AWG design is required.

Several designs for large FSR are proposed in literature. In [84] the "w" shape is proposed with the path length difference implemented by using a different radius of curvature. In [85] the proposed AWG layout is the typical rectangular shape with constant radius for all the arms but different overall arc. The increase in FSR is obtained by decreasing the arm aperture pitch. In both designs the FSR cannot be made arbitrary large since at a certain point the array arms are too closely spaced. An antisymmetric AWG layout, as a mean to increase the FSR was first proposed in [86]. The path length difference was realized by using arcs with the same angle but different radius. The same AWG layout and the same way of achieving the arm length difference was used in [87] for a coarse wavelength division multiplexing application.

The large FSR AWG of our choice is developed by Bright Photonics [88]. It overcomes the densely spaced waveguide problem by adding extra arm length which increases the space between the adjacent arms. This dispersion introduced by the extra arm length is compensated in the second half of the AWG which is "antisymmetric" with respect to the first half. With this method an AWG with an arbitrarily large FSR can be realized. In typical AWG designs the length difference between arms is realized by having bends with different radius and/or different total arc. Bends with different radius, however, have a different refractive index, leading to different optical paths. The change in refractive index as a function of radius can be predicted and accounted for but may not lead to perfect phase error cancellation due to simulation inaccuracies and processing tolerances. The designed AWG has a constant total arc, as well as constant radius for each arm of the array. The arm length difference is realized only at the straight waveguides section, making this design less sensitive to process imperfections, thus less phase errors. Measurement of the AWG transmission, presented in the next section, confirms the small phase errors of this design. The large FSR AWG design is shown in Figure 6.6 (a), whereas a scanning electron microscope photograph is shown in Figure 6.6 (b).
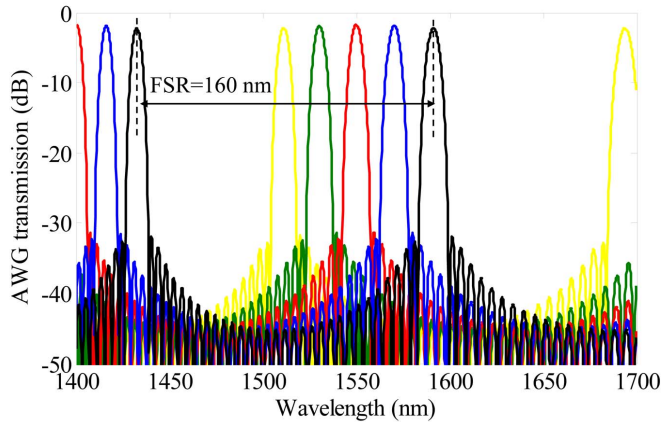
FIGURE 6.7: Simulated transmission of the designed large free spectral range arrayed waveguide grating.

An AWG shape similar to ours, realized in SiON technology for sensing applications, is proposed in [89].

Due to the periodic nature of the AWG, and the broad wavelength range of the *ASE* emission, the adjacent order of the AWG will still capture some *ASE* power. This *ASE* power will be collected by the detectors and, as we will see in the next sections, reduces the gain measurement accuracy. Therefore, it should be reduced as much as possible by choosing an AWG with an FSR as large as possible. For our *ASE* measurement window (1400-1630 nm) a 240 nm FSR AWG would be desirable. However, to reduce the AWG footprint an FSR of 160 nm is chosen and implemented since for a given channel spacing increasing the FSR increases the AWG footprint. The 160 nm FSR is a good trade-off between measurement accuracy of the test module and its footprint. The overall footprint of this test module is 4 mm^2. The transmission of the designed AWG is simulated with a Beam Propagation Method (BPM) module of OptoDesigner Phoenix Software, and shown in Figure 6.7.

6.4 Accuracy Analysis

The large FSR AWG and the PD array, that comprise the on-wafer test module for characterizing the SOA modal gain, have a non-ideal behavior which affects the modal gain measurement accuracy. To quantify the measurement accuracy we focus on AWG related error sources, and on PD response related error sources. Also the SOAs have reproducibility limits as we saw in Section 3.2. In the next sections these error sources are analyzed.

6.4.1 SOA Related Error Sources

Even though the test module that we propose in this chapter is meant to characterize the SOA performance in terms of modal gain the SOAs themselves can introduce uncertainties and measurement errors. In this section we analyze how the reproducibility limits of the SOA-PD structure affects the gain measurement.

In Section 3.2 we showed that the Integrated Source Detector structure has a reproducibility limit of 0.4 dB (the worst wafer, see Figure 3.2 (a)). The 0.4 dB was the upper variation limit from the average of any ISD structure. This limit was determined while characterizing 40 ISDs under the same operating conditions: a forward bias ranging from 1-10 kA/cm² in 10 steps applied to the SOAs, and 0 V bias applied to the PDs, that absorb more than 95% of the incoming light. The same operating conditions are used in this chapter.

The reproducibility limit of 0.4 dB corresponds to less than 10% variation in ISD transmission. While changing the applied bias of the PDs and/or the current density of the SOAs no significant variation of the ISDs performance was measured. However, we have little information on how this power variation is distributed over the spectral window.

We assume that the 10% variation in ISD transmission is the same over the measurement wavelength window. Therefore, at each of the five AWG channels there is in first approximation an average error of 10%. Applying to equation (6.2) a 10% higher value to the measured ratio $I(2L)/I(L)$ the error in modal gain is within the range $\Delta G = 6.5 - 7.6 cm^{-1}$ for the current densities 3-7 kA/cm². This value, as we will see in the next sections, is quite high and comparable to the largest error source due to the central wavelength shift of the AWG, see Section 6.4.2.3.

The 10% transmission difference is quite high and introduces a significant error in calculating modal gain. This modal gain error due to the reproducibility limit of the ISDs does not only affect the integrated measurements, it affects the classical Thomson method too. During integrated measurements, however, the inclusion of a test module that comprises several ISDs, as the ones shown in Figure 3.1, is helpful in determining the accuracy resolution that is achievable in that wafer. In our case on the wafer W150-1 processed at SMART Photonics, the ISDs have a reproducibility limit of 0.4 dB, see Figure 3.2 (a) which translates into a gain measurement accuracy not better than 7.6 cm⁻¹. However, in wafer W150-3, see Figure 3.2 (b), the ISDs reproducibility limit is 0.2 dB which translates in a better gain measurement accuracy of approximately 4 cm⁻¹.

6.4.2   AWG Related Error Sources

The AWG is a complex optical component described by many parameters. We focus here on those parameters that mostly affect the modal gain measurement accuracy. These parameters are:

1. *crosstalk*: defined as the difference between the maximum transmission of an AWG channel and the crosstalk floor.

2. *roll-off*: defined as the insertion loss of the outer channels with respect to the central one.

3. *central wavelength shift*: defined as the difference between the designed and the measured AWG central wavelength.

4. *Free Spectral Range of the AWG*: defined as the AWG periodicity in the wavelength domain.
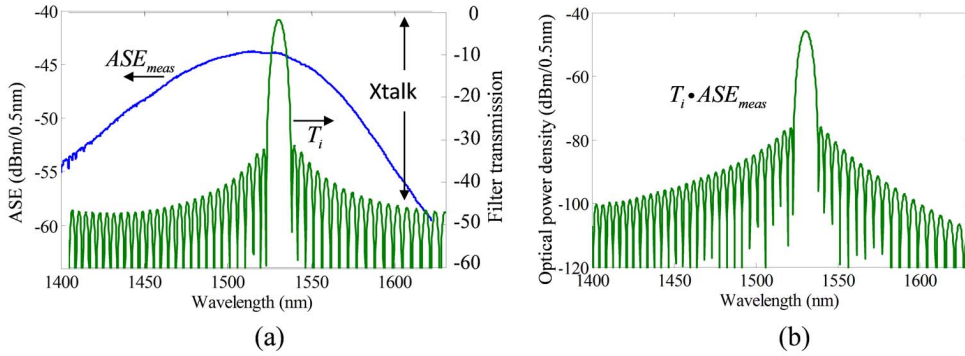
FIGURE 6.8: Measured *ASE* of a 400 μm long SOA and the simulated transmission of an AWG channel in (a), and optical power density collected by the real filter in (b).

In the following sections we analyze these parameters and their effect on the measurement accuracy.

6.4.2.1 AWG Crosstalk

To calculate the modal gain at a specific wavelength ideally a very narrow filter, centered at the wavelength of interest, that samples the *ASE* at that specific wavelength is needed. Such an optical filter, however, does not exist. In Figure 6.8 (a) the simulated response of one of the AWG outputs, and the measured *ASE* from a 400 μm long SOA pumped at 5 kA/cm² are shown. The AWG crosstalk, defined as the difference between the maximum AWG transmission and the crosstalk floor, is shown too. Typical AWG crosstalk values are in the order of -20 dB to -30 dB.

The *ASE* power, after being filtered by the corresponding AWG channel, is absorbed by the respective PD. The PD absorbs all the incoming light over a broad wavelength range, including spectral crosstalk, therefore, it is clear that crosstalk is detrimental to the measurement accuracy. To quantify the crosstalk induced modal gain error we first calculate the *ASE* power that is collected by the respective AWG channel and absorbed by the detector.

$$I_i = \int (ASE_{meas} \cdot T_i) d\lambda \quad i = 1, ..., 5 \tag{6.3}$$

with T_i the simulated AWG channel transmission. In (6.3) the assumption of an ideal detector is made with the PD absorption constant at each wavelength. We deal with the detector induced gain error later on in this chapter. In Figure 6.8 (b) the *ASE* spectral power, absorbed by the PD, is depicted in green. The crosstalk floor is 30 to 40 dB less than the max transmission of the AWG channel but it extends over a large wavelength region, therefore, the power absorbed by the detector due to crosstalk cannot be neglected. $I_i(2L)$ and $I_i(L)$, calculated through equation (6.3), is the total *ASE* power absorbed by the PD when the SOAs with
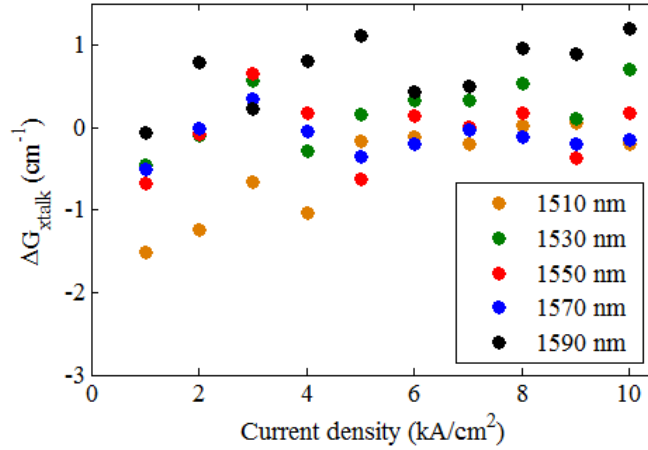
FIGURE 6.9: Crosstalk induced gain error at the AWG output wavelengths calculated for different current densities.

lengths L and $2L$ are pumped at the same current density. To calculate the modal gain from the filtered ASE equation (6.2) is used.

We define the *crosstalk induced gain error* ΔG_{xtalk} as the difference between the optically measured ideal modal gain $G(\lambda)$ at the measured wavelength, calculated with equation (6.2) and shown in Figure 6.2, and the estimated gain G_{est} calculated at the wavelength of the AWG passbands using equation (6.3).

$$\Delta G_{xtalk} = G(\lambda) - G_{est} \tag{6.4}$$

where from $G(\lambda)$ only the modal gain at the wavelengths that correspond to the AWG passbands is considered.

The crosstalk induced gain error according to equation (6.4) is plotted in Figure 6.9. For G_{est} we neglect crosstalk effects from adjacent orders, which are discussed in Section 6.4.2.4. In Figure 6.9 the crosstalk induced gain error is calculated at all the AWG output wavelengths and for different current densities (1-10 kA/cm^2). This gain error is calculated for the 200-400 μm long SOA pair. Similar values apply for the 400-800 μm long pair.

The crosstalk induced gain error is small, up to a few percent of the maximum gain, and only weakly dependent on the wavelength since crosstalk itself has a small wavelength dependence.

6.4.2.2 AWG Roll-off

The far field of the array waveguide gratings has its maximum intensity at the central channel receiver. This focal field intensity drops while moving towards the outer channel receivers. This intensity drop is often called roll-off. An AWG where the FSR is equal to the channel spacing times the number of channels is called a cyclic AWG.

For large numbers of AWG channels channel 1 of main order and the virtual channel $N + 1$ of the next order will experience similar loss (with N the total
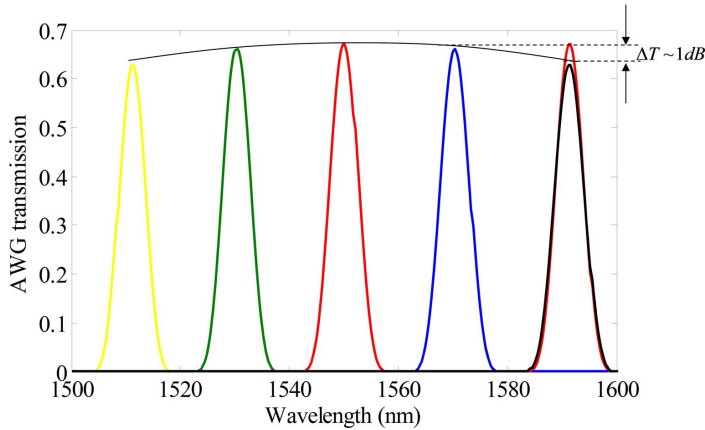
FIGURE 6.10: Simulated AWG transmission with in evidence the roll-off of the outer channel. The non roll-off ideal channel five is shown in red whereas the one with roll-off is shown in black.

number of channels), each of them has at least 3-dB excess loss relative to the central channel [83].

Our AWG is not a cyclic one, which helps reducing the gain error due to reduced *ASE* contributions from the secondary grating orders, as we will see in the next sections. In Figure 6.10 the BPM simulation of the 160 nm FSR AWG, introduced in the previous sections, is shown again with the focus on the outer channel roll-off. Here linear units are used to make the roll-off better visible. As expected roll-off in our AWG is smaller than in a cyclic one.

Different AWG passbands filter different amounts of *ASE* power, which lead to errors when calculating modal gain. To quantify the modal gain error induced when using an AWG affected by roll-off we proceed as in the previous section by calculating the *ASE* power, collected by the outer channel in case it is not affected by roll-off, and absorbed by the respective PD

$$I_{ideal\ i} = \int (ASE_{meas} \cdot T_{ideal\ i}) d\lambda \quad i = 1, ..., 5 \tag{6.5}$$

with $T_{ideal\ i}$ the simulated AWG channel transmission without roll-off, in Figure 6.10 channel 5 in red. The assumption of ideal PD response in (6.5) is again made. $I_{ideal\ i}(L)$ and $I_{ideal\ i}(2L)$, calculated through equation (6.5), is the total *ASE* power absorbed by the PD when SOAs with lengths L and $2L$ and filtered by non roll-off AWG channels, pumped at the same current density. To calculate the modal gain from the filtered *ASE* equation (6.2) is used.

We define the *roll-off induced gain error* ΔG_{ideal} as the difference between the estimated modal gain G_{est}, obtained from equations (6.3) and (6.2), and the one without roll-off G_{ideal}, obtained from (6.5) and (6.2)

$$\Delta G_{ideal} = G_{est} - G_{ideal} \tag{6.6}$$

where for G_{est} the *ASE* from adjacent order was neglected as in the previous section. In Figure 6.11 the roll-off induced gain error is calculated at the AWG
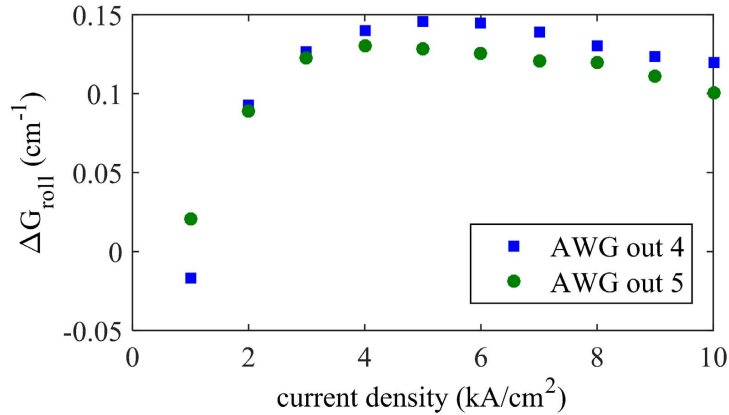
FIGURE 6.11: AWG roll-off induced gain error at the AWG outer channels calculated for different current densities.

output channels 4 and 5 for current densities 1-10 kA/cm^2. The gain error at channels 1 and 2 is similar to the one in channels 4 and 5 due to the symmetry of the AWG passband with respect to its central channel. In Figure 6.11 the roll-off induced gain error is calculated for the 400-800 μm long SOA pair. Similar values are found for the 200-400 μm long pair.

The gain error is similar in channel 4 and 5 even though the AWG roll-off in channel 5 is more severe than in channel 4. From Figure 6.11 it can be seen that roll-off induced gain error is hardly dependent on current except for low current densities. As to be expected the roll-off induced gain error is very small since the AWG passband difference is canceled out when calculating gain, therefore, it does not present a major issue when the total gain error is calculated.

6.4.2.3 Central Wavelength Shift

The central wavelength shift of an AWG is difficult to control. It is mainly due to variations in waveguide width and layer stack thickness during processing. Statistical data from the last MPW runs processed in our InP generic integration technology show a central wavelength shift up to 5 nm compared to the design value.

Since the whole AWG transmission shifts with the central channel wavelength this wavelength shift would not be a problem if a calibration of the AWG could be done before hand or a better knowledge on the AWG central wavelength shift from one MPW run to the other was present. However, the test module that we propose is meant to be used for on-wafer gain measurement, thus a calibration is not possible.

In this section we translate the wavelength shift of the gain curves due to the central wavelength shift of the AWG into a modal gain error per each AWG channel. By doing so we uniform the way we calculate the modal gain error for the different error sources. This uniformity allows us to compare the gain error sources and estimate the overall gain error.

In Figure 6.12 the concept of gain measurement is illustrated together with a visual explanation of the wavelength shift induced gain error. In solid the five AWG
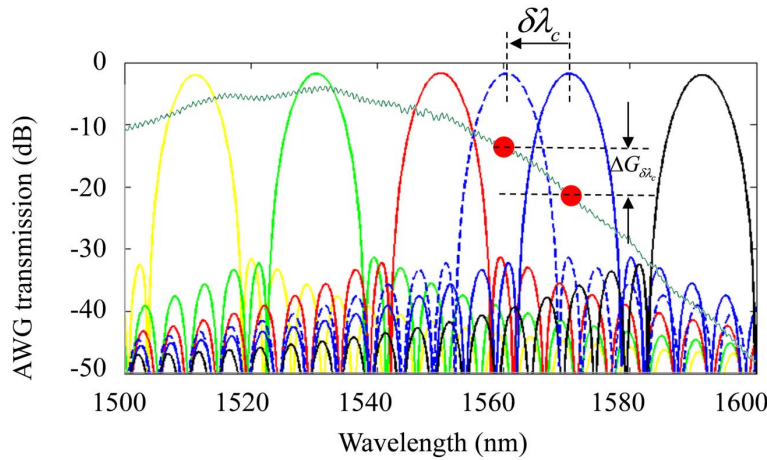
FIGURE 6.12: Simulated AWG transmission and optically measured modal gain. The solid curves are the ideal AWG passbands (no central wavelength shift), and channel 4 with a 10 nm blue shift is shown in dashed. The red dots represent the modal gain that is measured by the ideal channel 4 and by the 10 nm blue shifted one.

passbands (without central wavelength shift) are shown, and in dashed channel 4 is shown with a 10 nm blue shift. The other channels have the same shift but are not shown for clarity.

The gain has a zero slope at its peak, therefore, for a small AWG wavelength shift, at the corresponding AWG channel a zero gain error should be present. As can be seen from Figure 6.12 an AWG wavelength shift leads to sampling the gain at different wavelengths, thus leading to an error in gain measurement.

To analyze how much a typical AWG central wavelength shift affects the gain measurement we calculate the *ASE* power that is collected by the respective AWG channel, which is wavelength shifted by $\delta\lambda$ with respect to the ideal AWG transmission.

$$I_{\delta\lambda i} = \int (ASE_{meas} \cdot T_i(\lambda - \delta\lambda))d\lambda \quad i = 1, ..., 5 \tag{6.7}$$

with $T_i (\lambda - \delta\lambda)$ the i-th AWG passband shifted over $\delta\lambda$. From the *ASE* intensity (6.7), and (6.2) the modal gain is calculated. We define the *central wavelength shift induced gain error* $\Delta G_{\delta\lambda_c}$ as the difference between the modal gain calculated with the ideal AWG transmission, obtained from (6.3) and (6.2), and the one with shifted AWG passband, calculated from (6.7) and (6.2)

$$\Delta G_{\delta\lambda_c} = G_{est} - G_{\delta\lambda_c} \tag{6.8}$$

To quantify the central wavelength shift induced gain error eq. (6.8), and G_{est} for an infinite FSR AWG is used. In case of a central wavelength shifted AWG the wavelength dependence of the gain curve is of primary importance for the measurement error. In Figure 6.13 the central wavelength shift induced gain error is calculated for the 200-400 μm long SOA pair at a current density of 5 kA/cm^2 (typical value for biasing SOAs). Similar errors are obtained for the 400-800 μm
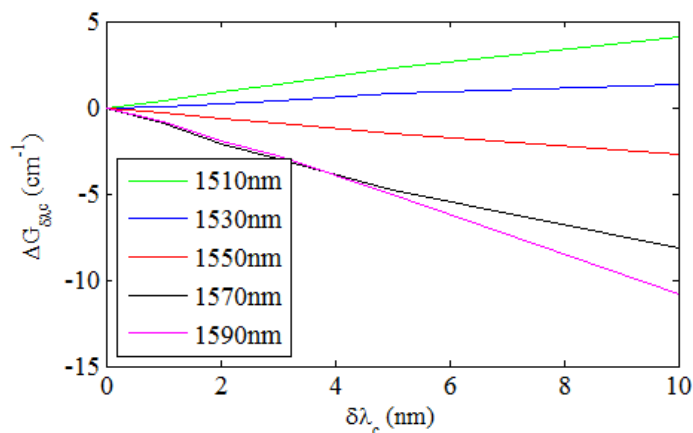
FIGURE 6.13: AWG central wavelength shift induced gain error calculated for different wavelength shifts at all the output channels.

long SOA pair and different current densities, they are not shown. As can be seen from Figure 6.13 the outer channels have a larger gain error since the gain curve has a larger slope. As already mentioned the maximum AWG central channel shift in our technology is up to 5 nm, which causes a modal gain error of a few percent with respect to the peak gain at the central wavelengths and up to 13 % at channel 5. In Figure 6.13 the errors are shown for blue shifts up to 10 nm. In case of red shift similar values are found, with an opposite sign.

6.4.2.4 Adjacent AWG Orders

Adjacent grating orders of the AWG collect *ASE* power too. The *ASE* power collected from the adjacent grating orders is added to the *ASE* power from the main grating order and absorbed by the detector. We have no means to distinguish which part of the photocurrent is due to *ASE* collected from the main grating order and which part is due to the adjacent ones. Therefore, the *ASE* power collected by adjacent grating orders is causing an error in the on-wafer modal gain measurement. Given the *ASE* intensity drop in the 1400 nm and 1600 nm wavelength region, an FSR of a few hundred nm would bring down the gain error to a few percent, comparable to the other measurement uncertainties. Increasing the FSR however, for a given channel spacing, increases the AWG footprint, thus a trade-off between footprint and modal gain accuracy should be made. In Figure 6.14 the effect of the finite FSR (smaller than 200 nm) on the collected *ASE* power from the adjacent grating orders is shown. The FSR induced gain error can be calculated with similar formulas as in the previous sections. We analyze the finite FSR induced gain error together with that of the PD response related gain errors since, as we show in the next section, they are very similar errors, and therefore, their analysis can be combined.

6.4.3 PD Response Error Sources

The photo detector response is another parameter to be considered when calculating the overall gain measurement accuracy. In Figure 6.15 the simulated AWG
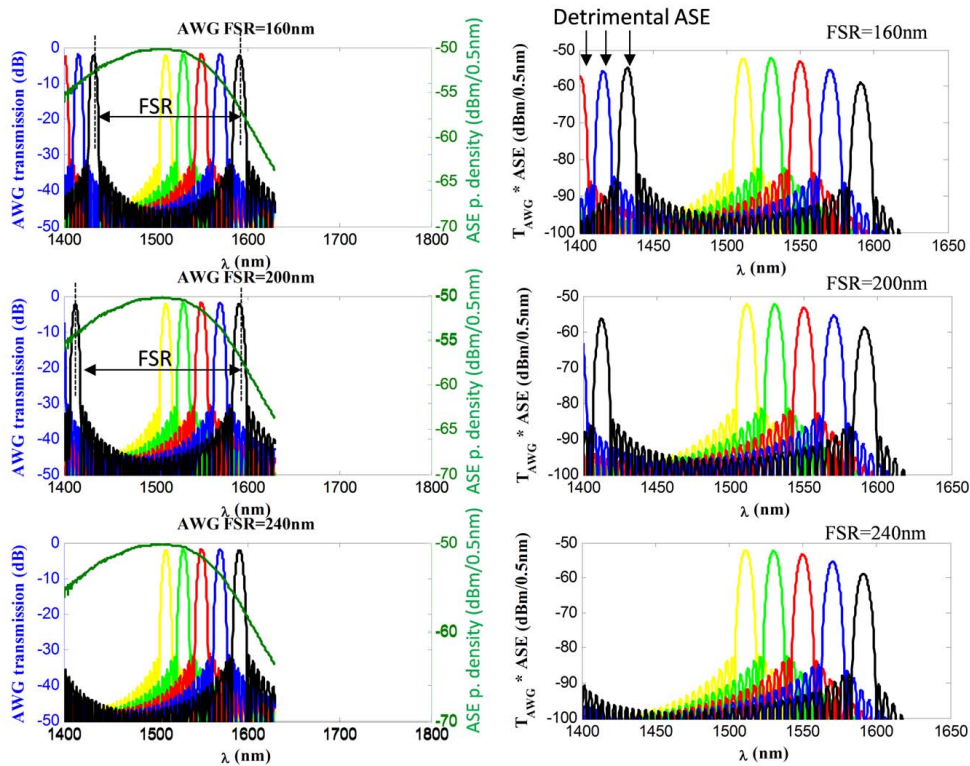
FIGURE 6.14: Figures on the left show the *ASE* for the 200 μm long SOA at 5 kA/cm^2 together with the AWG transmission for 160 nm, 200 nm, and 240 nm FSR. Figures on the right show the *ASE* spectrum filtered by the AWG channels. The effect of a small FSR is clearly observed.

transmission response and the measured PD absorption response are shown. To measure the PD response, shown in Figure 6.15, TE polarized light was coupled in the PD access waveguide through a lensed fiber. The lensed fiber was connected to a HP tunable laser (Agilent 81600B), which covers the wavelength range 1440-1640 nm. The photo current, collected by the PD (biased at 0 V), was recorded
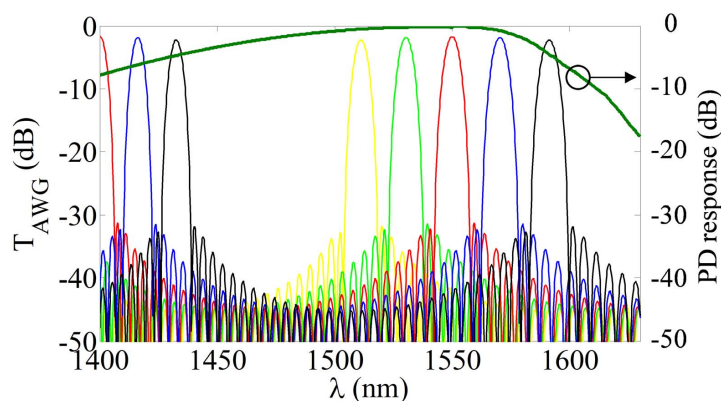
FIGURE 6.15: Simulated AWG transmission and measured PD response.

during a full wavelength sweep. The recorded photo current was corrected for the laser peak power drop (laser peak power is not constant over the whole wavelength range). To extend the PD response to shorter wavelengths, and match it with the 1400-1630 nm range of the *ASE* (measured with an ANDO AQ-6315A Optical Spectrum Analyser), the final PD response was extrapolated for the range 1400-1440 nm using a second order polynomial fit in the 1440-1500 nm.

The photocurrent, for a given wavelength, is proportional to the incident optical power. The quantum efficiency, defined as the ratio between the number of generated electron-hole pairs and the number of photons, is wavelength dependent (varies with photon energy). So is the responsivity, defined as the photocurrent generated per unit optical power. The photodetector response, shown in Figure 6.15, is the normalized photocurrent. The drop in PD response at short wavelengths is due to the quantum efficiency, and to the increased photon absorption near the junction between the waveguide and the photodetector. For short wavelengths the absorption coefficient is higher thus light penetrates less in the active area, and as a consequence is absorbed near the waveguide-detector junction. Close to the junction the recombination time is shorter (plenty of recombination centers) thus more photo carriers recombine non-radiatively [44]. The quantum efficiency drop has a linear dependence on the wavelength. For the overall photocurrent drop at short wavelengths, a quadratic fit, that takes into account increased absorption at the device edge too, is more appropriate.

The drop at long wavelengths is due to the bandgap of the absorbing material used in the PD, which is a multiquantum well with a composition such that the band edge is at a wavelength of 1.55 μm. The PD was biased at 0 V for reducing the PD dark current. Another benefit of the 0 V biased PD is the strong cut-off in absorption at longer wavelengths. The secondary grating order, centered at 1700 nm, is thus reduced by at least -25 dB. If a higher reverse bias voltage is applied the band edge shifts towards longer wavelengths, thus *ASE* absorption at the secondary grating order is larger, which reduces our measurement accuracy.

In Figure 6.16 the simulated AWG transmission for 160 nm, 200 nm and 240 nm FSR, the *ASE* collected by the simulated AWGs, and finally, the measured *ASE* collected by the simulated AWG transmissions and absorbed by the PDs are shown. The *ASE* curve is measured for a 200 μm long SOA pumped at 5 kA/cm^2, whereas the PD response is obtained for 0 V bias. The AWG simulation is done for an FSR of 160 nm, 200 nm, and 240 nm. In this way we are able to distinguish between the finite FSR related gain error and the PD response related one. It is clear that the error introduced by channel 4 and 5 of the adjacent grating order, is reduced by the reduced PD responsivity at those wavelengths. This is even more clear if the 200 nm FSR AWG is considered. Channel 5 at the adjacent grating order is reduced by at least 5 dB when the PD response is considered.

To analyze the effect of the PD response and of the finite FSR on the gain error quantitatively we take into account the typical PD response and AWGs with three different FSRs: 160 nm, 200 nm, and 240 nm. The adjacent grating order of the 240 nm FSR AWG is outside our measurement window. The *ASE* power collected
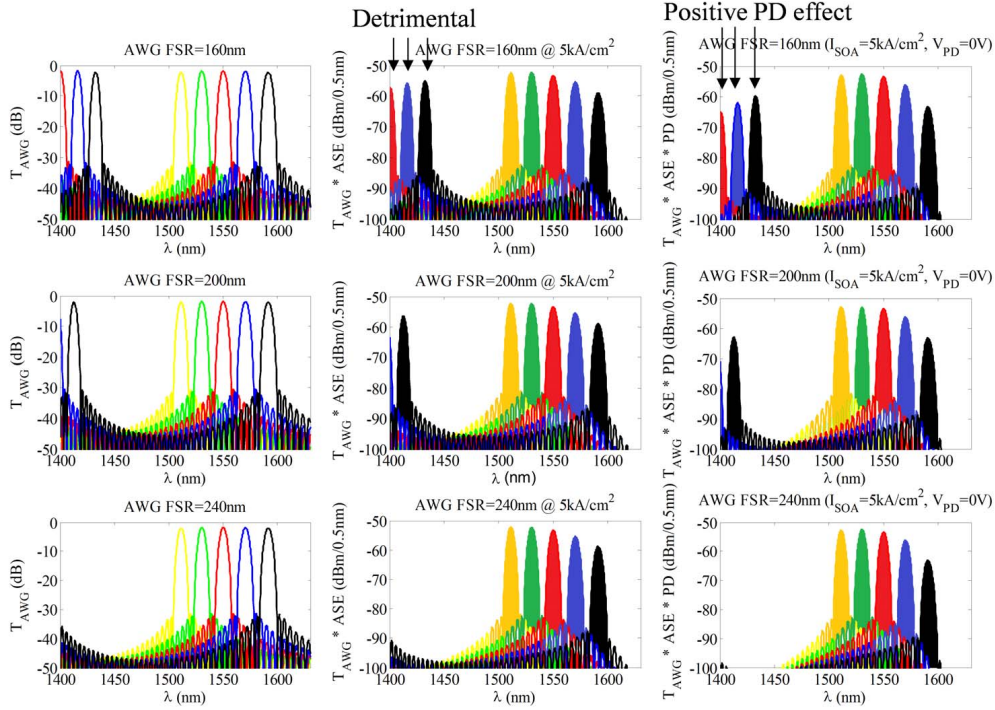
FIGURE 6.16: Simulated AWG transmission, *ASE* collected power from AWG transmission, and *ASE* collected power from AWG transmission and absorbed by PD for respectively 160 nm, 200 nm, and 240 nm FSR AWG.

by the AWG and absorbed by the PD is given by

$$I_{Di} = \int (ASE_{meas} \cdot T_i \cdot D) d\lambda \quad i = 1, ..., 5 \tag{6.9}$$

with D the typical PD transmission at 0 V, which is a function of wavelength. From the *ASE* intensity in (6.9) and (6.2) we calculate the modal gain, G_{D-FSR}. The *PD response and finite FSR induced gain error* ΔG_{D-FSR} is defined as the difference between the modal gain calculated with the ideal AWG transmission, obtained from eq. (6.3) and (6.2), and the one when the typical PD response is taken into account, calculated from (6.9) and (6.2)

$$\Delta G_{D-FSR} = G_{est} - G_{D-FSR} \tag{6.10}$$

In Figure 6.17 the finite FSR and PD response induced gain error is calculated for the AWGs with 160 nm and 200 nm FSR. We use these values to calibrate the final gain measurement curves. The gain error is calculated for the 200-400 μm long SOA pair with the current density 5 kA/cm^2. Similar values are found for the 400-800 μm long pair SOA and for other current values. A fourth order polynomial fit is used to estimate the gain error at intermediate wavelength points. The fourth order polynomial takes into account the quadratic behavior with wavelength of both, the PD [44], and the *ASE* [90] when they are considered together in equation 6.9.
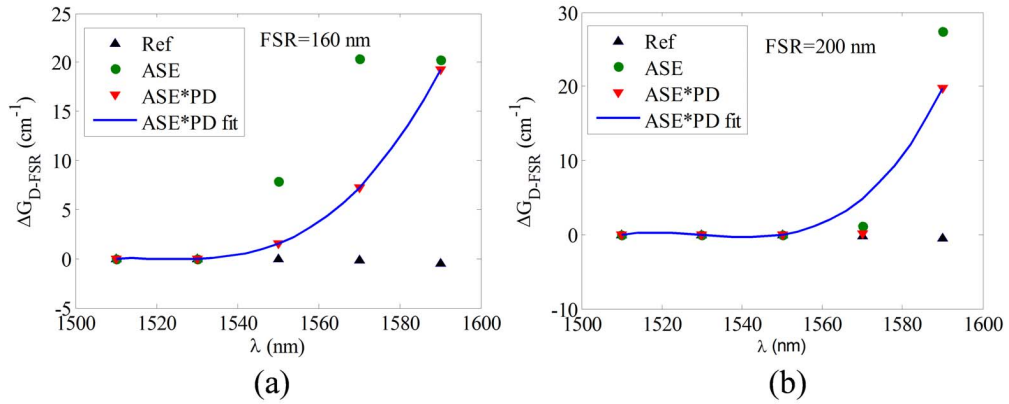
FIGURE 6.17: Gain error comparison between the Reference (infinite FSR), when only *ASE* is considered, and when both *ASE* and PD response is considered, (a) for a 160 nm FSR and in (b) for a 200 nm FSR.

For an AWG with an FSR of 160 nm the gain error at the edge of the C-band is 7 cm^{-1}, see Figure 6.17 (a). This gain error is systematic, therefore, we avoid it by calibrating the final gain measurement. The gain error fro which we have to calibrate reduces further if an AWG with a larger FSR is considered, see Figure 6.17 (b). An AWG with a larger FSR, however, has a larger footprint.

6.4.4 Final Measurement Accuracy

Crosstalk, roll-off, FSR, and photo detector response are well defined properties of the individual components, thus the gain error that they cause is a systematic one and can, therefore, be accounted for. After quantifying the individual systematic gain error sources, we add them up and compensate for them during electrical on-wafer characterization.

The other two error sources, namely the reproducibility limit of the ISDs and the AWG central wavelength shift cannot be predicted, and therefore, their effect on the overall measurement accuracy is calculated. The ISD related error is wavelength independent, whereas the AWG central wavelength shift error is wavelength dependent. Therefore, the overall gain measurement accuracy is wavelength dependent. Its dependence on wavelength is as follows:

- At the maximum gain region the gain measurement error is almost entirely due to the ISD related errors (the gain measurement error related to the central wavelength shift of the AWG is in the order of 0-1 cm^{-1}, therefore negligible in the calculation of the overall gain measurement error, see Figure 6.13). The measurement accuracy of the proposed test module is, therefore, in the order of 4 cm^{-1} (7.6 cm^{-1} for wafer W150-1).

- At the long wavelength edge of the C-band (1570 nm) the measurement accuracy is affected not only by the reproducibility limit of the ISDs but also by the central wavelength shift of the AWG. A 5 nm shift, the maximum

observed in our technology, corresponds to 5 cm^{-1} gain variation, see Figure 6.13. By considering the two uncertainties statistically independent on each other and applying equation (4.25) the measurement accuracy of the proposed test module at the edge of the C band is 6.4 cm^{-1}.

The AWG based test module is most suitable for characterizing gain at the maximum gain region (where the gain is flat). At this point only the gain error due to the limited ISD reproducibility is present, with as a consequence higher measurement accuracy.

6.5   Experiments

The on-wafer gain measurement test module, as well as the other on-wafer test modules, are designed with special attention for their testability. This means that extra effort was put to realize it in such a way that intermediate characterization of the individual BBs is also possible, in this case the AWG and the PDs. This was realized by adding an extra input waveguide to the AWG that could be accessed externally after dicing the wafer. Using this external input, shown in Figure 6.5, the integrated photo detectors and the AWG passband can be characterized using an external tunable laser. As can be seen from Figure 6.18 the measurement matches quite well with the simulation especially in terms of channel spacing (20 nm), and in terms of non adjacent crosstalk (-30 dB). Polarization conversion in the bends of the array is most probably the reason for the secondary peaks at the left side of the main peak at a power level of -20 dB [91]. The power level present in the secondary peaks is at a level of -20 dB, so their effect on the measurement error is expected to be low. The central wavelength is red shifted by 3 nm from the design value. The implemented FSR of 160 nm could not be measured accurately since the channel five peak at the short wavelength grating order is out of the measurement window of our laser. The 3 dB bandwidth of the AWG passband channels matches the simulation well. The power drop present at the last two channels is due to the reduced PD absorption at those wavelengths.

After characterizing the AWG, and confirming the assumptions made in the previous section, we measure the modal gain in the electrical domain by electrically contacting all the SOAs and the detectors. In Figure 6.19 the test module during on-wafer gain measurement is shown. During on-wafer measurement the temperature was stabilized at 18°C with a temperature controller.

The multisection SOA, shown in Figure 6.19, consists of four cascaded SOAs of lengths 200-200-400-800 μm, electrically isolated from each other. With this configuration the following SOA pairs can be obtained: 200-400 μm, 400-800 μm, and 800-1600 μm long.

Once the needles are contacted, the automated control software responsible for applying the required currents and voltages is started. Initially only the first 200 μm long SOA is pumped with current densities 1-10 kA/cm^2 in steps of 1 kA/cm^2, whereas at the other SOAs of the multisection SOA a 0 V bias is applied to prevent carrier injection into the unused SOAs. The generated photocurrent for each photo detector is recorded, with the PD reversely biased at 0 V as previously explained. Consequently the same current densities are applied to each of the first
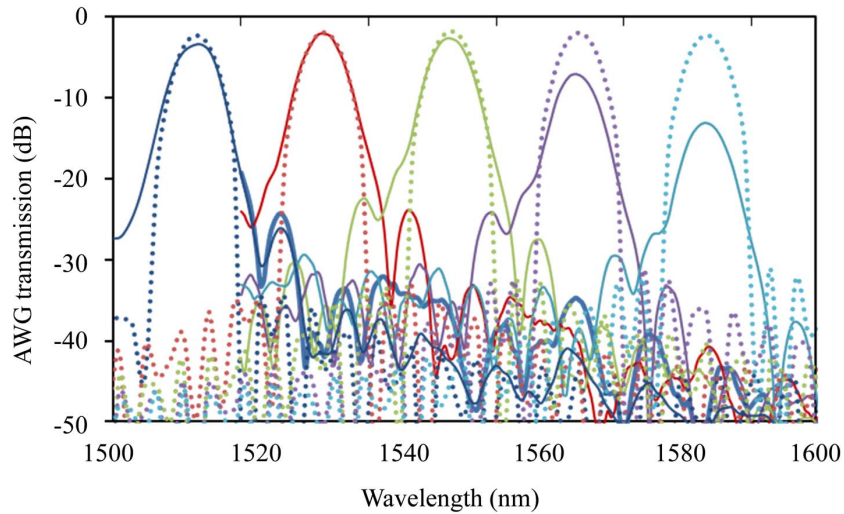
FIGURE 6.18: Measured (solid) vs. simulated (dashed) arrayed waveguide grating transmission measured by coupling at the external input a swept source and reading at the detector array the generated photocurrent. The characterized AWG is present on wafer W150-3

FIGURE 6.19: Microscope photograph of the on-wafer gain measurement test module while measuring. The measurement is realized through electrical signals only.

two 200 μm long SOAs simultaneously (obtaining a total SOA length of 400 μm) and recording the generated photocurrent at the photo detectors. Finally the gain for the 200-400 μm long pair is calculated through equation (6.2) for each of the AWG channels. The procedure is repeated for each different SOA combination, using always the same current densities (1-10 kA/cm^2). The modal gain, measured in this way for different current densities, is shown in Figure 6.20.

The first two pairs give very comparable results, as expected, whereas the last pair gives a significantly lower modal gain at all wavelengths. This might be due to the non optimal current distribution at the last SOA.

The electrical modal gain was measured in the test cell present in wafer W150-3. The optically measured modal gain, at the corresponding current densities, is also shown for comparison. A quadratic fit with respect to wavelength is used in the electrically measured modal gain to have an estimate of the gain peak. The gain peak is on average 4 nm red shifted if compared to the optically measured shift, due to the red shifted AWG response.
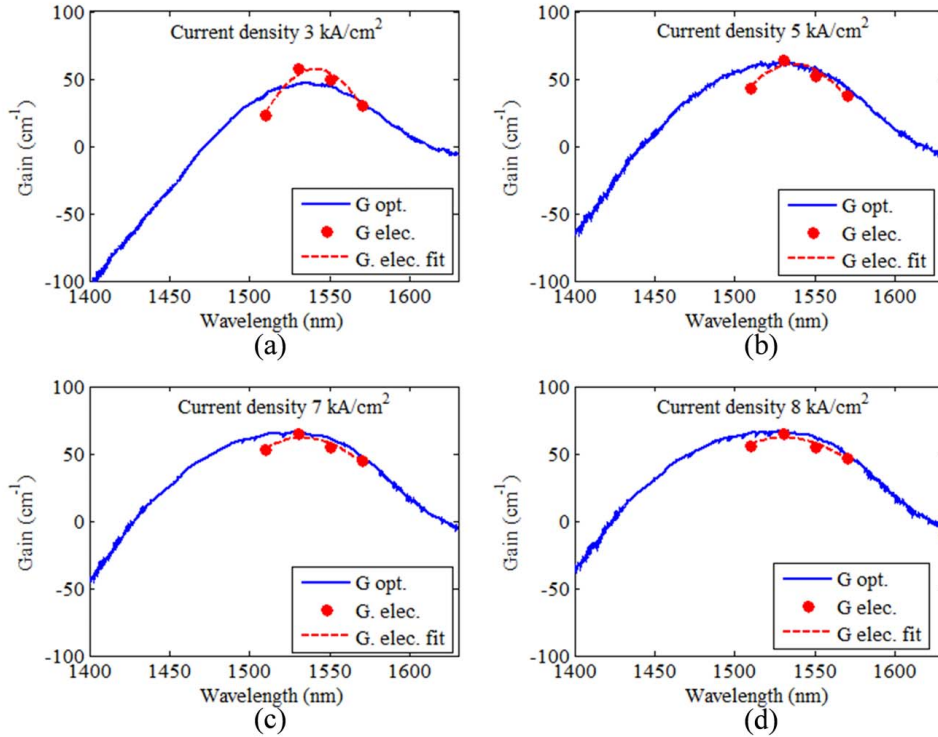
FIGURE 6.20: Optically (solid blue), and electrically (red) measured gain comparison for different current densities, in (a) for 3 kA/cm^2, in (b) for 5 kA/cm^2, in (c) for 7 kA/cm^2, and in (d) for 8 kA/cm^2. The dashed red curves are the quadratic gain fit to the measured electrical points. Characterization was performed in wafer W150-3

The fit in the C-band (1530-1565 nm) of the gain curves with respect to wavelength is quite good, with a max gain difference of, 6.4 cm^{-1} at 1570 nm and of only 1.5 cm^{-1} at max gain 1530 nm measured for a typical current density of 5 kA/cm^2. Both values fall within the uncertainty range of the test module determined in the previous section.

The electrical gain difference between the 200-400 μm and 400-800 μm long SOA pair differs by 6 cm^{-1}, which is within the uncertainty range of the test module determined previously. Very similar gain difference was observed when comparing gain measured from different test cells.

SOA saturation is observed at the current density of 7 kA/cm^2 which was confirmed by the optical measurement, see Figure 6.20 (c,d). Same current density was observed in the W150-1 wafer. Therefore, the electrical gain characterization is suitable to measure SOA saturation. The gain ripples conversely, are very difficult to observe in the electrical domain due to the very coarse sampling of the gain curves.

In channel one we observe an error larger than expected, that lowers the modal gain at the short wavelengths. An underestimation in the PD absorption at long wavelengths can be responsible for this error. We estimated an attenuation of 25 dB for channel 1 at the adjacent grating order (centered at 1700 nm). If this

assumption is not valid the PD of channel one absorbs non negligible *ASE* power from this grating order, which lowers the total gain estimated for 1510 nm.

To reduce the error, an AWG with an FSR of 240 nm (or larger) is the solution, with as drawback a 25% larger AWG footprint. Another solution is the use of an optical filter (such as an asymmetric MZI) before the AWG that reduces the transmission at the adjacent orders. Such a filter will also increase the footprint but may be fit in a smart way in the existing space.

The validity of the electrical characterization method is tested against the optical method. The methods used in both cases are very similar, the domain is different: electrical versus optical. Confirming the electrically measured gain with an independent method is however still missing.

6.6 Conclusions

In this chapter an on-wafer test module for measuring the spectral gain of semiconductor optical amplifiers is presented for the first time. By using electrical signals only it avoids the time consuming optical alignment and, therefore, speeds up the overall characterization process. The theoretical analysis of the individual components showed that the finite FSR of the AWG, as well as its central wavelength shift are the largest error sources for the modal gain measurement. The PD response and the SOA too introduce errors in gain measurement.

Comparing the electrical method to the optical equivalent one a difference ranging from 1.5 cm^{-1} at the maximum gain region up to 6.4 cm^{-1} at the outer channels was found, which is in very good agreement with the estimated accuracy limit of our test module. The overall footprint of the test module is 4 mm^2.

Chapter 7

Conclusions and Outlook

The goal of the PARADIGM project is to create a paradigm shift in the development and manufacturing of Indium Phosphide based photonic integrated components. This paradigm shift is performed by the introduction of the generic manufacturing concept. It leads to a more than tenfold reduction in prototyping cost for new photonic integrated chips.

Another potential advantage of the generic manufacturing concept is a strong reduction of the costs of testing. In this work we propose to achieve such a significant cost reduction by working in two aspects:

- Moving a large part of the testing from the circuit (chip) level to the BBB level (generic testing).

- Moving from die-level testing to wafer-level testing, which requires moving from the optical to the electrical testing domain.

Moving part of the characterization to a lower hierarchical level (from circuit level to BBB level testing) allows for generic characterization. Only a few BBBs have to be characterized. All the photonic integrated circuits composed of these BBBs, if designed according to the design rules, should have an overall performance that lies within specs.

We identified the passive waveguide, the phase modulator and the semiconductor optical amplifier as the most important basic building blocks. We investigated test modules to characterize the main properties of these building blocks.

Another aspect that allows a significant cost reduction and speeds-up the characterization process is moving from the optical to the electrical characterization domain. To achieve this sources and detectors are integrated together with optical filters or cavities in dedicated test modules suitable for characterization of optical properties in the electrical domain.

A major achievement reported in this thesis are the demonstration for the first time of a ring-resonator-based test module for measuring propagation loss and electro-optic phase modulation efficiency. It integrates a tunable source, a ring cavity and a detector. This test module has a small footprint and provides accurate characterization of propagation loss of passive waveguides, phase modulation efficiency of phase modulators, and excess loss of the MMI-coupler used in the test structure. By performing all the measurement in the electrical domain the

use of lensed fibers at the input is avoided. We demonstrated a significant increase in measurement accuracy since the excitation of higher order modes and/or transverse magnetic modes, which degrade the measurement accuracy, is avoided. Another important result is the integration of test structure for measuring the modal gain spectrum of an optical amplifier in the electrical domain, without optical probes. The structure consist of an arrayed waveguide grating with a large FSR integrated with a broad band source at the input and an array of detectors at the output.

These novel test modules, which are the main focus of this thesis, were proposed and demonstrated in different foundries. In particular, the ring based test module was realised on the Oclaro platform due to its capability to fabricate tunable DBR lasers, whereas the integrated spectrometer for on-wafer modal gain characterization was realized in the platforms of Oclaro and SMART Photonics. Novel test cells for investigating platform compatibility have been designed for all three JeP-PIX platforms, inluding Fraunhofer HHI, but the results of these runs will come after finishing this PhD thesis.

An important aim, which was identified later on in the project, was to investigate and demonstrate the compatibility of the different foundry platforms. We have, therefore, designed the test cells for all foundries using the same characterization concept and testing protocol. These test cells can track the platform performance in time (by comparing different MPW runs), and are a means to check the cross platform compatibility.

A future development is the development of automated on-wafer measurement of different test cells across the wafer, rather than characterizing singular test cells on-chip. The conceptual difference is small and poses no challenges from the research perspective but the impact it would have on the commercialization of generic manufactured PICs is very important.

On the singular test modules, two main improvements concern the integrated modal gain measurement test module.

- Improve the measurement accuracy at the outer wavelength regions of interest, that at present have the largest measurement error, by introducing an optical filter before the AWG to reduce the ASE outside the band of interest. Such a filter can be an asymmetric MZ interferometer.

- Another option to improve the accuracy at the outer wavelength regions is by increasing even further the FSR of the AWG. It has already been implemented in the test cell designs for the up-coming MPW runs. This improvement can be complementary to the previous solution or added to it.

Finally, the concepts developed in this thesis should be extended to characterisation of other BBBs on-wafer such as for example polarization converters, AWGs etc.

Bibliography

[1] R. N. Hall, G. E. Fenner, J. D. Kingsley, T. J. Soltys, R. O. Carlson, "Coherent Light Emission from GaAs Junctions," Physical Review Letters, **9**, 9, (1962).

[2] M. I. Nathan, W. P. Dumke, G. Burns, F. H. Dill, Jr., G. Lasher, "Stimulated Emission of Radiation from GaAs Junctions," Applied Physics Letters, **1**, 3, (1962).

[3] C. Cremer, "Grating Spectrograph in InGaAsP/lnP for Dense Wavelength Division Multiplexing," Applied Physics Letters, **59**, 9, (1991).

[4] M. Gustavsson, B. Lagerstrom, L. Thylen, M. Janson, L. Lundgren, A.-C. Morner, M. Rask, B. Stoltz, "Monolithically Integrated 4x4 InGaAsP/InP Laser Amplifier Gate Switch Arrays," Electronics Letters, **28**, 24, (1992).

[5] R. Nagarajan, et al., "Large-scale Photonic Integrated Circuits," IEEE Journal of Selected Topics in Quantum Electronics, **11**, 50–65, (2005).

[6] R. Nagarajan, et al., "Single-chip 40-channel InP Transmitter Photonic Integrated Circuit Capable of Aggregate Data rate of 1.6 Tbit/s," Electronics Letters, **42**, 13, (2006).

[7] S. W. Corzine, et. al., "Large-scale InP Transmitter PICs for PM-DQPSK Fiber Transmission Systems," IEEE Photonics Technology Letters, **22**, 7, (2010).

[8] R. Stabile, A. Albores-Mejia, K. A. Williams, "Monolithic Active-passive 16x16 Optoelectronic Switch," Optics Letters, **37**, 8, (2012).

[9] A. Rickman, G. T. Reed, B. L. Weiss, F. Namavar, "Low-Loss Planar Optical Waveguides Fabricated in SIMOX Material," IEEE Photonics Technology Letters, **4**, 6, (1992).

[10] D. F. Clark, M. S. Iqbal, "Simple extension to the Fabry-Perot technique for accurate measurement of losses in semiconductor waveguides" Optics Letters, **15**, 22, (1990).

[11] R. G. Walker, "Simple and Accurate Loss Measurement Technique for Semiconductor Optical Waveguides," Electronics Letters, **21**, 13, (1985).

[12] B. Hakki, T. Paoli, "CW degradation at 300°K of GaAs double-heterostructure junction lasers. II. Electronic gain," Journal of Applied Physics, **44**, 9, (1973).

[13] A. De Rossi, V. Ortiz, M. Calligaro, "Measuring Propagation Loss in a Multimode Semiconductor Waveguide," Journal of Applied Physics, **97**, 073105, (2005).

[14] Y. Sidorin, "On the Accuracy of the Measurement of Propagation loss in Channel Waveguides using the Fabry-Perot Resonance Method," Optics Communications, **194**, (2001).

[15] L. Finkelstein, M. S. Leaning, "A review of the fundamental concepts of measurement," : Measurement, **2** (1984).

[16] M. K. Smit, "A novel approach to the solution of indirect measurement problems with minimal error propagation," Measurement, **1**, (1983).

[17] J. R. Taylor, "An Introduction to Error Analysis: The Study of Uncertainties in Physical Measurements," Sausalito, CA, USA: University Science, (1982).

[18] L. Conway, "The M.I.T. 1978 VLSI System Design Course," (1978).

[19] MOSIS: Metal Oxide Silicon Implementation Service: Production solutions for IC innovation, http://www.mosis.com

[20] http://cmp.imag.fr

[21] http://www.europractice.com

[22] M. Smit, X. Leijtens, H. Ambrosius, E. Bente, J. van der Tol, B. Smalbrugge, T. de Vries, E. Geluk, J. Bolk, R. van Veldhoven, L. Augustin, P. Thijs, D. D'Agostino, H. Rabbani, K. Lawniczuk, S. Stopinski, S. Tahvili, A. Corradi, E. Kleijn, D. Dzibrou, M. Felicetti, E. Bitincka, V. Moskalenko, J. Zhao, R. Santos, G. Gilardi, W. Yao, K. Williams, P. Stabile, P. Kuindersma, J. Pello, S. Bhat, Y. Jiao, D. Heiss, G. Roelkens, M. Wale, P. Firth, F. Soares, N. Grote, M. Schell, H. Debregeas, M. Achouche, J. Gentner, A. Bakker, T. Korthorst, D. Gallagher, A. Dabbs, A. Melloni, F. Morichetti, D. Melati, A. Wonfor, R. Penty, R. Broeke, B. Musk, D. Robbins, "An introduction to InP-based generic integration technology", Journal of Semiconductor Science and Technology, **29**, 083001 (2014).

[23] M. Smit, X. Leijtens, E. Bente, J. Van der Tol, H. Ambrosius, D. Robbins, M. Wale, N. Grote, M. Schell, "Generic foundry model for InP-based photonics," IET Optoelectronics, **5**, 187-194 (2011).

[24] http://www.jeppix.eu

[25] http://www.epixfab.eu

[26] EU FP7 project EuroPIC: the European manufacturing platform for Photonic Integrated Circuits, http://europic.jeppix.eu

[27] EU FP7 project PARADIGM: Photonic Advanced Research And Development for Integrated Generic Manufacturing, http://paradigm.jeppix.eu

[28] Dutch Smartmix project MEMPHIS (Merging Electronics and MicroNano-Photonics in Integrated Systems) http://www.smartmix-memphis.nl

[29] P. Vettiger, M. K. Benedic, G. Bona, P. Buchmann, E. C. Cahoon, K. Datwyler, H. Dietrich, A. Moser, H. K. Seitz, O. Voegeli, D. J. Webb, P. Wolf, "Full-Wafer Technology-A New Approach to Large-scale Laser Fabrication and Integration," IEEE Journal of Quantum Electronics, **27**, 6 (1991).

[30] W. R. Heffner, A. Robertson, "Wafer Level Optoelectronic Testing for DFB Laser Diodes", in *Conference Proceedings - International Conference on Indium Phosphide and Related Materials*, (2000).

[31] H. D. Thacker, O. O. Ogunsola, A. V. Mule', J. D. Meindl, "Wafer-Testing of Optoelectonic–Gigascale CMOS Integrated Circuits," IEEE Journal of Selected Topics in Quantum Electronics, **17**, 3 (2011).

[32] M. Gould, J. Li, T. Baehr-Jones, M. Hochberg, "Full-Wafer Loss Measurements of Silicon Ridge Waveguides," in *Proceedings of 8th IEEE International Conference on Group IV Photonics (GFP)*, P2.3 (2011).

[33] A. Novack, Y. Liu, R. Ding, M. Gould, T. Baehr-Jones, Q. Li, Y. Yang, Y. Ma, Y. Zhang, K. Padmaraju, K. Bergmen, A.E.-J. Lim, G.-Q. Lo, M. Hochberg, "A 30 GHz silicon photonic platform," in *Proceedings of 10th IEEE International Conference on Group IV Photonics* (GFP), WA4 (2013).

[34] http://www.oclaro.uk

[35] Fraunhofer Heinrich Hertz Insitute, http://www.hhi.fraunhofer.de

[36] http://www.smartphotonics.nl

[37] D. Melati, F. Morichetti, G. G. Gentili, A. Melloni, "Optical radiative crosstalk in integrated photonic waveguides," Optics Letters, **39**, 13 (2014).

[38] http://www.thorlabs.de

[39] J. H. den Besten, R. G. Broeke, M. van Geemert, J. J. M. Binsma, F. Heinrichsdorff, T. van Dongen, T. de Vries, E. A. J. M. Bente, X. J. M. Leijtens, M. K. Smit, "A Compact Digitally Tunable Seven-Channel Ring Laser," IEEE Photonics Technology Letters, **14**, 6, (2002).

[40] L. A. Coldren, S. W. Corzine, M. L. Mashanovitch, "Diode Lasers and Photonic Integrated Circuits, 2nd Edition" John Wiley and Sons, (2012).

[41] L. A. Coldren, G. A. Fish, Y. Akulova, J. S. Barton, L. Johansson, C.W. Coldren, "Tunable Semiconductor Lasers: A Tutorial," Journal of Lightwave Technology, **22**, 1, (2004).

[42] A. J. Ward, D. J. Robbins, G. Busico, E. Barton, L. Ponnampalam, J. P. Duck, N. D. Whitbread, P. J. Williams, D. C. J. Reid, A. C. Carter, M. J. Wale, "Widely tunable DS-DBR laser with monolithically integrated SOA: Design and performance," IEEE Journal of Selected Topics in Quantum Electronics, **11**, 149–156 (2005).

[43] D. D'Agostino, D. Lenstra, H. Ambrosius, M. Smit, "Tunable Coupled Cavity Laser based on a 3x3 Multimode Interference Reflector," in *Advanced Photonics for Communications*, OSA Technical Digest (online) (Optical Society of America, 2014), paper IW1A.1

[44] B. E. A. Saleh, M. C. Teich, "Fundamentals of Photonics Second edition," Wiley Series in Pure and Applied Optics, Book, (2007).

[45] E. Kleijn, M. K. Smit, X. J. M. Leijtens, "Multimode Interference Reflectors: A New Class of Components for Photonic Integrated Circuits," Journal of Lightwave Technology **31**, 18, (2013).

[46] Y. Okamura, S. Yoshinaka, S. Yamamoto, "Measuring mode propagation losses of integrated optical waveguides: a simple method," Applied Optics, **22**, 23, (1983).

[47] P. Brannon, "Improved method of measuring optical waveguide propagation losses," Applied Optics, **25**, 20, (1986).

[48] W. McKinnon, D. Xu, C. Storey, E. Post, A. Densmore, A. Delâge, P. Waldron, J. Schmid, S. Janz, "Extracting coupling and loss coefficients from a ring resonator," **17**, 21, (2009).

[49] F. Xia, L. Sekaric, Y. Vlasov, "Mode conversion losses in silicon-on-insulator photonic wire based racetrack resonators," Optics Express, **14**, 9, (2006).

[50] F. M. Soares, "Photonic Integrated True-Time-Delay Beamformers in InP Technology," PhD Thesis, (2006).

[51] G. Tittelbach, B. Richter, W. Karthe, "Comparison of three transmission methods for integrated optical waveguide propagation loss measurement" Applied Optics, (1993).

[52] E. Kleijn, D. Melati, A. Melloni, T. de Vries, M. Smit, X. Leijtens, "Multimode interference couplers with reduced parasitic reflections," IEEE Photonics Technology Letters, **26**, 4, (2014).

[53] L. Soldano, "Optical Multi-Mode Interference Devices Based on Self-Imaging: Principles and Applications," Journal of Lightwave Technology, **13**, 4, (1995).

[54] P. A. Besse, M. Bachmann, H. Melchior, L. B. Soldano, M. K. Smit, "Optical Bandwidth and Fabrication Tolerances of Multimode Interference Couplers," Journal of Lightwave Technology, **12**, 1004-1009 (1994).

[55] A. Yariv, "Universal relations for coupling of optical power between microresonators and dielectric waveguides," Electronics Letters, **36**, 4, (2000).

[56] A. Vörckel, M. Mönster, W. Henschel, P. Bolivar, H. Kurz, "Asymmetrically Coupled Silicon-On-Insulator Microring Resonators for Compact Add-Drop Multiplexers," IEEE Photonics Technology Letters, **15**, 7, (2003).

[57] M. Felicetti, "Polarization Converter post-processing and Brillouin Sensing Optical Functionality in Generically Integrated Photonic Circuits," PhD thesis, (2014).

[58] F. Koyama, K. Iga, "Frequency Chirping in External Modulators," Journal of Lightwave Technology, **6**, 87-93 (1988).

[59] I. Kaminow, T. Li, A. E. Willner, "Semiconductor Photonic Integrated Circuit Transmitters and Receivers," in *Optical Fiber Telecommunications Volume VIA*, R. Nagarajan, C. Doerr, F. Kisha, (Elsevier 2013), pp. 25-98.

[60] J. Summers, T. Vallaitis, P. Evans, M. Ziari, P. Studenkov, M. Fisher, J. Sena, A. James, S. Corzine, D. Pavinski, J. Ou Yang, M. Missey, D. Gold, D. Lambert, W. Williams, M. Lai, F. Kish, D. Welch, "40 Channels x 57 Gb/s Monolithically Integrated InP-Based Coherent Photonic Transmitter," in *Proceedings of European Conference on Optical Communications*, (2014), P.2.5.

[61] S. C. Heck, S. K. Jones, R. A. Griffin, N. Whitbread, P. A. Bromley, G. Harris, D. Smith, L. N. Langley, T. Goodall, "Miniaturized InP Dual I&Q Mach Zehnder Modulator with Full Monitoring Functionality for CFP2," in *Proceedings of European Conference on Optical Communications*, (2014), Tu.4.4.2.

[62] H. N. Klein, H. Chen, D. Hoffmann, S. Staroske, A. G. Steffan, K.-O. Velthaus, "1.55 μm Mach-Zehnder Modulators on InP for Optical 40/80 Gbit/s Transmission Networks," in *Proceedings of International Conference on Indium Phosphide and Related Materials*, (2006), pp. 171–173.

[63] Chen Ji, R. G. Broeke, Y. Du, Jing Cao, N. Chubun, P. Bjeletich, F. Olsson, S. Lourdudoss, R. Welty, C. Reinhardt, P. L. Stephan, S. J. B. Yoo, "Monolithically Integrated InP-Based Photonic ChipDevelopment for O-CDMA Systems," IEEE Journal of Selected Topics in Quantum Electronics, **11**, 66-77 (2005).

[64] S. Adachi, K. Oe, "Linear electro-optic effects in zincblende-type semiconductors: Key properties of InGaAsP relevant to device design," Journal of Applied Physics, **56**, 74-80 (1984).

[65] S. Adachi, "Handbook on physical properties of semiconductor," (1992).

[66] H. Klein, "Integrated InP Mach-Zehnder Modulators for 100 Gbit / s Ethernet Applications using QPSK Modulation," in *PhD thesis*, (2010).

[67] S. Adachi, K. Oe, "Quadratic electro-optic (Kerr) effects in zincblende-type semiconductors: Key properties of InGaAsP relevant to device design," Journal of Applied Physics, **56**, 1499-1504 (1984).

[68] W. Franz, "Einfluss eines elektrischen Feldes auf eine Absorptionskante," 484-489, (1958)

[69] V. Keldysh, "The effect of a strong electric field on the optical properties of insulating crystals," 484-489, (1958).

[70] V. Lucarini, J. J. Saarinen, K. -E. Peiponen, E. M. Vartiainen, "Kramers–Kronig Relations in Optical Materials Research," in *Springer*, (2005).

[71] D. A. B. Miller, D. S. Chemla, T. C. Damen, A. C. Gossard, W. Wiegmann, T. H. Wood, C. A. Burrus, "Band-Edge Electroabsorption in Quantum Well Structures: The Quantum-Confined Stark Effect," Phys. Rev. Lett., **53**, 2173-2176 (1984).

[72] A. Chen, E. J. Murphy, "Broadband Optical Modulators," Chapter 7, pp. 173-196, (2012).

[73] N. Kikuchi, E. Yamada, Y. Shibata, H. Ishii, "High-speed InP-based Mach-Zehnder Modulator for Advanced Modulation Formats," in *Proceedings of Compound Semiconductor Integrated Circuit Symposium* (CSICS), (2012).

[74] C. H. Henry, R. A. Logan, K. A. Bertness, "Spectral dependence of the change in refractive index due to carrier injection in GaAs lasers," Journal of Applied Physics, **52**, 4457-4461 (1981).

[75] E. Burstein, "Anomalous optical absorption limit in InSb," Physical Review, 632-633 (1953).

[76] P. A. Wolff, "Theory of the band structure of very degenerate semiconductors," Physical Review, **126**, 405-412 (1962).

[77] E. Gini, H. Melchior, "The refractive index of InP and its temperature dependence in the wavelength range from 1.3 μm to 1.6 μm," in *Proceedings of the 8th International Conference on Indium Phosphide and Related Materials, IPRM'96*, (1996), WP-C 34.

[78] F. M. De Paola, V. d'Alessandro, A. Irace, J. H. den Besten, M. K. Smit, "Novel optoelectronic simulation strategy of an ultra-fast InP/InGaAsP modulator," in *Proceedings of the 7th International Conference on Optics*, pp. 762-766, (2004).

[79] G. Gilardi, W. Yao, H. Rabbani Haghighi, M. Smit, M. Wale, "Substrate thickness effects on thermal crosstalk in InP-based photonic integrated circuits," IEEE Journal of Lightwave Technology, **32**, 17, (2014).

[80] B. Hakki, T. Paoli, "CW degradation at 300°K of GaAs double-heterostructure junction lasers. II. Electronic gain," Journal of Applied Physics, **44**, 9, (1973).

[81] J. D. Thomson, H. D. Summers, P. J. Hulyer, P. M. Smowton, P. Blood, "Determination of single-pass optical gain and internal loss using a multisection device," Applied Physics Letters, **75**, 17, (1999).

[82] B. W. Tilma, M. S. Tahvili, J. Kotani, R. Nötzel, M. K. Smit, E. J. M. Bente, "Measurement and analysis of optical gain spectra in 1.6 to 1.8 μm InAs/InP (100) quantum-dot amplifiers," Optical and Quantum Electronics, **41**, 10, (2009).

[83] M. K. Smit, C. van Dam, "PHASAR-Based WDM-Devices: Principles, Design and Applications", IEEE Journal of Selected Topics in Quantum Electronics, **2**, 2, (1996).

[84] R. Mestric, M. Renaud, M. Bachmann, B. Martin, F. Gaborit, "Desgin and fabrication of 1.31-1.55-μm Phased-Array Duplexer on InP,"**2**, 2, (1996).

[85] Sh. Pathak, D. Van Thourhout, W. Bogaerts, "Design trade-offs for silicon-on-insulator-based AWGs for (de)multiplexer applications," Optics letters, **38**, 16, (2013).

[86] R. Adar, C. H. Henry, C. Dragone, R. C. Kistler, M. Milbrodt, "Broadband array multiplexers made with silica waveguides on silicon," Journal of Lightwave Technology, **11**, 2, (1993).

[87] K. Rausch, N. Yurt, D. F. Geraghty, N. Eradat, N. Peyghambarian, A. R. Kost, "Broadband arrayed waveguide gratings on InP," Optical and Quantum Electronics, **39**, 7, (2007).

[88] http://www.brightphotonics.eu

[89] N. Ismail, F. Sun, G. Sengo, K. Wörhoff, A. Driessen, R. M. de Ridder, M. Pollnau, "Improved arrayed-waveguide-grating layout avoiding systematic phase errors," Optics express, **19**, 9, (2011).

[90] R. G. Broeke, "A wavelength converter integrated with a discretely tunable laser for wavelength division multiplexing networks," PhD thesis, (2003).

[91] E. Kleijn, P. WIlliams, N. Whitbread, M. Wale, M. Smit, X. Leijtens, "Side-lobes in the response of arrawyed waveguide gratings caused by polarization rotation," Optics Express, **20**, 20, (2012).

Summary

Generic Testing in Photonic ICs

TU/e is leading a novel development in Photonic Integration that has enabled the introduction of a foundry model in photonics. This model is based on the concept of Basic Building Blocks (BBBs) as the simplest integrated photonic components whose basic functionalities can be used to synthesize a broad range of complex functionalities.

In such foundry processes validation of wafer quality has to be done at the level of the offered BBBs rather than at the level of the Photonic ICs, which is the responsibility of the designer, and it should be done at the wafer level in order to reduce the time required for testing and validation. But also for testing the fabricated Photonic ICs fast and accurate measurements are required. In this thesis we address both research challenges.

A systematic approach for wafer-scale validation is developed. It consists of including a dedicated generic test cell with which the performance of the most important BBBs, namely the passive interconnecting Waveguide (WG), the Phase Modulator (PM), and the Semiconductor Optical amplifier (SOA) is tested. To test each one of the above mentioned BBBs dedicated test modules are developed, demonstrated and presented throughout this thesis.

In order to be able to characterize these BBBs test lasers and detectors are integrated on the test chip. This approach offers the possibility for validation of optical properties in the electrical domain. By shifting the characterization from the optical to the electrical domain the critical and time consuming optical aligning is avoided.

To characterize propagation loss of passive waveguides a dedicated test module composed of an integrated tunable laser, an integrated detector and a ring resonator is used. The high ring sensitivity to propagation losses makes it the perfect choice for accurate measurement allowing an improvement from typical accuracy values of 1 dB/cm to 0.2 dB/cm. The use of electrical signals to drive the tunable laser and detector avoids the time-consuming and demanding optical alignment. For the on-wafer phase modulator characterization an integrated coupled cavity laser, a Mach-Zehnder interferometer and two detectors were used in the design of the dedicated test module. The performance of the Mach-Zehnder interferometer with the integrated laser is very similar to the case when using an external cavity laser. Another test module, similar to the one used for on-wafer characterization

of propagation loss of waveguide is proposed to characterize phase modulation. This test module includes a phase modulator inside the ring cavity. It is more compact than the MZI, therefore, very promising in integrated testing.

To characterize the modal gain of semiconductor optical amplifiers a compact integrated spectrometer with electrical control signals only was used. The spectrometer was realized by a specific design of an optical filter integrated with a multisection SOA in input and detectors in output. The opportunity of characterizing all the BBBs in the electrical domain through electrical signals opens the way to a much simpler automated measurement procedure, vital to quick and accurate cross-wafer characterization.

Further an accurate and fast measurement setup for characterizing Photonic ICs that are designed using a standard configuration for the electrical and optical IO-ports is developed. For both the wafer-scale measurements and the measurements of photonic ICs we have studied in depth the effects of a number of error mechanisms on the achievable measurement accuracy and using that analysis we have succeeded in increasing the accuracy of photonic measurements significantly.

Acknowledgments

It seems like yesterday when I had my Skype interview with Meint, Jos and Huub. And now after a bit more than 4 years I have to write the acknowledgments. It is really true: time flies when you have good time.

First of all I would like to start the acknowledgment section by thanking Meint for selecting me during the interview process, then for directly supervising me, and last but not least, leading me toward the highest achievement in my brief but very enjoyable scientific career, the Dr. title. From you Meint I learned to always push if I want to have things done. I learned to always ask questions, starting from myself, and be critic about everything. You introduced me to the very friendly PhI group and to the fantastic PARADIGM consortium. A special thank you goes to Kevin for co-supervising me. At first I admit I had some doubts whether Meint's decision on adding another supervisor during the last months of my PhD was a good idea. But soon I realized that your hard work and criticism helped in improving and speeding up my thesis. I wish you good luck with the very demanding but at the same time very rewarding task of leading the PhI.

Thank you Xaveer for letting me be part of the Wednesday's meetings, which most of the time were quite fun, and for solving my issues with C++ (before the MaskEngineering era). Thank you Jos for our discussions on sports and physics. You had always an answer to my physics puzzles, and always up for a good joke. Still remember your words: "... you have to be a mafia member in Albania to earn the same as a PhD!". Erwin, the lab lord, you always had a solution to the lab equipment problems. Made my life easier more than once, much appreciated.

Thank you Huub, Barry, Eric-Jan, Jeroen and Robert. Even though I did not work in the cleanroom, every time I needed something, chips to be cleaved or trainings, you were willing to help. Tjibbe I did not forget you. Thanks for the cleanroom help of course, but mainly thank you for organizing the football matches (was nice till it lasted) and the Thursday borrel.

And now is time to thank my PhD and Postdoc colleagues. Giovanni I will start with you. The first time I met you it was at the market square in Eindhoven and I was surprised by your laugh (and your long hair). The second time I met you was even a bigger surprise, at the day of your interview you were dressing like a professional dancer, instead of like a scientist. Sharing the office with you was a big pleasure, never annoying, always up for a laugh. I will miss our little experiments on bio-fluido-optics. Dima thank you for your kindness and madness. It made my start at the TU/e quite pleasent, I wish you all the best in Minsk. Manuela thanks for our roman talks. Thanks to you I found a bit of Rome even in Eindhoven. Thank you PhI girls, Kashia, Vale, Jing, Marija, Daan and Jolanda. You made the 10th flour less nerdy and more enjoyable. Dima P. and Rui thank

you for helping out at the SOLAR lab. Domenico I will always appreciate your expertise in the Phoenix SW and your willingness to help. Good luck with your thesis.

Weiming, it was a pleasure being you and playing the RF expert in Nice. Next time you need a replacement just let me know. Good luck with the big efforts to you and Giovanni in the 100+GHz transceiver. Sylvester, thanks for the efforts in keeping OLA a nice and organized lab. I know it is not always easy. I would also like to thank Hadi, for being always so kind and friendly. I wish you a lot of success in Canada. Antonio, by the moment I am writing the acknowledgments I hope you have already found a job. If not "In bocca al lupo" with the job and with the end of the PhD.

IMOS guys, Srivathsa, Yuqing, Longfei, Victor, Aura, Alonso, Vadim and Dominik, I wish you all the best, and good luck with the membrane laser. You guys deserve it. And a big good luck to you Emil and Staszek with your future careers in integrated photonics. Deepak my friend, your visits at our office were always pleasant. Good like with being a great parent and with ending your PhD. Good luck to the new come: Valeria, Perry and Monica.

A special thanks goes to my former colleagues at the TU and actual colleagues at ASML Jing, Ray and Josselin.

A very special thanks goes to Fraunhofer Heinrich Hertz Institute. Norbert thank you very much for welcoming me in Berlin. Those four months were a significant step ahead in my scientific career. Thank you Francisco for being a good friend and a very pleasant supervisor to work with during my stay in Berlin. Thanks to Martin my knowledge on DBR and DFB lasers got a big boost. Holger and Moritz thank you and good luck. From Berlin's crew special thanks go to George with whom I shared the office and who taught me a lot about RF measurements, patiently. The others that I do not remember I hope will forgive my poor memory.

A very special good luck to Boudewijn, Tim, Saeed and the rest of Effect Photonics team. I learned the good news of the funding a few days ago. It is nice to see that the hard work and dedication finally are paying off. I am very happy for you guys. You really deserve it.

Thank you Luc and your team at Smart Photonics for realizing the impossible: an MPW run in 3-4 months. Keep up the good work.

A special thanks goes to the committee members of my thesis. I apologize for the short time I gave you in reading my thesis and thank you in helping improving it. I tried to make the most out of every comment.

And as last but not least I would like to thank the PARADIGM consortium in general, and in particular Dave, Mike, Ronald, Andrea, Dominic, Daniele, Mohand, Richard etc. May be the best part of my PhD were the review meetings and especially the very friendly and delicious dinners all across Europe. I appreciated a lot the common effort toward making history in generic manufacturing of PICs. I wish you all the best with PARADIGM 2 and on. Special thanks to the Phoenix. A very big thank you to the very dedicated and always willing to help team. You solved quite a few of my head aches. Thank you to Oclaro and all its employees for the very beautiful pink chips. A large part of my thesis relied on your chips. Good luck with the demanding SI run.

Curriculum Vitae

Elton Bitincka was born in Korce, Albania, on May 26 1985. After finishing high school in Tirana, Albania, he moved to Rome to study Engineering. There he received the Bachelor and Master degree in Electronic Engineering both cum laude. During the Master's thesis work, pursued as an exchange student at the Denmark University of Technology, he discovered the potential of photonics. To continue the research in photonics he started a PhD within the Photonic Integration Group in the COBRA Research Institute at the Technical University of Eindhoven. As part of his PhD research he joined for a period of 4 months the Fraunhofer Heinrich Hertz Institute in Berlin. During his PhD research he was active with the Student Chapter of the IEEE Photonics Benelux Society. He has been an active member for several years and chairman in 2013. Athletics is a very important chapter in his life. He joined the local team in athletics when he was twelve. He has been practicing regularly ever since. He is the actual national champion and record holder in the discipline of 110 mh.

List of Publications

Journal Publications

- E. Bitincka, G. Gilardi, M. K. Smit, "On-wafer Optical Loss Measurements Using Ring Resonators With Integrated Sources and Detectors," IEEE Photonics Journal, **6**, 5, (2014).

- M. Smit, X. Leijtens, H. Ambrosius, E. Bente, J. van der Tol, B. Smalbrugge, T. de Vries, E. Geluk, J. Bolk, R. van Veldhoven, L. Augustin, P. Thijs, D. D'Agostino, H. Rabbani, K. Lawniczuk, S. Stopinski, S. Tahvili, A. Corradi, E. Kleijn, D. Dzibrou, M. Felicetti, E. Bitincka, V. Moskalenko, J. Zhao, R. Santos, G. Gilardi, W. Yao, K. Williams, P. Stabile, P. Kuindersma, J. Pello, S. Bhat, Y. Jiao, D. Heiss, G. Roelkens, M. Wale, P. Firth, F. Soares, N. Grote, M. Schell, H. Debregeas, M. Achouche, J. Gentner, A. Bakker, T. Korthorst, D. Gallagher, A. Dabbs, A. Melloni, F. Morichetti, D. Melati, A. Wonfor, R. Penty, R. Broeke, B. Musk, D. Robbins, "An introduction to InP-based generic integration technology," Journal of Semiconductor Science and Technology, **29**, 083001, (2014) (41pp).

Conference Publications

- E. Bitincka, D. D'Agostino, D. Pustakhod, R. G. Broeke, K. A. Williams, M. K. Smit, "On-wafer electrical characterization of Photonic Integrated Circuits (PICs)," in *Proceedings of IEEE Photonics Benelux Symposium* (2014).

- E. Bitincka, M. K. Smit, "Novel On-wafer Technique for Loss Characterization," in *Proceedings of Integrated Photonics Research, Silicon and Nanophotonics* (2014).

- E. Bitincka, R. G. Broeke, M. K. Smit, Electrical Method for On-Wafer Modal Gain Characterization of Semiconductor Optical Amplifiers," in *Proceedings of European Confenrence of Integrated Optics* (2014).

- E. Bitincka, R. G. Broeke, M. K. Smit, "Progress report on on-wafer testing of Photonic Integrated Circuits (PICs)," in *Proceedings of IEEE Photonics Benelux Symposium* (2013).

- E. Bitincka, E. Kleijn, M. K. Smit, "Accuracy analysis of the Fabry-Perot measurement method," in *Proceedings of Integrated Photonics Research, Silicon and Nanophotonics* (2013).

- F.M. Soares, J. Kreissl, M. Theurer, E. Bitincka, T. Goebel, M. Moehrle, N. Grote, "Transmitter PIC for THz Applications Based on Generic Integration Technology," in *Proceedings of Indium Phosphide and Related Materials* (2013).

- E. Bitincka, M. K. Smit, "On-wafer testing of Basic Building Blocks in Photonic Integrated Circuits (PICs)," in *Proceeding of IEEE Photonics Benelux Symposium* (2012).

- E. Bitincka, X. Leijtens, J. J. G. M. van der Tol, E. Kleijn, M. K. Smit, "Electrical on-wafer testing of Photonic Integrated Circuits (PICs)," in *Proceedings of IEEE Photonics Benelux Symposium* (2011).